ESD-TR-75-335

Semiannual Technical Summary

Seismic Discrimination

31 December 1975

Lincoln Laboratory

MASSACHUSETTS INSTITUTE OF TECHNOLOGY

LEXINGTON, MASSACHUSETTS

ADA025777

This technical report has been reviewed and is approved for publication.

FOR THE COMMANDER

Eugene C. Raabe, Lt. Col., USAF
Chief, ESD Lincoln Laboratory Project Office

MASSACHUSETTS INSTITUTE OF TECHNOLOGY
LINCOLN LABORATORY

SEISMIC DISCRIMINATION

SEMIANNUAL TECHNICAL SUMMARY REPORT
TO THE
DEFENSE ADVANCED RESEARCH PROJECTS AGENCY

1 JULY – 31 DECEMBER 1975

ISSUED 24 MARCH 1976

LEXINGTON   MASSACHUSETTS
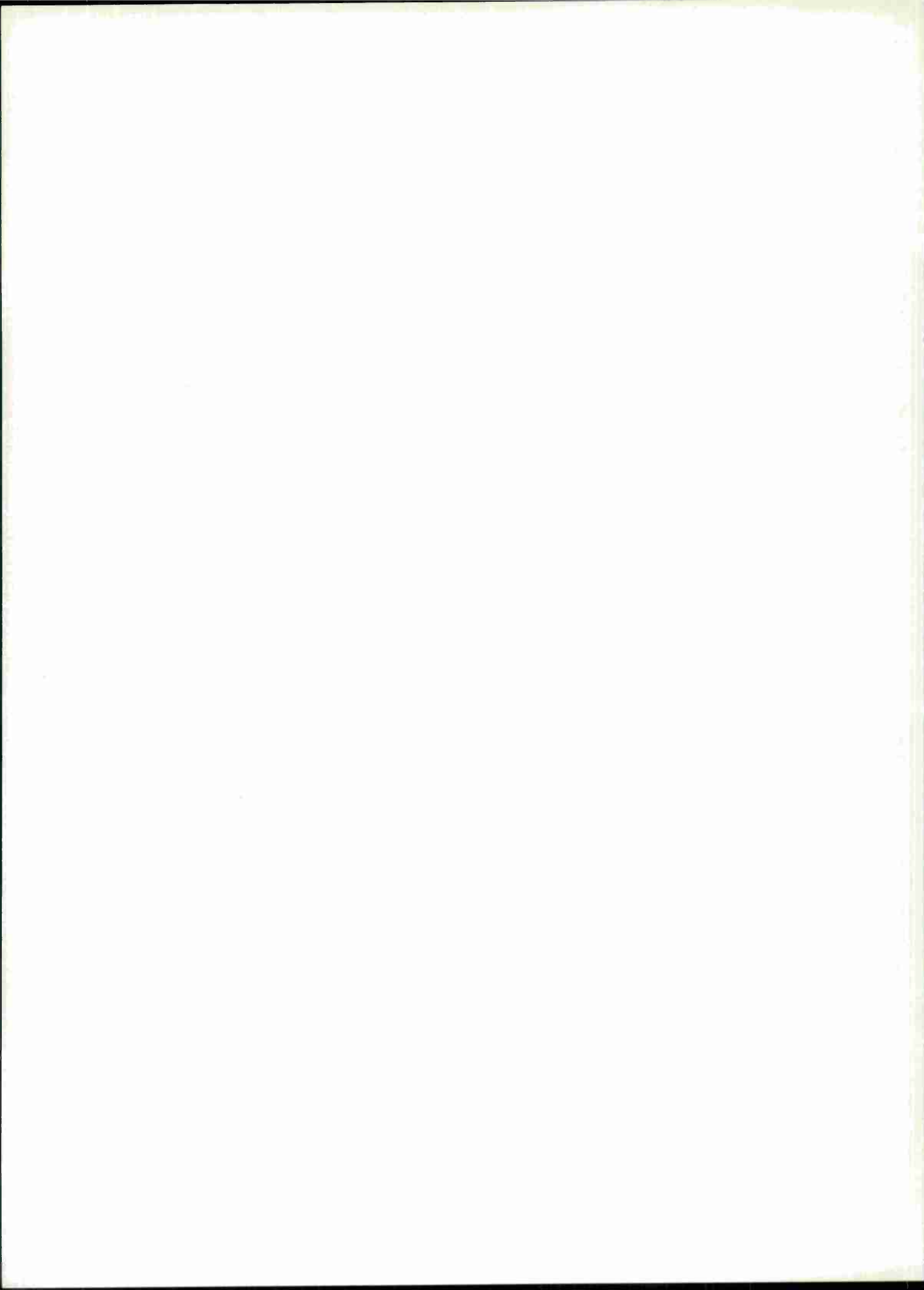
ABSTRACT

This report describes 23 investigations in the field of seismic discrimination. These are grouped as follows: estimation of magnitude by networks and single stations (6 contributions); studies relating to earth structure and scattering processes (7 contributions); studies in focal depth determination, source mechanism discrimination, and general seismology (6 contributions); and recent developments in computer systems and software for seismic data processing (4 contributions).

CONTENTS

SUMMARY

This is the twenty-fourth Semiannual Technical Summary report describing the activities of Lincoln Laboratory, M.I.T., in the field of seismic discrimination. These activities involve research into the fundamental seismological problems associated with the detection, location, and identification of earthquakes and nuclear explosions. We also are concerned with the development of methods for the handling and analysis of large quantities of global seismic data, and the application of these methods to data management system design and the optimum extraction of scientific information from high-quality digital data.

A detailed investigation into the problems associated with the estimation of magnitude by a network of seismic stations has been initiated. This was prompted by some earlier studies that suggested that the effects of station detection thresholds may be to insert a positive bias into network magnitudes for small events. The problem is primarily a statistical one, and a series of statistical models have been developed in order to facilitate the removal of these effects. The principal features of these models are described in this report. The next important problem is the optimum determination of the parameters describing the detection characteristics and bias of each station in a network. Some preliminary results along these lines are presented in this report. Other studies in magnitude estimation have concentrated on existing bulletin data, and several investigations show that current methods of determining magnitude, particularly body wave magnitude m_b, are open to some criticism.

We have continued to attack the general problem of earth structure and heterogeneity. An inversion of free oscillation data to obtain the attenuation parameter Q shows rather low values of Q in both upper and lower mantles, and no evidence for a frequency dependence of Q. Earlier work on tracing the paths of Rayleigh waves across the Eurasian continent has been extended by the inclusion of more information on crustal structure. Severe deviations from great-circle paths and large amplitude anomalies are predicted, and the agreement with observation is good. Studies of the P-wave codes from Novaya Zemlya explosions, using wave number analysis and adaptive deconvolution, show complex arrivals generated in the vicinity of the source. Other studies described include reflections from the 600-km discontinuity, and the applications of spatial correlation and transmission holography to seismic data.

Section III of this report describes a series of investigations related to seismic discrimination and general seismology. Further investigations of the Maximum Entropy method of spectral analysis have focused on the determination of the order of a time series, and the optimization of the length of the prediction error filter. Application of the method to the network determination of focal depth is included. Effects of source geometry on the discrimination between events with different source mechanisms are being studied. A series of travel-time tables based on a parametric representation are described. These have the advantages of high accuracy and low computer-storage requirements. An analysis is described which links the concept of the moment tensor of an earthquake with its radiated energy. An application of normal mode theory leads to a new method for the calculation of the permanent displacement fields of an earthquake.

·We have continued to develop the software and systems necessary for the analysis of digital seismic data from a global network. We have adapted previous software into a form suitable

for the display and processing of SRO data. An interactive system, utilizing the IBM 370/168 at Lincoln Laboratory, has been designed for the comparison of observed waveforms with those predicted by source mechanism theory. We are continuing to update the seismic documentation files that we constructed using the NLS system. Also, we are developing the additional software necessary for the full utilization of our connection to the ARPANET and the datacomputer at the Computer Corporation of America.

M. A. Chinnery

GLOSSARY

ARPANET	DARPA Computer Network
CCP	Control and Communication Processor
DARPA	Defense Advanced Research Projects Agency
EDR	Earthquake Data Reports
HGLP	High Gain Long Period (Network)
ISC	International Seismological Center
IWWSS	Integrated World-Wide Seismic System
LASA	Large Aperture Seismic Array
NEP	Network Event Processor
NIC	Network Information Center
NLS	On-Line System
NORSAR	Norwegian Seismic Array
NTS	Nevada Test Site
PDE	Preliminary Determination of Epicenters
PEM	Parametric Earth Model
SATS	Semiannual Technical Summary
SIP	Seismic Information Processor
S/N	Signal to Noise (Ratio)
SRO	Seismic Research Observatory
SUS	Seismic User Subsystem
USCGS	U.S. Coast and Geodetic Survey
USGS	U.S. Geological Survey
VESPA	Velocity Spectral Analysis
WWSSN	World-Wide Standard Seismograph Network
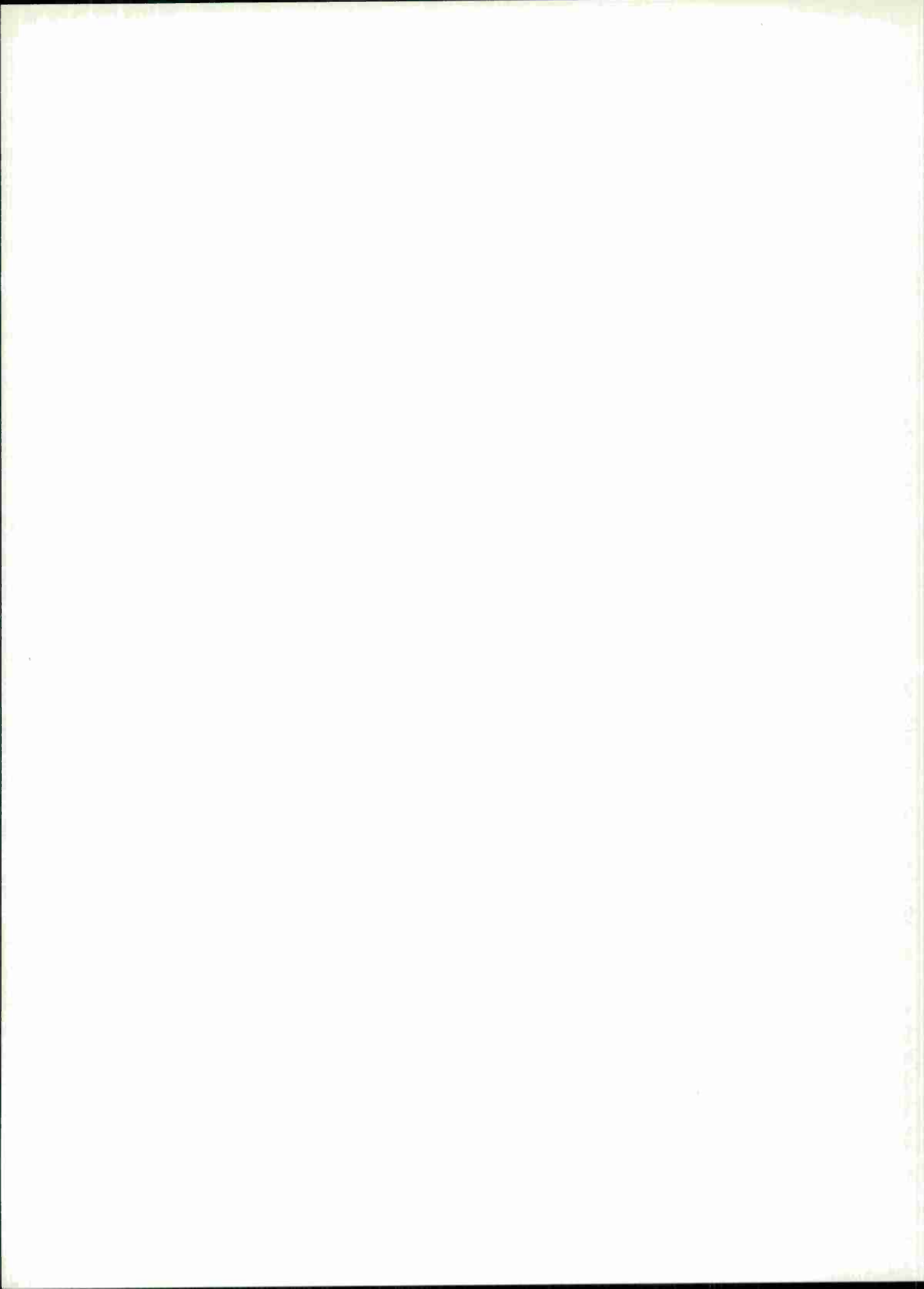
SEISMIC DISCRIMINATION

I. ESTIMATION OF MAGNITUDE

A. PROBLEMS IN MAGNITUDE ESTIMATION

Lincoln Laboratory has embarked on an in-depth investigation of the problems involved in the estimation of magnitude, using both single stations and networks. Previous Lincoln studies,[1] together with more recent work of Ringdal,[2] have demonstrated the importance of including station detection thresholds and biases when attempting to estimate the magnitude of small events using a network. We have extended these results, and have begun to apply them to network data.

The basic problems can be divided into two separate cases. The first problem concerns the development of methods for the estimation of magnitude by an idealized network. The crucial point here is that a report from each station in the network is received for each event. This report will consist of either "seen," when an amplitude and period will be recorded, or "not-seen," when the instrument noise level will be recorded. Such an idealized network is not presently available, but the new ARPA global network of arrays, SROs, and HGLP stations may be used in this way.

The second class of problem involves the data from imperfect networks, such as the group of stations currently used to produce the ISC and PDE Bulletins. In these cases, the "not seen" information is generally unreliable, due to inconsistencies in both instrumental status and operator characteristics.

In Secs. B through F that follow, we outline a series of statistical models that may be applicable to the above problems, and explore ways of estimating station detection threshold and bias. Some preliminary results from the application of these models are included.

Perhaps inevitably, detailed examination of these problems has raised a series of new questions that were not anticipated. Aspects of this work currently under investigation, and which will be reported in later publications, are as follows:

(1) Presumably clipping, and the difficulty in measuring very large swings on a photographic seismogram, leads to effects very similar to a detection threshold. Can they be described by similar statistical models? And how does this affect the magnitude estimation of large events in existing catalogues?

(2) To date, following Ringdal,[2] we have assumed the frequency-magnitude relation to be linear. In the case of m_b, this is a questionable assumption.[3] Newer models containing a quadratic relation are being developed and applied.

(3) One contribution to the variation in station amplitude A observed over a network for a given event is due to path differences, or Q. However, Q will also affect the observed dominant period T. Recording log A/T only partially corrects for this effect (see Sec. F). Also, this raises the complication that instrument response should be removed from station readings before the station magnitude is computed, and this is not a routine correction at all stations.

It appears likely that it will never be possible to completely remove these type of difficulties from existing earthquake catalogues. However, it may be possible to remove systematic biases from these data sources, and thereby reduce the observed scatter in m_b observations.

<div align="right">M. A. Chinnery</div>

B. STATISTICAL MODELS FOR MAGNITUDE ESTIMATION

We have extended the earlier work of Freedman,[4] Kelly and Lacoss,[1] and Ringdal,[2] in order to account for the detection characteristics of seismic stations and networks. We first list the assumptions and definitions used in the models, and then outline the models themselves for a number of useful cases.

Assumptions and Definitions

1. When the ith station in a network observes an event with true magnitude m, it will record a value of $[\log(A/T)]$, where A is the amplitude and T the period of the signal. For convenience, we set

$$y_i = [\log \frac{A}{T}]_i \quad . \tag{I-1}$$

We define the station magnitude m_i as

$$m_i = y_i + Q_i \tag{I-2}$$

where Q_i is the station distance-depth correction for the event, at the ith station. We then assume that m_i is related to m by an expression of the form

$$m_i = m + B_i + \epsilon_i \tag{I-3}$$

where B_i is the station bias, and ϵ_i is a Gaussian random variable with zero mean and variance σ_i^2.

2. We assume that the probability that an event will be detected at the ith station is given by

$$\Pr \{detection/y_i\} = \int_{-\infty}^{y_i} \frac{1}{\sqrt{2\pi} \, \gamma_i} \exp \{-1/2 \, [(z - G_i)/\gamma_i]^2\} \, dz$$

$$= \Phi\left(\frac{y_i - G_i}{\gamma_i}\right) \quad . \tag{I-4}$$

G_i is the detection threshold for observations of y_i, and corresponds to a 50-percent detection probability. γ_i determines the shape of the detection probability curve.

3. In certain cases, it will be more convenient to express the detection characteristics in terms of the station magnitude m_i. We may then attempt to represent the detection probability curve by an expression of the form

$$\Pr \{detection/m_i\} = \Phi\left(\frac{m_i - G_i^*}{\gamma_i^*}\right) \quad . \tag{I-5}$$

Equation (I-5) is formally equivalent to Eq. (I-4), with $\gamma_i^* = \gamma_i$ and $G_i^* = G_i + Q_i$, if all the events considered are located within a small region, so that paths and Q values to the network are the

same for all events. If the events lie within a distributed source area, Eq. (I-5) is an approximation, and G_i^* and γ_i^* will in general have no simple relation to G_i and γ_i.

4. We assume that the true magnitudes of earthquakes obey the Gutenberg-Richter relationship, in the form

$$\ln N = \alpha - \beta m \tag{I-6}$$

where N is the number of events in a small magnitude interval centered at m, and α and β are constants. It is necessary that β have the same value at all parts of the source region, for if this is not so, or if the magnitude-frequency relation is not linear, new complications arise. These will be the subject of future studies.

5. In the presence of a detection threshold, a station may report either a value of y_i (or m_i), or the report "not seen." In order to include a proper statistical treatment of the last possibility, it is necessary to introduce new variables a_i and μ_i defined as follows:

$$a_i = \begin{cases} y_i & \text{if event detected} \\ \text{"not seen"} & \text{if event undetected} \end{cases}$$

$$\mu_i = \begin{cases} m_i & \text{if event detected} \\ \text{"not seen"} & \text{if event undetected} \end{cases}.$$

Statistical Relationships

1. From assumption 1 above, the conditional distributions of y_i and m_i for events with true magnitude m are:

$$g^0\{y_i|m\}\,dy_i = \Theta\left\{\frac{y_i + Q_i - B_i - m}{\sigma_i}\right\}dy_i \tag{I-7}$$

$$h^0\{m_i|m\}\,dm_i = \Theta\left\{\frac{m_i - B_i - m}{\sigma_i}\right\}dm_i \tag{I-8}$$

where

$$\Theta\left(\frac{x}{\sigma_i}\right) = \frac{1}{\sqrt{2\pi}\,\sigma_i}\exp[-1/2\,(x/\sigma_i)^2] \quad . \tag{I-9}$$

2. In the presence of a detection threshold, these equations require modification. Now, the conditional distributions of a_i and μ_i (for both seen and unseen events) are

$$g\{a_i|m\}\,da_i = \begin{cases} \Phi\left(\dfrac{a_i - G_i}{\gamma_i}\right)\Theta\left\{\dfrac{a_i + Q_i - B_i - m}{\sigma_i}\right\}da_i & \text{(for "seen" events)} \\[4ex] \Phi\left\{\dfrac{-(B_i + m - Q_i - G_i)}{\sqrt{\sigma_i^2 + \gamma_i^2}}\right\} & \text{(for "unseen" events)} \end{cases} \tag{I-10}$$

3

and

$$
h\{\mu_i \mid m\}\, d\mu_i =
\begin{cases}
\Phi\left\{\dfrac{\mu_i - G_i^*}{\gamma_i^*}\right\} \; \Theta\left\{\dfrac{\mu_i - B_i - m}{\sigma_i}\right\}\, d\mu_i & \text{(for "seen" events)} \\[2em]
\Phi\left\{\dfrac{-(B_i + m - G_i^*)}{\sqrt{\sigma_i^2 + \gamma_i^{*2}}}\right\} & \text{(for "unseen" events)}
\end{cases}
\qquad (I\text{-}11)
$$

The parallelism of the formulations in terms of y_i and m_i is clear. In the expressions that follow, we quote only those for the station magnitudes m_i. Similar expressions in terms of y_i are easily derived.

3. If we consider only those events "seen" at the ith station, the conditional distribution for observed station magnitudes becomes

$$
H\{m_i \mid m\}\, dm_i = \frac{\Phi\left\{\dfrac{m_i - G_i^*}{\gamma_i^*}\right\} \; \Theta\left\{\dfrac{m_i - B_i - m}{\sigma_i}\right\}}{\Phi\left\{\dfrac{B_i + m - G_i^*}{\sqrt{\sigma_i^2 + \gamma_i^{*2}}}\right\}}\, dm_i \qquad (I\text{-}12)
$$

The shape of this distribution for the parameters $m = 3.8$, $B_i = 0$, $G_i^* = 4.0$, $\sigma_i = 0.3$, and $\gamma_i^* = 0.2$ is shown in Fig. I-1. For comparison, the Gaussian distribution with mean 3.8 and standard deviation 0.3 is also shown.

4. The expected value of observed station magnitudes m_i, given m, may be found from Eq. (I-12) to be

$$
E\{m_i \mid m\} = m + B_i + \frac{\sigma_i^2}{\sqrt{\sigma_i^2 + \gamma_i^{*2}}}\; z\left\{\frac{m + B_i - G_i^*}{\sqrt{\sigma_i^2 + \gamma_i^{*2}}}\right\} \qquad (I\text{-}13)
$$

where

$$
z(x) = \frac{\Theta(x)}{\Phi(x)} \quad .
$$

This equation is plotted in Fig. I-2, with the parameters $G_i^* = 4.0$, $B_i = 0$, $\sigma_i = 0.3$, and $\gamma_i^* = 0.2$.

5. In general, if an event of magnitude m is declared detected by a network of N stations when it is detected by at least one station in the network, the conditional distribution of the station observations $\mu_1, \ldots, \mu_N$ is

$$
H\{\mu_1, \ldots, \mu_N\}\, d\mu_1, \ldots, d\mu_N = \frac{\displaystyle\prod_{i=1}^{N} h\{\mu_i \mid m\}\, d\mu_i}{1 - \displaystyle\prod_{i=1}^{N} \Phi\left\{\dfrac{-(B_i + m - G_i^*)}{\sqrt{\sigma_i^2 + \gamma_i^{*2}}}\right\}} \quad . \qquad (I\text{-}14)
$$

In the case of a one-station "network," Eq. (I-14) reduces to Eq. (I-12). In the case of Eq. (I-12), m_i can be used rather than μ_i because the μ_i never takes on the "not seen" value.

6. Introducing the frequency-magnitude relationship, Eq. (I-6), we may derive the distribution of y_i and m_i for those events seen at the ith station without conditioning on m:

$$Q(y_i)\,dy_i = \beta\,e^{\beta(G_i - 1/2\beta\gamma_i^2 - y_i)}\;\Phi\left\{\frac{y_i - G_i}{\gamma_i}\right\}\,dy_i \tag{I-15}$$

$$R(m_i)\,dm_i = \beta\,e^{\beta(G_i^* - 1/2\beta\gamma_i^{*2} - m_i)}\;\Phi\left\{\frac{m_i - G_i^*}{\gamma_i^*}\right\}\,dm_i \quad . \tag{I-16}$$

Notice that these distributions are independent of B_i and σ_i.

7. Again using the linear seismicity assumption, the distribution of magnitudes recorded by a network of N stations, given that the event is seen by at least one station, becomes

$$R(\mu_1, \ldots, \mu_N)\,d\mu_1, \ldots, d\mu_N = \frac{\int_{-\infty}^{\infty} \left[\prod_{i=1}^{N} h\{\mu_i \mid m\}\,d\mu_i\right] e^{-\beta m}\,dm}{\int_{-\infty}^{\infty}\left[1 - \prod_{i=1}^{N}\left\{\frac{-(B_i + m - G_i^*)}{\sqrt{\sigma_i^2 + \gamma_i^{*2}}}\right\}\right] e^{-\beta m}\,dm} \quad . \tag{I-17}$$

8. The conditional distribution of the station magnitudes m_2 observed at station 2, given that a station magnitude m_1 has been observed at station 1, is

$$g\{m_2 \mid m_1\}\,dm_2 = \frac{\Theta\left\{\dfrac{m_2 - m_1 - B_2 + B_1 + \beta\sigma_1^2}{\sqrt{\sigma_1^2 + \sigma_2^2}}\right\}\Phi\left\{\dfrac{m_2 - G_2^*}{\gamma_2^*}\right\}}{\Phi\left\{\dfrac{m_1 + B_2 - B_1 - \beta\sigma_1^2 - G_2^*}{\sqrt{\sigma_1^2 + \sigma_2^2 + \gamma_2^{*2}}}\right\}}\,dm_2 \quad . \tag{I-18}$$

The expected value of m_2, given m_1, is then

$$E\{m_2 \mid m_1\} = m_1 + B_2 - B_1 - \beta\sigma_1^2 + \frac{\sigma_1^2 + \sigma_2^2}{\sqrt{\sigma_1^2 + \sigma_2^2 + \gamma_2^{*2}}}$$

$$\times z\left\{\frac{m_1 + B_2 - B_1 - \beta\sigma_1^2 - G_2^*}{\sqrt{\sigma_1^2 + \sigma_2^2 + \gamma_2^{*2}}}\right\} \quad . \tag{I-19}$$

Because of the similar forms of Eqs. (I-13) and (I-19), Fig. I-2 may be taken as a plot of Eq. (I-19) if the horizontal axis is labeled m_1 and the vertical axis m_2. The appropriate parameters are now $G_2^* = 4.0$, $B_2 - B_1 - \beta\sigma_1^2 = 0$, $\sigma_1 = \sigma_2 = 0.3/\sqrt{2}$, and $\gamma_2^* = 0.2$.

L.A. Christoffersson
R.T. Lacoss
M.A. Chinnery

C. ESTIMATION OF NETWORK MAGNITUDE AND STATION DETECTION PARAMETERS

Based on the relationships developed in the previous section, a series of computer programs have been written for the separate and joint estimation of network magnitude and the parameters describing the detection characteristics of the stations within the network. Four of these programs, together with some applications, are described below.

1. Network Magnitude Estimation

This program is designed to make a maximum-likelihood estimate of the magnitude of an event detected by a network, assuming that the detection probability curves and biases are known at each station in the network.

We assume that reports μ_i are received from each of the N stations in the network. As in the previous section, these reports may consist either of a station magnitude m_i, or the report "not seen." The appropriate distribution of the μ_i is given by Eq. (I-14), and the log-likelihood function L is obtained by simply taking the logarithm of this equation. We obtain

$$\log L = \sum_{i=1}^{N} \log h \{\mu_i | m\} - \log \left[1 - \prod_{i=1}^{N} \Phi \left\{ \frac{-(B_i + m - G_i^*)}{\sqrt{\sigma_i^2 + \gamma_i^{*2}}} \right\} \right] \quad . \tag{I-20}$$

The program maximizes this function with respect to m in order to obtain the maximum-likelihood estimate of m. B_i, G_i^*, and γ_i^* are assumed known. Notice that, in the case of a single event, we may write $G_i^* = G_i + Q_i$ and $\gamma_i^* = \gamma_i$ (see Sec. B above).

The likelihood function (I-20) differs slightly from that of Ringdal,[2] since he chose to include in his sample space the possibility that none of the stations saw the event. Also, the distribution $h \{\mu_i | m\}$ differs from his since we include the appropriate detection probability.

There remain some theoretical difficulties with the approach outlined above. It is known that maximum-likelihood estimates are asymptotically efficient for a broad class of distribution functions. However, we have not yet been able to demonstrate that the distribution (I-14) falls into this class. At present, this method is the only one that allows for the inclusion of "not seen" information, and we shall therefore pursue these problems. Certainly, initial results suggest that the method converges properly to reasonable values, both in this case and the one described below.

2. Joint Estimation of Network Magnitude, Station Biases, and Detection Thresholds

Suppose a set of K events occurs within a localized region, so that the path corrections Q_i are common to all events. We may then form a total log-likelihood function by summing the log likelihoods for the individual events, as given by Eq. (I-20). Noting, as before, that in this case $G_i^* = G_i + Q_i$ and $\gamma_i^* = \gamma_i$, we find

$$\log L = \sum_{j=1}^{K} \log L_j = \sum_{j=1}^{K} \left\{ \sum_{i=1}^{N} \log h \{\mu_i | m_j\} - \log \left[1 - \prod_{i=1}^{N} \Phi \left\{ \frac{-(B_i + m_j - G_i^*)}{\sqrt{\sigma_i^2 + \gamma_i^{*2}}} \right\} \right] \right\} \tag{I-21}$$

where m_j is the true magnitude of the jth event.

6

A program which maximizes this function with respect to the m_j, the B_i, and the G_i has been written. σ_i, γ_i, and Q_i must be assumed known. It has been tested on an aftershock sequence of 72 events located in a small region south of the island of Honshu, Japan. Station magnitudes were obtained from the data base of the International Seismic Month[5] for a set of 15 stations that were very carefully analyzed. We have assumed that the lack of a station magnitude corresponds to the verdict "not seen," and this is a very reasonable assumption for this data set. σ_i and γ_i were preset to the values 0.3 and 0.2, respectively, for all stations. The resulting estimates of station bias B_i, and station detection thresholds G_i and G_i^*, are listed in Table I-1. The extent to which these estimates are affected by incorrect values of σ_i and γ_i is not yet clear (the inclusion of σ_i and γ_i as free parameters in the problem results in severe computational difficulties).

Estimates of network magnitude may be plotted against the usual definition of magnitude (the average of the station magnitudes for those stations reporting the event). This is shown in Fig. I-3. Clearly, at low magnitudes, the conventional estimate is biased high.

TABLE I-1 ESTIMATES[†] OF STATION BIAS B_i, AND STATION DETECTION THRESHOLDS G_i AND G_i^*				
Station	B_i	G_i^*	Q_i	G_i
LAO	0.07	3.6	3.7	−0.1
MBC	0.29	4.1	3.9	+0.2
NAO	0.00	3.7	3.7	0.0
RES	0.38	4.2	3.7	+0.5
HFS	0.00	3.8	3.7	+0.1
UBO	−0.16	3.8	3.7	+0.1
KBL	0.09	4.1	3.9	+0.2
FFC	−0.03	4.3	3.7	+0.6
BLC	0.20	4.6	3.7	+0.9
ALE	0.05	4.5	3.7	+0.8
FBC	0.05	4.5	3.7	+0.8
CHG	−0.39	4.0	3.7	+0.3
COL	−0.21	4.2	3.8	+0.4
FCC	−0.15	4.4	3.7	+0.7
YKC	−0.21	4.4	3.7	+0.7

† Results of a preliminary experiment in the application of Eq. (I-21). Seventy-two events in an aftershock sequence south of Japan were used. σ_i and γ_i were assumed to be 0.3 and 0.2, respectively. Due to the small number of events used, the standard errors of the G_i are quite large, and values there should be considered presently unreliable.

3. Joint Estimation of Detection Parameters and Seismicity

Suppose a record is kept of all the $y = \log(A/T)$ values recorded at a station, and the results are plotted in histogram form. Assuming that the events seen are drawn from a population distributed in magnitude according to the Gutenberg-Richter relation (I-6), the observed distribution of y values will obey an equation of the form of (I-15). A log-likelihood function may be obtained from this equation:

$$\log L = \sum_{j=1}^{N} \left[\log \beta + \beta(G - \tfrac{1}{2} \beta \gamma^2 - y_j) + \log \Phi \left\{ \frac{y_j - G}{\gamma} \right\} \right] \qquad (I-22)$$

where the summation is over all the events recorded. A program has been written to maximize this likelihood function with respect to β, G, and γ. This is equivalent to the method of estimating β, G, and γ described by Kelly and Lacoss.[1] It differs from the approach of Aki,[6] who assumed $\gamma = 0$ (i.e., a step function detection probability curve).

This program has been applied to 228 observations of y at LASA from events in Japan. The cumulative distributions of observed and theoretical y are shown in Fig. I-4 which also gives 95-percent confidence bands, based on the Kolmogorov-Smirnov test. The theoretical curve lies well within these confidence bands. The corresponding parameter estimates are $\beta = 2.12$, $G = -0.08$, and $\gamma = 0.19$, with standard deviations of 0.03, 0.02, and 0.01, respectively ($\beta = 2.12$ corresponds to a "b-value" of 0.92). We would expect these values of G and γ to correspond to those given in Table I-1 for LAO, since both are derived from events in Japan. In fact, the agreement is better than was expected, considering the difference in methods and data.

4. Estimation of Detection Parameters Using a Pair of Stations

A particularly promising method for the estimation of detection parameters involves the conditional distribution of the station magnitudes m_2 at one station, given the station magnitude at a reference station, m_1. The appropriate distribution is given in Eq. (I-18), and is found to be independent of the detection characteristics of the reference station. A log-likelihood function can be constructed as above, and the resulting function maximized with respect to the free parameters, which in this case are G_2^*, γ_2^*, and $B = B_2 - B_1 - \beta \sigma_1^2$. A program has been written to estimate these parameters, and is in the final stages of testing.

Although a single station pair cannot permit the estimation of the separate biases B_1 and B_2, a method for determining these over a network is suggested. First a reference station is chosen, and then the relative bias of all the remaining stations can be found. If a new reference station is now chosen and the experiment repeated, the relative biases of all the stations in the network can be found. Adding the usual condition that $\sum_{i=1}^{N} B_i = 0$ is sufficient to determine the B_i uniquely.

L. A. Christoffersson
R. T. Lacoss
M. A. Chinnery

D. STATION MAGNITUDE BIAS AND ITS EFFECT ON NETWORK m_b ESTIMATION

An examination of individual station body wave magnitude (m_b) measurements has revealed that these may possess a sizable bias relative to the network m_b (generally computed as an

average of all determinations). The effect was first noticed in a comparison of Russian m_b determinations with those of the USCGS PDE list,[7] in which it was postulated that some stations which report very frequently have large negative biases. It is apparent that m_b values for smaller events, for which only a few stations report amplitude measurements, will be more greatly affected by such biases than larger earthquakes, for which many stations contribute to the network m_b and thus average out the effect of these biases. The effect of detection h-olds has not been considered in this study.

Data from the USCGS EDR lists for the first 6 months of 1971 have been used in a study of this effect. During this time period, 1840 events had associated network m_b determinations, provided by 12,049 m_b values from a total of 149 stations. Many of these stations reported so infrequently that they could be rejected, and, in fact, the 52 stations which reported more than 50 times during this time period contributed 91.2 percent of all m_b measurements.

Figure I-5 shows the distribution of USCGS m_b values compared with that for m_b values from the reduced network of only 52 stations, computed as the average of all magnitudes from these stations for each event. It can be seen that the neglect of the remaining 97 stations has had little effect upon either the shape of this curve or the total number of events (1825 vs 1840).

For each of these 52 stations, biases (station m_b − 52-station network m_b) have been computed, and are listed in Table I-2. Only events for which 12 or more stations reported m_b values have been used, and it is believed that this limitation ensures that the average m_b is not affected by a small number of stations with large biases. For each individual station the distribution of the biases is close to normal, with means ranging from −0.36 to +0.31 m_b units and standard deviations of 0.26 to 0.43. The stations reporting most frequently were found to have generally negative biases, which implies of course that the network m_b for the smaller events for which only these stations report will be artificially lowered. The mean biases obtained were (rounded to the nearest 0.1 magnitude unit) applied as corrections to the station m_b values, and the network m_b for all the stations used was recomputed.

Figure I-6 shows the distribution of m_b values obtained from this 52-station network with and without application of these bias corrections. It can be seen that the number of events at $m_b > 4.5$ has been reduced as expected, but, more surprisingly, that the events have become re-distributed such that there is a substantial increase in the number of events at higher magnitudes. This difference persists up to $m_b \sim 5.7$, and the application of bias corrections has increased the number of events at this magnitude from 25 to 38.

It is also of interest to consider the effect of removing certain stations which report frequently. Of the 52 stations used, three (BMO, UBO, EUR) in the western U.S. contributed 23 percent of all m_b observations. Network m_b values have been recomputed, without application of bias corrections, excluding these three stations only, and the magnitude-frequency curve for these is also shown in Fig. I-6. For many events, only these stations reported m_b values and, consequently, the total number of events has been reduced to 1587, this difference being mainly accounted for by a decrease in the number of events at lower magnitudes. It is, however, also evident that the biases at these stations are sufficient to reduce network m_b values up to quite high magnitudes. The opening or closing of such stations can clearly cause substantial temporal variations in the shape of the magnitude-frequency curve up to quite high magnitude levels. Furthermore, even if world network coverage were ideal, substantial differences in magnitude-frequency curves for various regions could be caused by bias effects.

	TABLE I-2				
	MEAN BIASES OF 52 STATIONS USED IN THIS STUDY, WITH RESPECT TO AVERAGE OF 52-STATION NETWORK				
Station	Mean Bias	Standard Deviation	Station	Mean Bias	Standard Deviation
ADE	0.138	0.311	KTG	0.055	0.247
ALE	0.044	0.239	LAO	0.006	0.369
ALQ	−0.011	0.301	LON	−0.291	0.361
ASP	−0.068	0.401	LOR	0.052	0.687
BMO	−0.252	0.322	LPB	−0.035	0.426
BNG	−0.297	0.352	LPS	−0.081	0.338
BNS	0.068	0.292	MOX	−0.085	0.293
BUL	−0.067	0.283	NEW	−0.114	0.305
CAR	0.045	0.356	NOR	−0.218	0.324
CLL	0.062	0.255	NUR	0.042	0.313
COL	−0.044	0.368	OIS	0.035	0.341
COP	0.218	0.280	PMG	0.195	0.430
CPO	−0.030	0.294	PMR	−0.055	0.352
DUG	−0.166	0.239	PNT	0.123	0.267
EDM	0.308	0.253	POO	0.124	0.383
EUR	−0.358	0.375	PRE	−0.106	0.336
FLO	0.288	0.265	QUE	0.119	0.405
FUR	−0.028	0.322	RAB	0.120	0.383
GOL	−0.101	0.361	RES	0.088	0.316
GRF	0.205	0.334	SJG	0.195	0.326
HYB	0.305	0.338	TOL	0.289	0.326
INK	0.139	0.259	TSK	−0.332	0.407
JCT	0.016	0.282	TUC	−0.129	0.259
KBL	0.067	0.324	TUL	0.207	0.334
KEV	−0.024	0.286	UBO	−0.150	0.335
KJN	0.009	0.293	WIN	−0.091	0.317

There are several possible causes for the large but consistent biases observed. It is dif-
ficult to separate actual station bias from the effects of station detection thresholds, but it is
considered that the values obtained represent mainly actual bias effects. The only parts of the
world where the coverage of the stations used is sufficiently dense for regional bias effects to
emerge are the continental U.S. and western Europe. Figure I-7 shows the variation of station
bias across the U.S., and it is clear that stations in the basin and range province have highly
negative biases compared with those further east. This is consistent with observations of the
variation of Q within the U.S.[8] All stations in western Europe had biases of 0.0 to 0.3 m_b units,
three stations in Finland (Baltic Shield) having zero bias. It is remarkable that such a poor
measure of amplitude as m_b can reveal such differences. Of course, it is possible that such
biases may be highly azimuth-dependent and, in particular, that certain source-receiver paths,
such as those traveling down lithospheric slabs, will be highly perturbed. We propose to exam-
ine this effect using a larger set of data so that more complete world coverage can be attained.

R. G. North

E. m_b ESTIMATION FOR LARGE EVENTS IN THE PDE CATALOGUE

The shape of the frequency-magnitude curve at its upper end is of importance for several
reasons,[3,9] including the fact that this places a constraint on certain theoretical models of the
seismic source. In the course of another study (see Sec. D above), it was noticed that events of
very large m_b (>6.5) were not calculated in a manner consistent with that used for smaller events.
In particular, the PDE magnitude of an event in the New Guinea region (7.3) was calculated as
the average of the three highest m_b observations, neglecting eleven which were less than m_b =
7.0. The m_b observations contributing to these large m_b values have been abstracted from the
earthquake data reports (EDR) of the PDE. The criteria upon which PDE m_b values are calcu-
lated are given in the introduction to each EDR as: rejection of any m_b observation for PkP
arrivals, P arrivals at distances of less than 5°, those associated with P travel-time readings
having residuals greater than 10 sec, and any differing significantly from the mean value. The
rejection of certain m_b observations is, at least for the larger events considered here, incon-
sistent with these restrictions.

We have recomputed the magnitudes of all events listed as having m_b > 6.5 during the period
1965-1970 (inclusive), using the EDR station magnitudes and our interpretation of the criteria
listed above. In every case, this resulted in a reduction in the calculated event magnitude. In
particular, all listed m_b values of 7.0 and greater have been reduced to below 7.0. Since explo-
sions contribute significantly to events at these high magnitudes, these too have been removed
from the data.

This revision of the largest m_b values has a significant effect on the shape of the frequency-
magnitude relationship. Figure I-8 shows the relationship for shallow events in the PDE listing
for the period 1965-1970 (inclusive). There is a suggestion that the curve becomes linear in the
m_b range greater than 6.5. The shape of the curve after revision of the large m_b values is shown
in Fig. I-9. For comparison, this figure also includes the same curve constructed from data in
the Bulletin of the International Seismological Center (ISC).

The two data sets have a remarkably similar shape, except for m_b < 5.0 since the ISC Cata-
logue has a somewhat lower detection threshold. In general, the ISC Catalogue contains fewer
events with a listed magnitude, since it requires a minimum of three station magnitudes before

an event magnitude is computed. At the upper end of the curves, the agreement is excellent. Presumably, the ISC criteria are very similar to those adopted here.

The data in this study were limited to the period 1965-1970 since the magnetic-tape version of the ISC Bulletin is only available to us through the end of 1970. PDE m_b values for large events after 1971 appear to be consistent with the stated criteria. The extent to which these discrepancies exist at $m_b \leqslant 6.5$ is not known, although the general similarity in shape of the ISC and PDE data (Fig. I-9) suggests that it is likely to be small.

We conclude that events with $m_b > 6.8$ or 6.9 occur very rarely, if at all. This is consistent with suggestions in earlier studies.[3]

<div align="right">

R. G. North
M. A. Chinnery

</div>

F. AMPLITUDES AND PERIODS OF THE 1965 RAT ISLAND SEQUENCE

Amplitudes and periods of P-wave first arrivals as reported in the Earthquake Data Reports (EDR) for over 300 events of the Rat Island sequences of February to April 1965 have been analyzed. Four Vela array stations — CPO (Tennessee), TFO (Arizona), WMO (Oklahoma), and UBO (Utah) — at which all these events were recorded and assigned P-wave arrival amplitudes and period have been used. These cover source azimuths of 55° to 75° and are at distances of 40° to 65°. The variation in both azimuth and take-off angles of the rays as they leave the source is thus fairly small, and it is hoped that source radiation pattern effects are negligible.

An immediately noticeable feature of the data was that the reported period T of the first arrivals differed appreciably both at each individual station and between stations. Figure I-10 shows the histograms of these periods at each station. The periods range from 0.3 to 2.2 sec, but their distribution shows large variations from station to station. The most frequently reported periods for each station are 0.6 sec (CPO), 0.8 sec (TFO, WMO), and 0.9 sec (UBO). There is remarkably little overlap between the distribution of periods at CPO and those at the other three stations.

Figure I-11 shows the variation of $\log(A/T)$, where A is the amplitude of the first arrival, as a function of reported period T for each station. Each point is the mean value of $\log(A/T)$, and the bar indicates its associated standard deviation. The parameter $\log(A/T)$, with an additional distance-depth correction, is simply the body wave magnitude m_b. This figure thus shows the variation of dominant period T with magnitude. In all cases, T increases quite sharply with $\log(A/T)$.

Least-squares fits have been made to these data, and the values of a and b where

$$\log(A/T) = a + bT \qquad\qquad\qquad (I-23)$$

and the correlation coefficient R are given in Table I-3. Although R varies from 0.41 to 0.56 reflecting the scatter in the data, it can be seen from Fig. I-11 that these lines fit the data quite well.

The intercept a = 0.179 for CPO is ~0.2 to 0.3 m_b units higher than the other station intercepts, and the slope b = 0.736 is slightly lower than the slopes of the other stations. In Fig. I-12, the mean values of $\log(A/T)$ are plotted vs T for all four arrays. Also shown is the attenuation effect of two average Q values over a distance of 50°. The attenuation is given by

$$A(f) = e^{-\pi f t*}$$

TABLE I-3
LEAST-SQUARES FIT OF DATA TO EQ. (I-23) AT EACH STATION. R IS THE CORRELATION COEFFICIENT.

Station	a	b	R
CPO	0.179	0.736	0.562
TFO	−0.192	0.857	0.408
UBO	−0.030	0.857	0.443
WMO	−0.003	0.816	0.517

where $t^* =$ travel time$/Q$. The curve for $Q = 1330$ was calculated using Archambeau's Q model,[10] based on short-period recordings of NTS explosions. The t^* for this model is ~0.40, which is comparable to other values measured teleseismically.[11]

The data show that Q values between ~1330 and 665 could explain the $\log(A/T)$ dependence on period, ignoring seismic scaling effects which must be present. Such scaling effects cannot be determined independently of Q from these data. We plan to use scaled source functions from presumed U.S. explosions on nearby Amchitka Island to determine Q more accurately for these particular paths. This information will enable us to estimate seismic scaling effects for this Rat Island sequence.

These data raise a certain dilemma in that apparent m_b at these stations is strongly frequency dependent. Thus, reliable m_b determinations require adequate knowledge of Q along the ray paths.

C.W. Frasier
R.G. North

REFERENCES

1. E. J. Kelly and R. T. Lacoss, "Estimation of Seismicity and Network Detection Capability," Technical Note 1969-41, Lincoln Laboratory, M.I.T. (16 September 1969), DDC AD-695044.

2. F. Ringdal, "Maximum Likelihood Estimation of Seismic Event Magnitude from Network Data," Technical Report No. 1, Vela Network Evaluation and Automatic Processing Research, Texas Instruments, Inc. (27 March 1975).

3. Seismic Discrimination SATS, Lincoln Laboratory, M.I.T. (30 June 1974), DDC AD-785377/3.

4. H. W. Freedman, "Estimating Earthquake Magnitude," Bull. Seismol. Soc. Am. $\underline{57}$, 747-760 (1967).

5. R. T. Lacoss, R. E. Needham, and B. R. Julian, "International Seismic Month Event List," Technical Note 1974-14, Lincoln Laboratory, M.I.T. (27 February 1974), DDC AD-776021/8.

6. K. Aki, "Maximum Likelihood Estimate of b in the Formula $\log N = a - bM$ and its Confidence Bands," Bull. Earth. Res. Inst. $\underline{43}$, 237-239 (1965).

7. V. I. Buen, N. A. Vvedenskaya, I. V. Gorbunova, N. V. Kondorskaya, N. S. Landyreva, and I. V. Fedorova, "Correlation of M_{LH} and m_{pv} by Data of the Network of Seismic Stations of the USSR, Geophys. J. R. Astr. Soc. $\underline{19}$, 533-542 (1970).

8. S. C. Solomon, "Seismic Wave Attenuation and Partial Melting in the Upper Mantle of North America," J. Geophys. Res. $\underline{77}$, 1483-1502 (1972).

9. M. A. Chinnery and R. G. North, "The Frequency of Very Large Earthquakes," Science $\underline{190}$, 1197-1198 (1975).

10. C. B. Archambeau, E. A. Flinn, and D. G. Lambert, "Fine Structure of Upper Mantle," J. Geophys. Res. $\underline{74}$, 5825-5865 (1969).

11. C. W. Frasier and J. Filson, "A Direct Measurement of the Earth's Short-Period Attenuation Along a Teleseismic Ray Path," J. Geophys. Res. $\underline{77}$, 3782-3787 (1972).
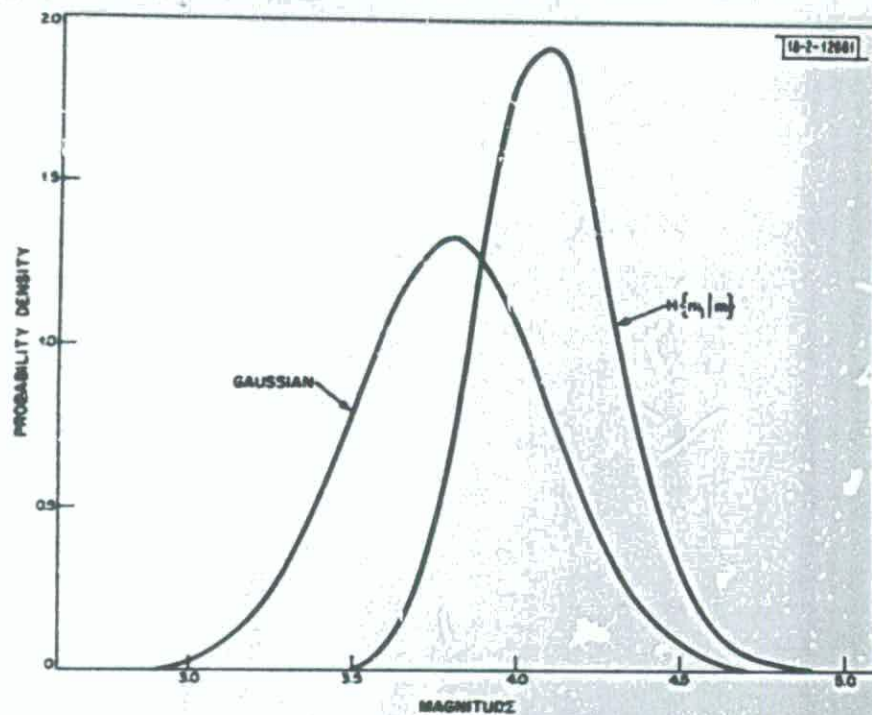
Fig. I-1. Frequency distribution H $\{m_i|m\}$ for m = 3.8, $G_i^* = 4.0$, $\sigma_i = 0.3$, $\gamma_i^* = 0.2$, and corresponding Gaussian distribution with expectation 3.8 and standard deviation 0.3.
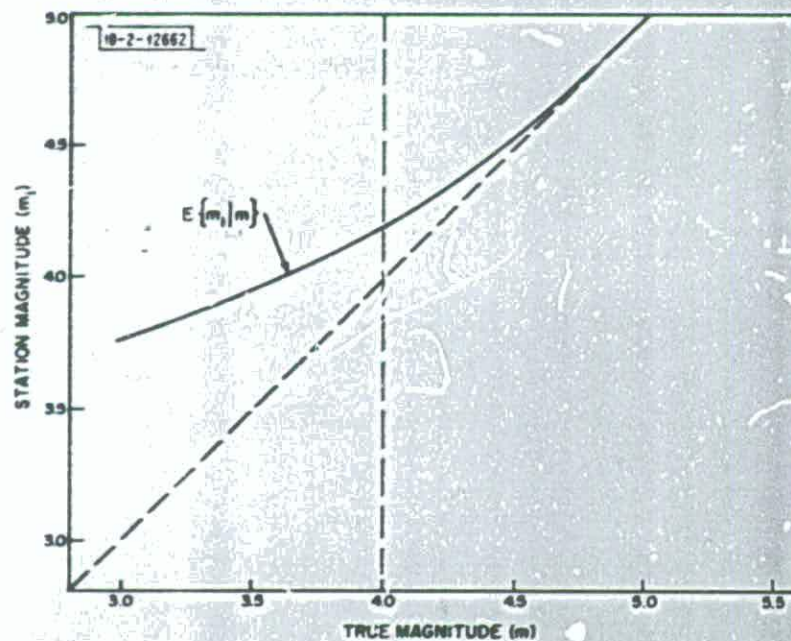
Fig. I-2. Expected magnitude at a station for a given true magnitude m, according to Eq. (I-13). Parameters used are $G_i^* = 4.0$, $B_i = 0$, $\sigma_i = 0.3$, and $\gamma_i^* = 0.2$.
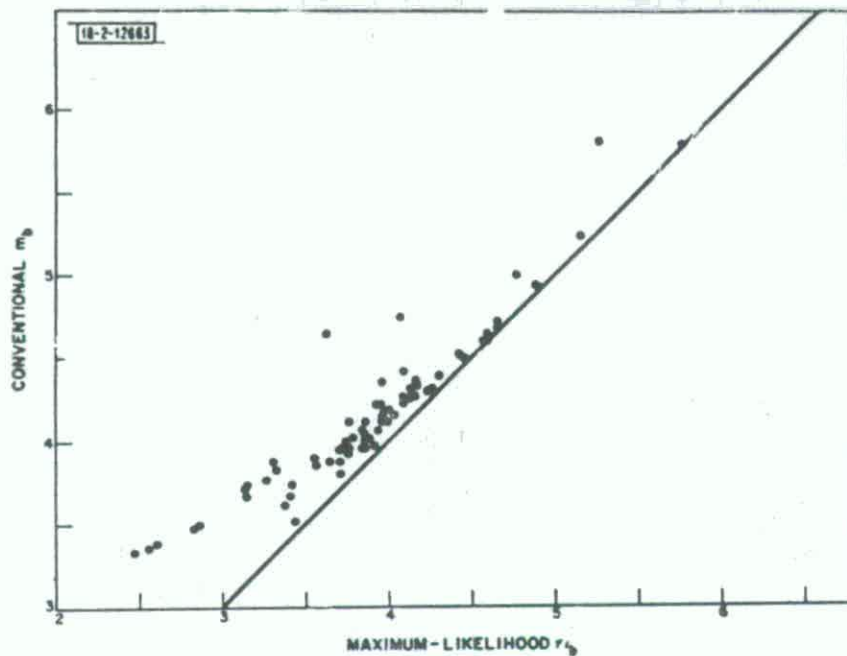
Fig. I-3. Plot of conventional m_b against maximum-likelihood m_b estimated using detection parameters listed in Table I-1, for a set of 72 events located south of Japan and observed at a network of 15 stations.
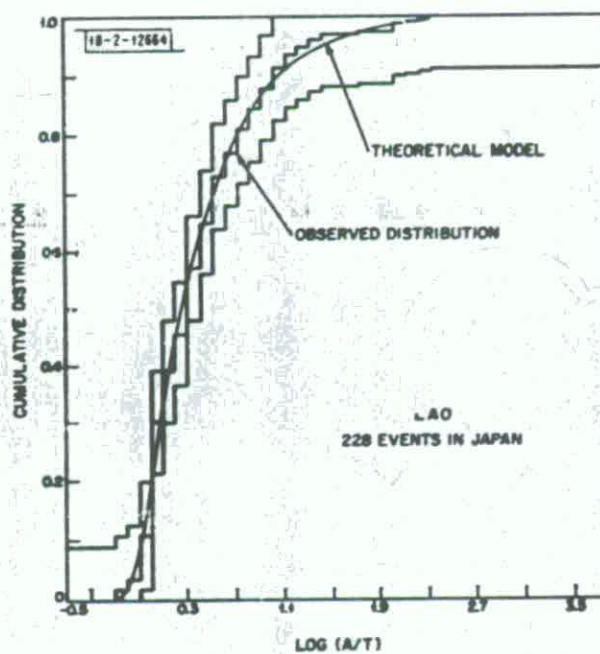
Fig. I-4. Distribution of log (A/T) for 228 events from Japan observed at LASA. Smooth curve is maximum-likelihood estimate, center step curve is observed distribution, and others are upper and lower 95-percent Kolmogorov-Smirnov confidence bands.
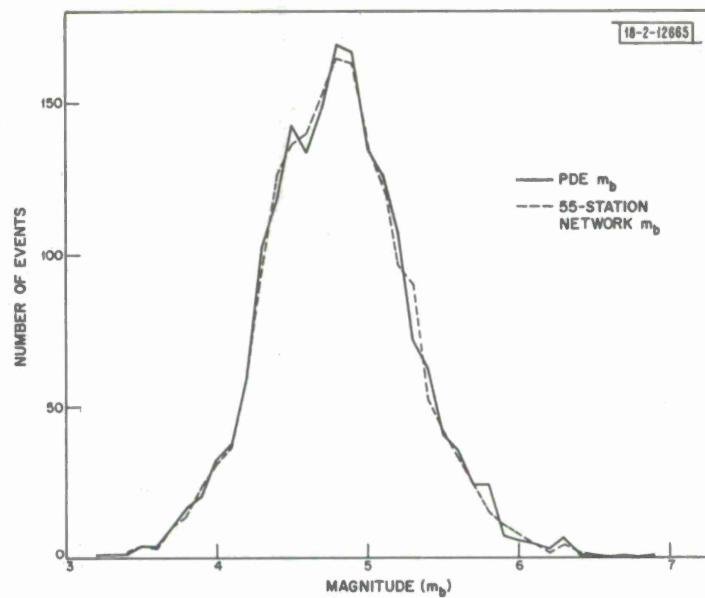
Fig. I-5. Magnitude-frequency curves for January through June 1971, for magnitudes from PDE Catalogue, and from network of 52 stations uncorrected for bias.
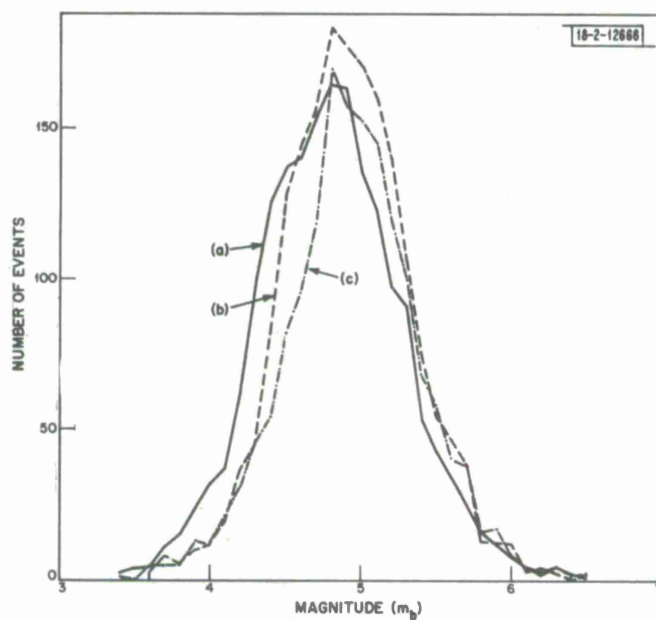
Fig. I-6. Magnitude-frequency curves for January through June 1971, magnitudes from 52-station network: (a) uncorrected; (b) corrected for bias; and (c) uncorrected, stations UBO, BMO, EUR removed.

17
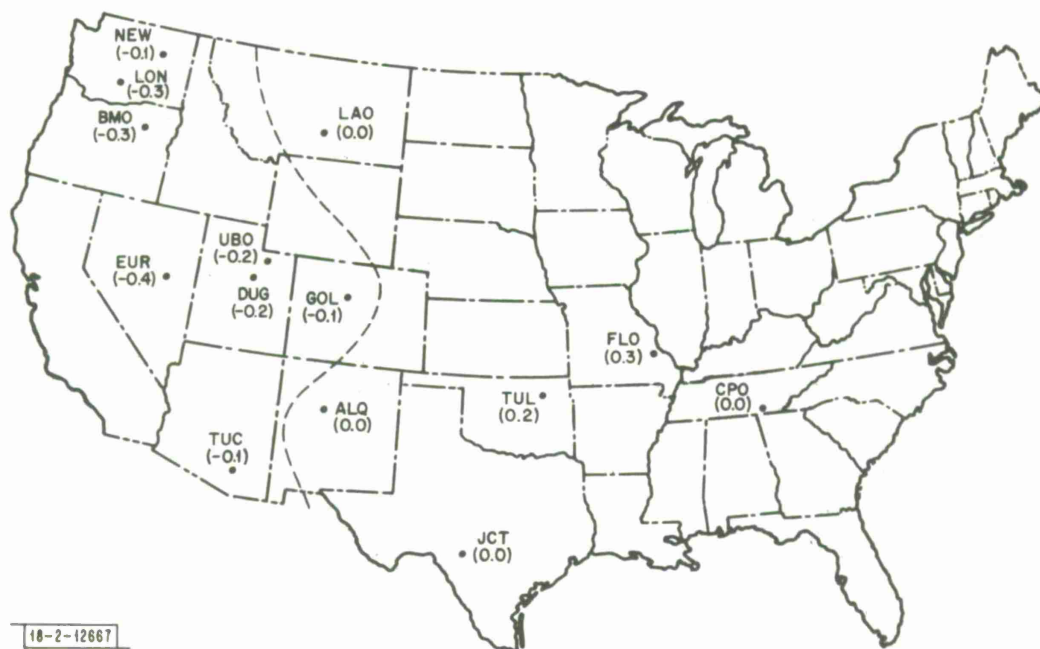
Fig. I-7.   Variation of mean station bias in m_b across U.S.   Dashed line separates negative from positive values.

Fig. I-8. Frequency-magnitude curve for 1965-1970 (inclusive) using values of m_b listed in PDE Catalogue.
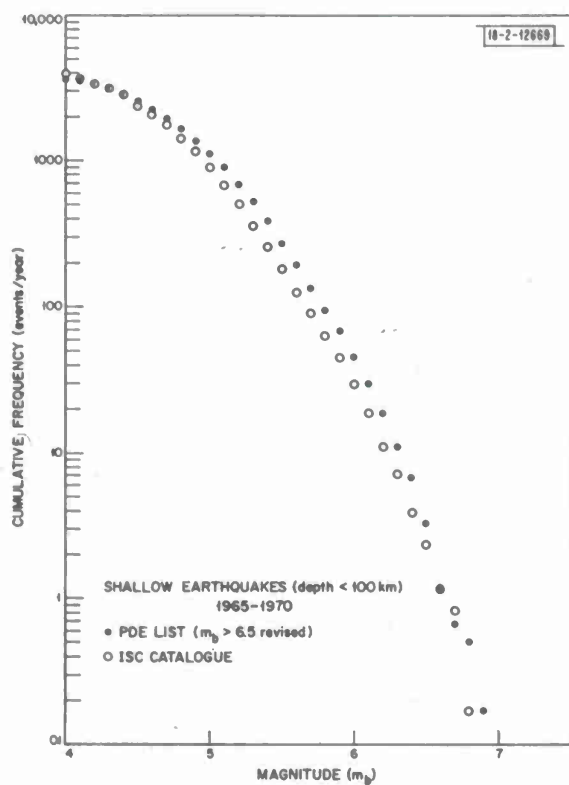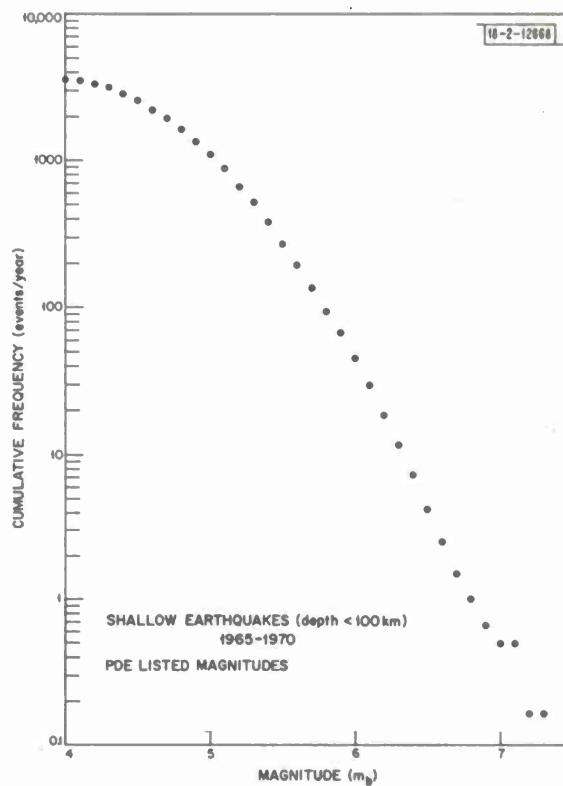
Fig. I-9. Frequency-magnitude curves for 1965-1970 (inclusive) for ISC Catalogue, and for PDE Catalogue using revised values of m_b for those events with $m_b > 6.5$.

19
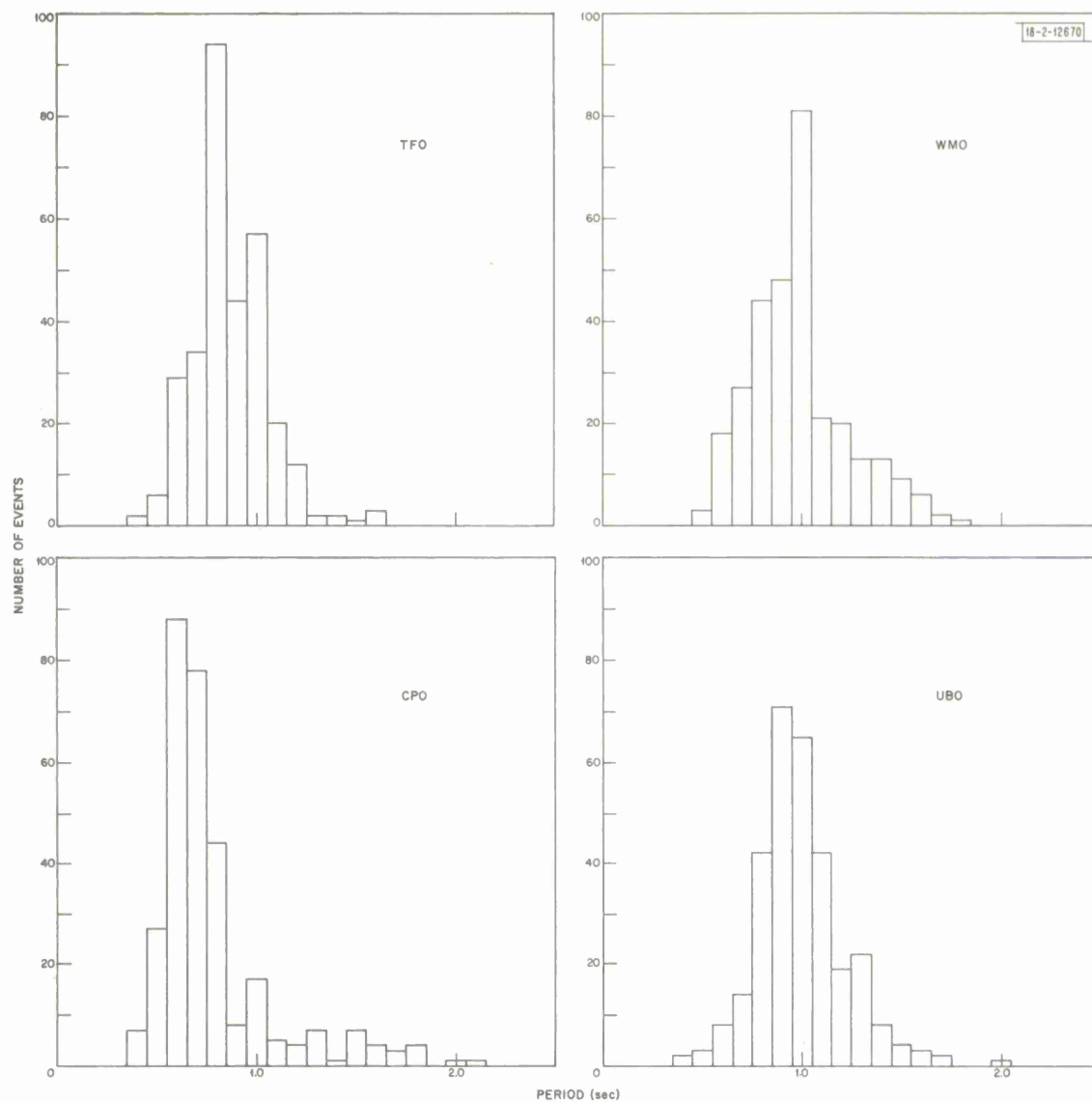
Fig. I-10. Histograms of reported periods of P-wave arrivals at Vela array stations CPO, TFO, UBO, and WMO for 302 events in 1965 Rat Island sequence.
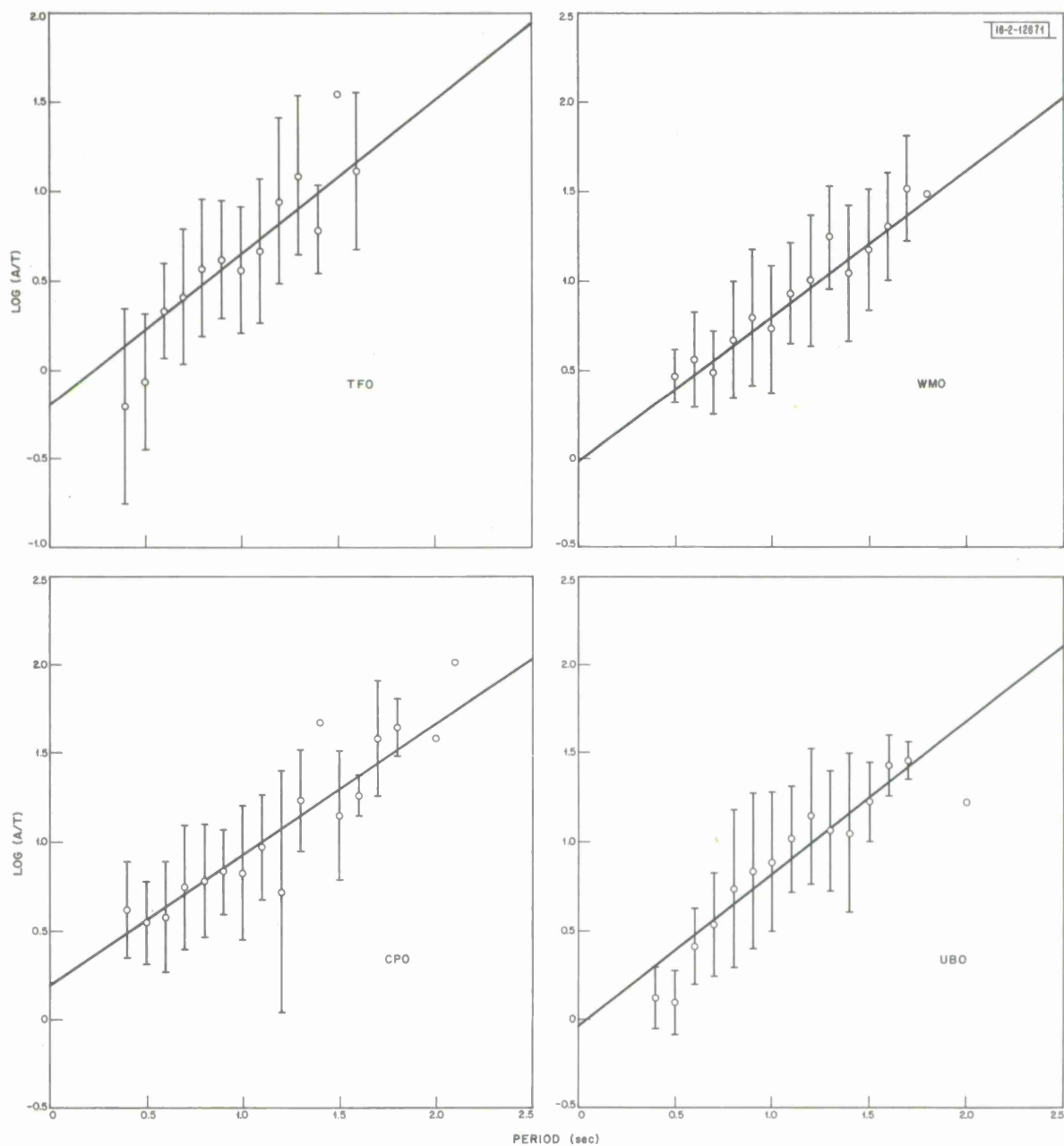
Fig. I-11. Variation of log (A/T) with period T for Rat Island events at four stations considered. Each point gives mean value of log (A/T) at each period, and bar indicates its associated standard deviation.
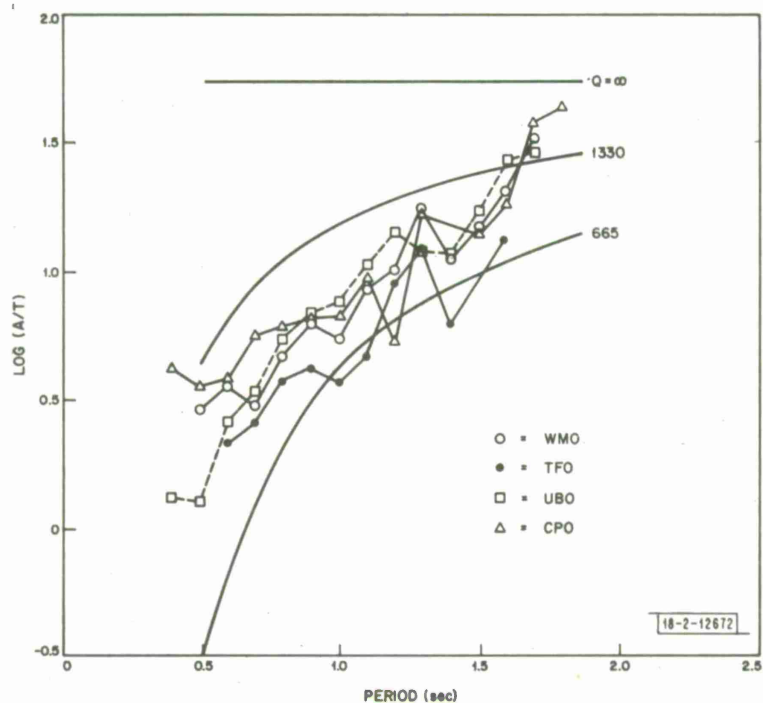
Fig. I-12. Mean values of log(A/T) as a function of period (from Fig. I-11) at CPO, TFO, UBO, and WMO. Also shown is variation of attenuation [expressed as that of log(A/T)] with period for mean path Q values of ∞, 1330, and 665.

II. EARTH STRUCTURE AND SCATTERING

A. ATTENUATION OF SHEAR ENERGY IN THE MANTLE FROM NORMAL MODE ANALYSIS

Measurements of Q for a large number of modes of free oscillation could provide the data necessary to constrain models of Q vs depth in the earth. However, until now, Q values had been obtained for only a relatively small number of modes (e.g., Smith,[1] Dratler et al.[2]). Thus, meaningful results could not be expected from inversion of these poor-quality data.[3]

A recent advance in the study of normal modes is the technique of "phase equalization," first used by Mendiguren.[4] The improved phase-equalization technique used by Gilbert and Dziewonski (called "stacking") resulted in the extraction of multiplet shapes for hundreds of modes that had not been detected before.[5] It was expected then that "stacking" might also make it possible to measure Q from the multiplet shapes, and thus greatly increase the size of the data set of Q values for normal modes. Numerous examples of multiplet shapes and a detailed description of "stacking" and "stripping" techniques can be found in Gilbert and Dziewonski.[5] A good "stack" shows a peak corresponding to the eigenperiod of the particular mode, and the shape of the stack approximates the spectral shape of this mode. The shape depends upon the attenuation and can be used to measure Q (see Ref. 6).

We have measured Q values for nearly 500 modes of free oscillation by fitting a resonance curve of the form of Eq. (II-1) to each stack. The stack for the kth normal mode is a good approximation of the resonance curve, or spectral peak:

$$\left| C_k(\omega) \right| = [\alpha_k^2 + (\omega_k - \omega)^2]^{-1/2} \tag{II-1}$$

where

$$\alpha_k = \omega_k / 2Q_k \quad .$$

Since we had reasonable starting values for ω_k and Q_k, the least-squares process converged after several iterations to give the best-fit Q for each stack. Figure II-1 shows examples of spectral stacks and the curves that were fitted to them. We note that Q values obtained in this way represent the minimum Q for each mode (multiplet), since "splitting" due to the earth's rotation, ellipticity, and lateral heterogeneities broadens the spectral peaks.

For this study, we used the data set of Gilbert and Dziewonski[5] which consists of spectra from 211 recordings of the 1963 Peru-Bolivia and 1970 Colombia earthquakes; individual recordings have an average length of about 17 hr.

Although the center frequencies could be estimated for over 800 modes,[5] only 477 stacks were of sufficient quality to attempt the measurement of Q. From this data set, we consider the most reliable Q measurements and coherence of the Q values obtained for adjacent modes to be for 197 modes — based upon the appearance of the stacks. This includes 49 toroidal modes (only 6 of the fundamental mode, but overtones up to $_5T_\ell$) and 148 spheroidal (with 40 $_0S_\ell$, $13 \leqslant \ell \leqslant 66$). The overall period range of our data is from about 500 to 80 sec.

The measured Q values for the fundamental spheroidal mode, $_0S_\ell$, agree well with published values determined by other methods; our measurements fall within the scatter of other data for spheroidal modes and long-period Rayleigh waves (Fig. II-2). We expect that the results

		Q Model	LMS Q-Model
		(this report)	(Smith[1])
Mode	Q Observed		
$_0S_0$	7500 (Ref.12)	6402	8816
$_2S_0$	704 (Ref.2)	1243	3156
$_4S_0$	1173 (Ref.2) 790 (Ref.1)	1032	2196
$_5S_0$	938 (Ref.2) 1570 (Ref.1)	1011	2047
$_6S_1$	613 (Ref.2)	619	1482
$_8S_1$	420 (Ref.2)	920	2028
$_{11}S_1$	1341	1072	2289
$_{11}S_4$	652	669	1426
$_{13}S_1$	1573	940	1942
$_{25}S_5$	791	1010	1579

TABLE II-1

OBSERVED Q VALUES COMPARED WITH THOSE COMPUTED BY TWO DIFFERENT Q MODELS OF THE MANTLE[†]

† Note that model "LMS" predicts values higher than observed. Refer to Fig. II-2 for the parameters of these models. Numbers in parentheses following values of Q observed indicate sources of data other than this study.

presented here may better represent the average attenuation properties of the earth. Each of our Q measurements is based upon many seismic recordings, while previously reported values are based on the information in single records.

Several inversions were performed to derive Q models of the mantle. The present set of data, augmented by Q values for 26 long-period modes listed by Smith,[1] was inverted to obtain a two-layer Q_μ model of the mantle. The result for these 233 modes was Q_μ = 120 in the upper 670 km of the mantle, and Q_μ = 240 in the lower 2200 km. The variance of $1/Q$ was such that within one standard deviation of $1/Q$, Q could vary from 107 to 133 in the top layer and from 200 to 300 in the lower layer. Using our data alone, or our data without a correction for record truncation, did not make a significant difference in the result of the inversion. Observations and the theoretical results for our Q_μ model are shown in Figs. II-2 and II-3 for the modes $_0S_\ell$, $_1S_\ell$, $_2S_\ell$, $_0T_\ell$, and $_1T_\ell$. Values for a number of high-Q overtones are listed in Table II-1. A three-layer inversion using the same data gave very similar results for the lower mantle, and in the top layer (to a depth of 300 km) gave a Q_μ of 86 (69 ⩽ Q ⩽ 120).

We have been assuming that $1/Q_K$, the dissipation due to pure dilatation, is zero and that the intrinsic Q is independent of frequency. The former assumption is justified by the work of Birch,[7] and we tested the latter by performing a series of inversions of our data within different frequency bands. Our data, when combined with a few observations of long-period modes listed by Smith,[1] cover a period range from about 1200 to 80 sec. Since we have many observations of overtones, then, in any given frequency band there are several modes which are sensitive to the different parts of the mantle, enough so that inversions may be performed using only modes with eigenfrequencies in the same frequency bandwidth. We performed two-layer inversions of the data within 16 different frequency bands, each of a width of 0.005 rad/sec. A plot of the results of these inversions vs frequency, including the standard-deviation error bars, showed that any frequency dependence of the intrinsic Q within the range of our data must be very small (Fig. II-4).

The fairly low value of Q_μ for the lower mantle (200 to 300) implied by our inversions contrasts with the higher values given by other published Q models (e.g., Smith,[1] Kovach and Anderson[8]). Our Q model is consistent with some more recent observations of multiple core reflections of ScS which imply an average Q of about 300 for the whole mantle.[9] We have not yet been able to quantify the bias in our results due to splitting. Some preliminary calculations indicate that this may not be as large as some have expected. Thus, if further work substantiates our estimates of Q in the lower mantle, this will have some important implications. First, there may be some frequency dependence of the intrinsic Q which would explain the higher values obtained for higher frequency body waves; and second, the lower mantle may be at a high enough temperature, or low enough viscosity, to undergo convection.

R. V. Sailor[†]
A. M. Dziewonski

B. MODELING RAYLEIGH-WAVE PHASE VELOCITIES AND AMPLITUDES IN EURASIA

In the last SATS,[10] the results of a study of how well azimuthal deviations of Rayleigh-wave arrivals at NORSAR could be predicted by ray tracing in a laterally heterogeneous earth were reported. This work is being continued, and considerable refinements have been made in the

† Department of Geological Sciences, Harvard University, Cambridge, MA 02138.

grid of phase velocities across Eurasia used in the ray tracing. In particular, different struc-
tural types such as shield, platform, oceanic, and foldbelt have been incorporated as well as
the variation of crustal thickness. The various models used have been taken from a summary
of inversions of observed dispersion.[13] Rift-type structures have not been included, although
they are obviously present in the Baikal rift zone and Rhinegraben, for example. Much of the
western U.S. appears to be of this type and there must exist large rift regions in Eurasia which
cannot be identified from surface geology. The grid is specified at $2°$ intervals in latitude and
longitude, and cubic splines are used during the ray tracing to interpolate phase velocity and its
spatial derivatives at intermediate points and to ensure their continuity.

We report the results of the ray tracing at 40-sec periods, for which typical grid velocities
are 3.88 (oceanic), 3.95 to 4.05 (shield), 3.35 to 3.85 (foldbelt), and 3.5 to 4.0 (platform) km/sec.
Variations in velocity for a given structure are caused by differences in crustal thickness. The
lower velocities for foldbelt and platform correspond to the Himalayas and the Tibetan platform,
respectively.

In the previous SATS,[10] the results of a study of surface waves from earthquakes in the Tien
Shan and Pamir mountains were reported. A continuation of this study has yielded mechanisms
for these earthquakes from the phase and amplitude spectra observed at a network of stations
and also the Rayleigh-wave phase velocities for the event-station paths.[14] These results place
constraints upon the velocity grid used, and it is also possible that the amplitude variations can
be partially explained by velocity changes causing focusing or defocusing of the rays.

Ray tracing has been carried out from the point (39°N, 75°E) in the Pamir mountains. The
results are shown in Fig. II-5, a polar plot centered at the source and extending to 50° distance.
Also shown are the locations of the stations at which phase velocity and amplitudes have been
measured. On this projection, great-circle paths from the origin are straight lines, and it is
clear that considerable deviations are caused by lateral variations in velocity. Figure II-6 shows
on a larger scale the rays as they propagate out to a distance of 15°. The contours are the wave-
fronts at phase delays of 100, 200, 300, and 400 sec due to propagation effects. In Figs. II-5
and II-6, the rays leave the source at 5° increments in azimuth from 0 to 355°. The low phase
velocities in the Himalayas (lower right of Fig. II-6) can be seen to cause considerable delays
and focusing of the rays. The extremely large deviations to the east in Fig. II-5 are due to the
fairly rapid transition from the central Asian mountain ranges (velocity ~ 3.7 km/sec) to the
platform region of North China (~4.0 km/sec). The rays here are incident upon the boundary
at low incidence angles and thus reflection occurs from the higher velocity region, causing high
azimuthal deviations. Rays to Northern Scandinavia (NW azimuth in Fig. II-5) are slightly fo-
cused by both near-source velocity variations and by the Ural mountains; the latter have been
assigned a velocity of ~3.85 km/sec as opposed to the platform region on each side (4.0 km/sec).
At sufficiently low angles of incidence, deviations of several degrees may be caused by rela-
tively small velocity variations.

The ray tracing results have been used to predict phase velocities (distance traveled along
ray/phase delay) and amplitude variations caused by nongeometric spreading effects at 17 WWSSN
stations for comparison with observation. The fit of the predicted phase velocities to those ob-
served is remarkably good [Fig. II-7(a)], and the substantial decrease in apparent phase velocity
as the rays sample more of the Himalayan and Chinese mountain belt (70° to 120° azimuth) is
well supported by the data. A slight reduction in grid velocities in China should give even better
agreement. The variation of velocity across Europe and Western Asia (260° to 330° azimuth) is
also well predicted by the model.

The amplitude variation caused by nongeometric spreading has been calculated simply by taking the ratio of azimuthal spread as rays leave the source region to that in the vicinity of the station. The observed 40-sec amplitudes at each station have been corrected for source radiation pattern, geometric spreading, and an average Q of 200. Predicted and observed amplitudes at each station are shown in Fig. II-7(b).

The predicted effects can be seen to be quite dramatic, involving a factor of six in amplitude. The observed variation is even larger, due to a combination of nongeometric spreading and differences in Q. The large amplitude variation at European stations (260° to 330° azimuth) seems likely to be caused by lateral velocity variations. The fit for stations in Asia is much poorer, but it may well be that the revision of grid velocities in China required to fit the phase velocities better will improve the situation.

The degree to which the observed phase velocities can be predicted is very encouraging and it is hoped that, by suitable modification to the grid, the amplitude variations can be better modeled.

R. G. North
H. J. Patton

C. WAVENUMBER ANALYSIS OF SEISMIC CODAS FROM NOVAYA ZEMLYA EXPLOSIONS

In the previous SATS,[10] polarization studies of three-component data from six Novaya Zemlya explosions showed that each coda contains a large number of impulsive body phases scattered by inhomogeneities in and out of the diametral plane.

We are now investigating the wavenumber structure of the seismic coda using subarray data for one of the six explosions which occurred on 14 October 1969 at 7:00:06 GMT with an m_b of 6.1. The extended E3 subarray at LASA was selected to study the coda because its aperture of 20 km, shown in Fig. II-8, gives significantly better wavenumber resolution than the other subarrays which have apertures of 7 km. The theoretical beam pattern of the E3 subarray is displayed in Fig. II-9.

Figures II-10, II-11, and II-12 show 3 min. of data recorded on the E3 subarray, filtered in three narrow bands centered at 0.7, 1.0, and 1.3 Hz, respectively. At the bottom of each figure is displayed the unfiltered center trace from sensor 10.

The only phases after P predicted by travel-time tables are PcP and PP. The expected arrival times of these time phases are shown in Figs. II-10, II-11, and II-12 by dashed lines. However, it is clear from these filtered traces that other coherent phases exist which are at least as strong as the predicted phases.

In order to determine the phase velocity and azimuth of the coherent arrivals within the coda, high-resolution wavenumber analysis (described by Capon[15]) was applied to each set of filtered traces using the center frequency of the passband. A cosine tapered window 10 sec long was used to compute each wavenumber spectrum. Successive windows were made to overlap by 5 sec so that no strong arrivals would be missed in the analysis.

Figure II-13(a-d) shows the results from nearly 3 min. of coda. Each plotted symbol was obtained from high-resolution analysis of a 10-sec window of data. The time at which each symbol is plotted indicates the center of the window.

Figures II-13(a) and (b) display the phase velocity and azimuth, respectively, of the wavenumber peak, if at least 2 dB higher than the background level on the plot. Figure II-13(c) shows

the amount of power that the wavenumber peak exceeds the background level, and in Fig. II-13(d) the average power of all 25 sensors is plotted for each window.

The phases P, PcP, and PP produce peaks in the wavenumber plots, but there are some interesting variations with frequency. The P phase arrives with a phase velocity of 18.5 km/sec for all three frequencies; however, there is a monotonic decrease in arriving azimuth with frequency from 12° to 0°. The wavenumber plot at 1 Hz (Fig. II-14) shows a very sharp peak at 18.7 km/sec, which is a higher velocity than the expected velocity of 16 km/sec for P waves at $\Delta = 60°$. This velocity shift is not due to frequency window leakage described by Smart[16] because it is reproducible at all three frequencies.

The PcP phase produces strong wavenumber peaks at all three frequencies; however, the phase velocities do not agree. At 1.3 Hz the peak occurs at 24.8 km/sec (Fig. II-15), a little less than the expected 27.8 km/sec, whereas at 0.7 and 1.0 Hz the wavenumber peaks are much sharper with velocities ~18.5, similar to the P velocity. Thus, the coda at this time is a mixture of P-type arrivals overlaying the PcP phase, making it difficult for the wavenumber analysis to extract the PcP wave unambiguously.

The PP arrival produces strong wavenumber peaks at 0.7 and 1.0 Hz in Fig. II-13(c), but not at 1.3 Hz. The corresponding peak velocities are ~10 to 13 km/sec, agreeing with a predicted velocity of 12.5 km/sec. In Fig. II-16, the wavenumber picture for the PP phase is shown for 0.7 Hz.

In Fig. II-13(c), we see that other strong wavenumber peaks occur at various times in the coda, especially for 0.7 Hz. These peaks correspond to peaks in the average power across the array shown in Fig. II-13(d). Although it is difficult to interpret these peaks unambiguously, it appears that most of these unknown phases are P-type which are generated near Novaya Zemlya within a narrow azimuthal range 5° to 10° from LASA. Some arrivals have velocities which vary from PP- to PcP-type arrivals, due to scattering far from LASA, but there is no evidence of backscattered body or surface waves generated locally near LASA.

C. W. Frasier
M. Yang

D. ADAPTIVE DECONVOLUTION OF NOVAYA ZEMLYA SHORT-PERIOD DATA

Deconvolution or, equivalently, prediction error filtering offers a means of searching for reverberations in seismic data[17] as well as enhancing first motion.[18] Adaptive deconvolution accomplishes the same effects while making as few assumptions as possible about the statistics of the input time series. The filter adapts itself, learning as it proceeds through the data, and is thus able to follow the behavior of nonstationary processes. This characteristic is attractive in investigations of the seismic coda because both near-source and near-receiver reverberations, as well as scattering from distant parts of the travel path, may be involved.

The data for this study consist of three-component, short-period recordings of five presumed explosions from Novaya Zemlya. These data were recorded at the LASA D2 subarray and were used previously[10] in an evaluation of polarization filters. The locations of the events are shown in Fig. II-17.

The method is an application of the Widrow algorithm[19] which was developed by Griffiths et al.[20] for use in petroleum exploration. It can be expressed

$$\vec{F}(t \pm 1) = \vec{F}(t) + \mu[x(t + \gamma) - \hat{x}(t + \gamma)] \vec{X}(t) \tag{II-2}$$

28

where $\vec{F}$ is the vector of filter coefficients, x is the input, $\hat{x}$ is the predicted value γ time units ahead, and $\vec{X}$ is a vector of past inputs. The constant μ is a learning-rate constant related to a dimensionless parameter α by:

$$\mu = \frac{\alpha}{L\sigma_x^2} \quad , \quad 0 < \alpha < 2 \qquad (\text{II-3})$$

where L is the number of filter points, and σ_x^2 is the variance of the input data over the last filter length. Griffiths et al.[20] give a detailed discussion of how to choose α and its effect on the filter response. The value α = 0.5 was used in this study.

The only other two parameters in the algorithm are the filter length L and the prediction span γ. These were determined experimentally. Using the vertical component of Event 1 and varying the filter length showed little change in the corresponding outputs beyond L = 20 points or 2 sec. Furthermore, the prediction error grew rapidly for any prediction span beyond 1 unit or 0.1 sec. Consequently, the values L = 20 and γ = 1 were used to produce the results given below. The usual interpretation of these choices[20] is that the basic wavelet being deconvolved is less than 1 sec long and that the reverberation time is on the order of 0.5 sec.

Following Griffiths et al.,[20] the data were filtered with the filter adapting first in a backward direction and then, using the final filter as a starting value, in a forward direction. Both results were stacked to produce the output. The reason for this approach is that, by the time the filter is ready to go forward through the data, it has already learned much from the backward pass.

Some of the results for Events 1 and 2 are shown in Figs. II-18 and II-19. The principal feature in Fig. II-18, which shows the vertical component plotted in an expanded time scale, is a large negative spike occurring 1.8 sec after the P arrival. This phase was seen in four of the five events processed, but only on the vertical components. It corresponds to a LASA P wave reverberation arriving at approximately 1.7 sec predicted by Frasier[21] from the USGS3 crustal model. Unfortunately, events with larger magnitudes recorded at LASA exhibit severe clipping, which renders the polarity of this phase unobservable. Figure II-19 shows all three components and their filtered counterparts from Event 2. As can be seen, adaptive deconvolution removes considerable coda energy arriving later than 10 sec after the P wave. The negative spike at 1.8 sec can also be seen in the filtered vertical component of this event.

The conclusions of this study are that adaptive deconvolution is selective enough to enhance receiver reverberations and, at the same time, remove considerable energy from the short-period coda. An obvious implication of the latter conclusion is that much of this coda energy is predictable in terms of that which arrives one filter length (2 sec) before it, and that this situation does not change faster than the filter can adapt. Thus, much of the short-period coda energy in these seismograms appears to be correlated enough to be deconvolved out, which tends to support the earlier conclusion by Greenfield[22] that it is generated by scattering in the source region.

D. W. McCowan

E. REFLECTION OF PKPPKP FROM THE 600-km DISCONTINUITY

With the use of array beamforming and velocity spectral analysis (VESPA), we are undertaking an investigation and study of reflections from the 600-km discontinuity. Given a sufficient number of these reflections from a large population of events within a given area, it should be possible to construct a model of the nature of the reflecting horizon. The point of reflection will

be located about 240° from the epicenter of the event along the array-event azimuth. For LASA, for example, the best events to use in this experiment would lie about 76° from LASA along any azimuth. The resulting PKPPKP reflection would therefore occur about 218° from the event along the same azimuth. Because of the location of LASA with respect to the seismic zones, most of these reflections will occur in the ocean basins off the coast of Antarctica. By selecting events in the Japan-Kuril region, it should be possible to map the reflecting 600-km boundary across the plate boundary of the Atlantic-Indian-Pacific Basin regions.

Figure II-20 shows an example of a 600-km reflection arriving about 2.5 min. before PKPPKP from a large Novaya Zemlya explosion. The apparent velocity of the 600-km discontinuity reflection is about 2.1 sec/deg, while the apparent velocity of the PKPPKP surface reflection is at about 2.4 sec/deg. The reflection point for this event lies in the Southeast Pacific Basin, off the coast of Antarctica. Because of the relative success of the velocity spectral analysis process in detecting the signals from the reflecting boundary, we plan to process a large number of events from the Kuril-Japan region to investigate the nature of the reflective boundary within a small area.

R. M. Sheppard

F.   LATERAL STRUCTURE FROM SPATIAL CORRELATION FUNCTIONS

As part of the U.S.A.–U.S.S.R. joint program on earthquake prediction, previous work[10] on lateral structure has been extended to include data from seismic networks in California and Garm, U.S.S.R. In order to standardize analysis of scattered signals, a set of earthquakes in the Japan and Kamchatka regions with $m_b \geqslant 5.2$ are being studied by determining the spatial correlation functions of the P waveforms, of the time residuals, and of the log-amplitude residuals. These correlation functions are calculated as functions of station separation and of distance between events. Further, correlation functions have been defined for distances measured parallel to the ray path and for distances perpendicular to the ray path; these functions have been termed, respectively, the parallel and transverse correlation functions. A typical set of correlation functions for LASA is shown in Figs. II-21 and II-22. Theoretical considerations predict that, if scattering is due to isotropic random inhomogeneities, the parallel correlation function will decrease more slowly than the transverse correlation coefficient. This is not evident in Figs. II-21 and II-22, indicating that the assumption of isotropic random inhomogeneities is unjustified. Similar results were obtained for the preliminary data sets from the other networks. Currently, the remaining correlation functions for all networks are being calculated.

J. Scheimer

G.   SEISMIC EXPERIMENT IN TRANSMISSION HOLOGRAPHY

Successful ultrasonic model experiments suggest a seismic holography experiment utilizing NORSAR data. For this experiment, two events have been chosen at moderate distances (77.2°, 88.0°) which had particularly sharp and clear P arrivals. Both events have nearly the same azimuth as seen from NORSAR, but one event (in the Japan region, 30 October 1971) is relatively deep (393 km) while the other (in the Kamchatka region, 11 August 1972) is relatively shallow (33 km).

The preliminary processing of these events consists of filtering records from the central seismometers of each subarray in three frequency bands: 0.5 to 0.75 Hz (Band 1), 0.75 to 1.1 Hz (Band 2), and 1.1 to 1.6 Hz (Band 3). For each of these filtered records, amplitude and phase

measurements were tabulated. Prior to applying the processing techniques developed in the model experiments, the data were examined for information they might yield on characteristics of the medium, and appropriateness of the frequency bands chosen.

Visualizing each of the frequency bands contributing a different "color" to a hologram draws attention to the problem of contrast between each "color." If the frequency bands are incorrectly chosen, the resulting "picture" will be either (washed out) low contrast (due to the similarity of adjacent frequencies) or will have such dissimilarity between adjacent frequencies that the resulting monochromatic "pictures" will be totally unrelated to one another, producing a composite that appears random. The appropriateness of the choice of frequency bands can be examined by calculating the correlation coefficient between the measurements of variations in log-amplitude for each adjacent band. A correlation coefficient greater than about 0.95 indicates that the two sets of data are so alike that little or no contrast can be expected. Alternatively, a correlation coefficient less than about 0.5 indicates that the two sets of data are so dissimilar that they would not contribute significantly to each other when combined. An optimum range of correlation coefficients might be from 0.75 to 0.9. Calculated correlation coefficients $[\rho_{ij} = \rho(\ln A_i : \ln A_j)]$ between the filtered records of the Kamchatka event were:

$$\rho_{12} = 0.837 \quad , \quad \rho_{23} = 0.841 \quad , \quad \rho_{13} = 0.653 \quad .$$

Rms variations for the three bands were 0.371, 0.495, and 0.640, respectively. Mean square values were 0.137, 0.245, and 0.410. These values for the correlation coefficients indicate that the chosen frequency bands should provide sufficient, but not excessive, contrast.

The reconstruction techniques to be applied to these data have been tested in concert with researchers at the Institute of Physics of the Earth in Moscow by application to data from an ultrasonic model experiment. The model (Fig. II-23) consisted of an epoxy block in which was embedded an aluminum cross. The image[23] was reconstructed by the use of an amplitude-only holographic technique using computer reconstruction rather than the laser reconstruction technique which has been widely used in the field of acoustic holography.[24] Figure II-24 shows the results of this reconstruction of the wavefront immediately above the ξ-η plane which contains the cross. Since the source is continuous, the signal (and reconstructed image) is heavily contaminated by surface waves and multiple reflections. Currently planned are experiments using an impulsive source in order to fully test the numerical techniques prior to applying them to the NORSAR data.

<div align="right">J. Scheimer</div>

REFERENCES

1. S. W. Smith, "The Anelasticity of the Mantle," Tectonophysics 13, 601-622 (1972).

2. J. Dratler, W. E. Farrell, B. Block, and F. Gilbert, "High-Q Overtone Modes of the Earth," Geophys. J. R. Astr. Soc. 23, 399-410 (1971).

3. G. Backus and F. Gilbert, "The Resolving Power of Gross Earth Data," Geophys. J. R. Astr. Soc. 16, 169-205 (1968).

4. J. Mendiguren, "High Resolution Spectroscopy of Earth's Free Oscillations Knowing the Earthquake Source Mechanism," Science 179, 179-180 (1973).

5. F. Gilbert and A. M. Dziewonski, "An Application of Normal Mode Theory to the Retrieval of Structural Parameters and Source Mechanisms from Seismic Spectra," Phil. Trans. R. Soc. London 278A, 187-269 (1975).

6. R. V. Sailor and A. M. Dziewonski, "Measurements of Q for the Earth's Free Oscillations," Trans. AGU 56, 403 (1975) (Abstract).

7. F. Birch, "Velocity and Attenuation from Resonant Vibrations of Spheres of Rock, Glass, and Steel," J. Geophys. Res. 80, 756-764 (1975).

8. R. L. Kovach and D. L. Anderson, "Attenuation of Shear Waves in the Upper and Lower Mantle," Bull. Seismol. Soc. Am. 54, 1855-1864 (1964).

9. W. J. Best, L. R. Johnson, and T. V. McEvilly, "ScS and the Mantle beneath Hawaii," Trans. AGU 55, 1147 (1974) (Abstract).

10. Seismic Discrimination SATS, Lincoln Laboratory, M.I.T. (30 June 1975), DDC AD-A014793/4.

11. H. Kanamori, "Velocity and Q of Mantle Waves," Phys. Earth Planet. Inter. 2, 259-275 (1970).

12. N. F. Ness, J. C. Harrison, and L. B. Slichter, "Observations of the Free Oscillations of the Earth," J. Geophys. Res. 66, 621-629 (1961).

13. L. Knopoff, "Observation and Inversion of Surface Wave Dispersion," Tectonophysics 13, 497-519 (1972).

14. H. Happon and K. Aki, "Surface Wave Generation and Propagation from Earthquakes in Central Asia" (in preparation).

15. J. Capon, "High-Resolution Frequency-Wavenumber Spectrum Analysis," Proc. IEEE 57, 1408-1418 (1969), DDC AD-696880.

16. E. Smart, "Erroneous Phase Velocities from Frequency-Wavenumber Spectral Sections," Geophys. J. 26, 247-253 (1971).

17. H. Mack, "Nature of Short-Period P-Wave Signal Variations at LASA," J. Geophys. Res. 74, 3161-3170 (1969).

18. J. F. Claerbout, "Detection of P-Waves from Weak Sources at Great Distances," Geophysics 29, 197-211 (1964).

19. B. Widrow, "Adaptive Filters I: Fundamentals," Stanford Electronics Laboratory Report SEL-66-126, Stanford, California (1966).

20. L. J. Griffiths, F. R. Smolka, and L. D. Trembly, "Adaptive Deconvolution I: Theory," paper presented to the annual meeting of the Society of Exploration Geophysicists, Denver, 15 October 1975.

21. C. W. Frasier, "Discrete Time Solution of Plane P-SV Waves in a Plane Layered Medium," Ph. D. Thesis, Massachusetts Institute of Technology (1969).

22. R. J. Greenfield, "Short Period P-Wave Generation by Rayleigh-Wave Scattering at Novaya Zemlya," J. Geophys. Res. 76, 7988-8002 (1971).

23. A. F. Metherell, "The Relative Importance of Phase and Amplitude in Acoustical Holography," in Acoustical Holography, Vol. 1 (Plenum Press, New York, 1969).

24. A. L. Boyer, P. M. Hirschy, J. A. Jordan, L. B. Lesem, and D. L. Van Rooy, "Reconstruction of Ultrasonic Images by Backward Propagation," in Acoustical Holography, Vol. 3, (Plenum Press, New York, 1971).
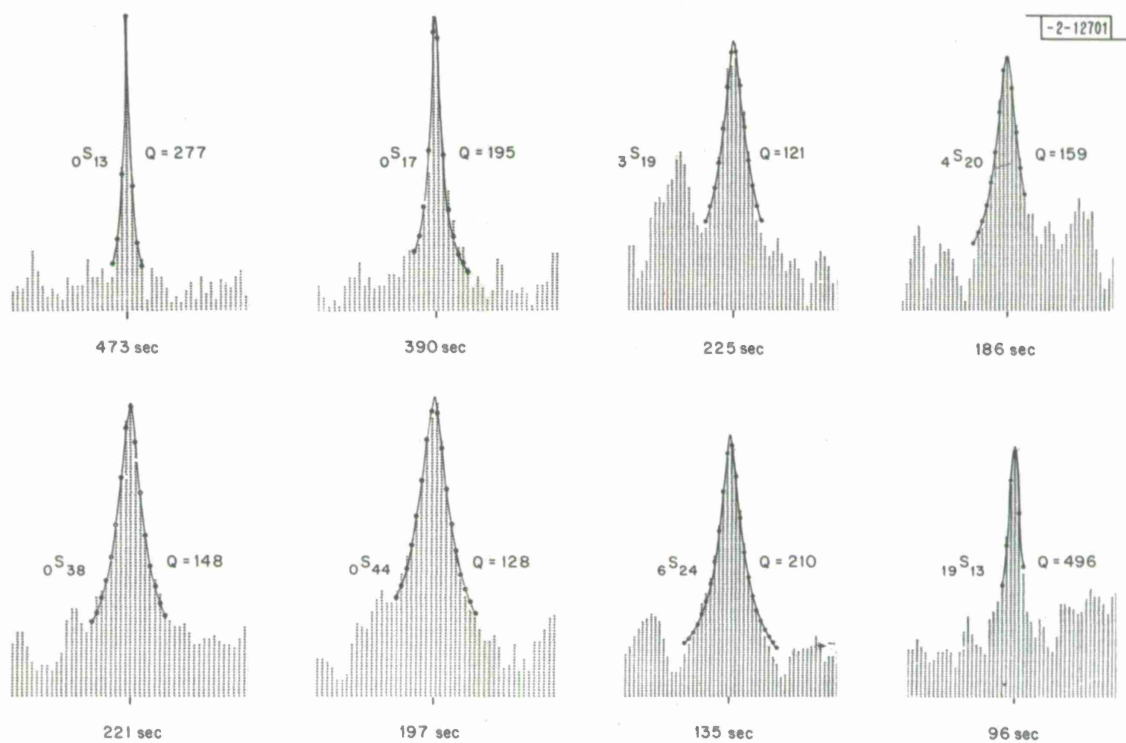
Fig. II-1. Examples of spectral stacks for spheroidal modes. Resonance curves fitted to stacks and measured Q values are shown. Each line in stack is separated by 7.6×10^{-6} Hz.
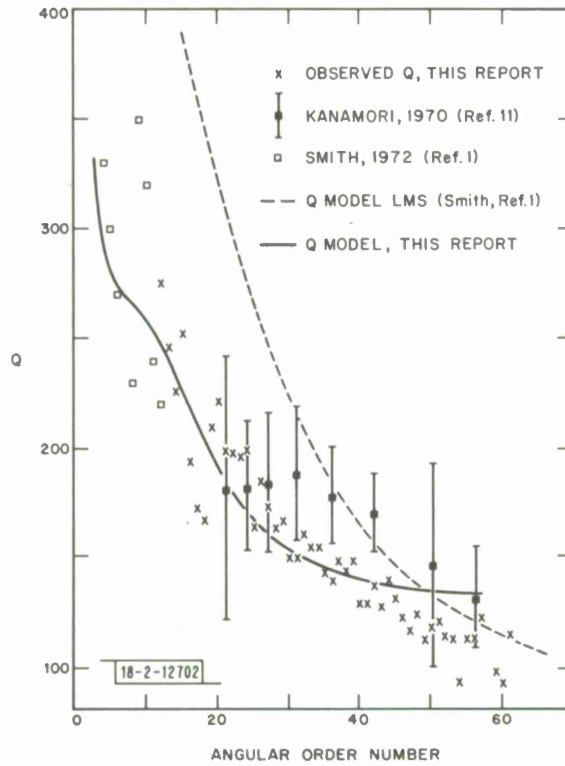
Fig. II-2. Theoretical and observed Q values for fundamental spheroidal mode, $_0S_\ell$. Dashed curve is for Q values predicted by the Q model "LMS" of Smith[1] (Q_μ = 750 from core-mantle boundary to depth of 1000 km, 375 to depth of 300 km, and 75 in upper 300 km). Solid curve is based on our two-layer Q model (Q_μ = 240 in lower mantle, 120 in upper 670 km), which was obtained by inverting Q measurements for 223 modes. Other symbols show observed Q values from this report, Kanamori,[11] and Smith.[1]
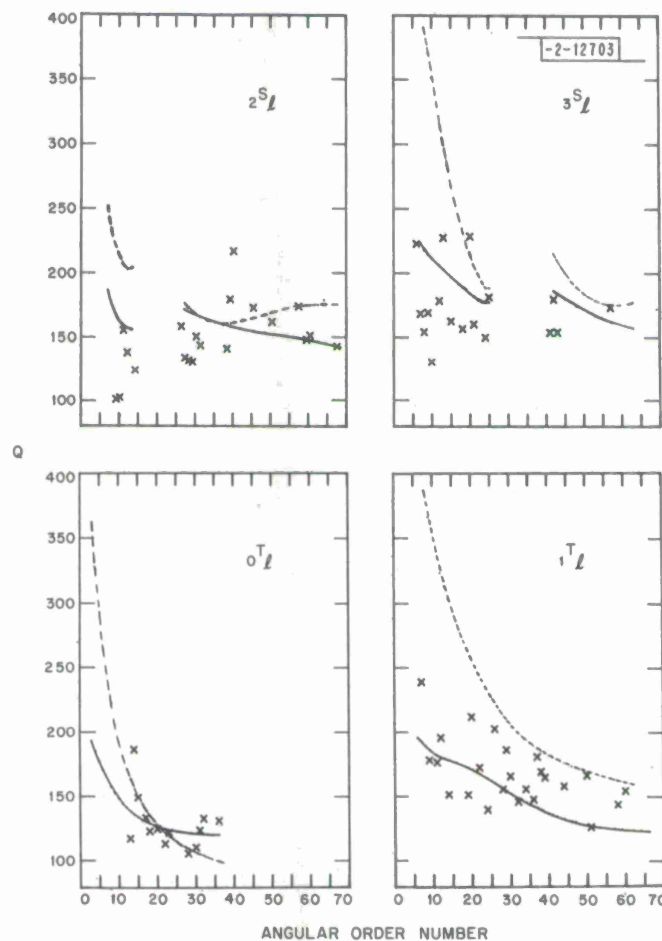
Fig. II-3. Theoretical and observed Q vs angular order number for $_2S_\ell$, $_3S_\ell$, $_0T_\ell$, and $_1T_\ell$. x's are observations from this study, dashed curves are values predicted by model "LMS," and solid curves are values predicted by our Q model (see Fig. II-2 for parameters of these models).
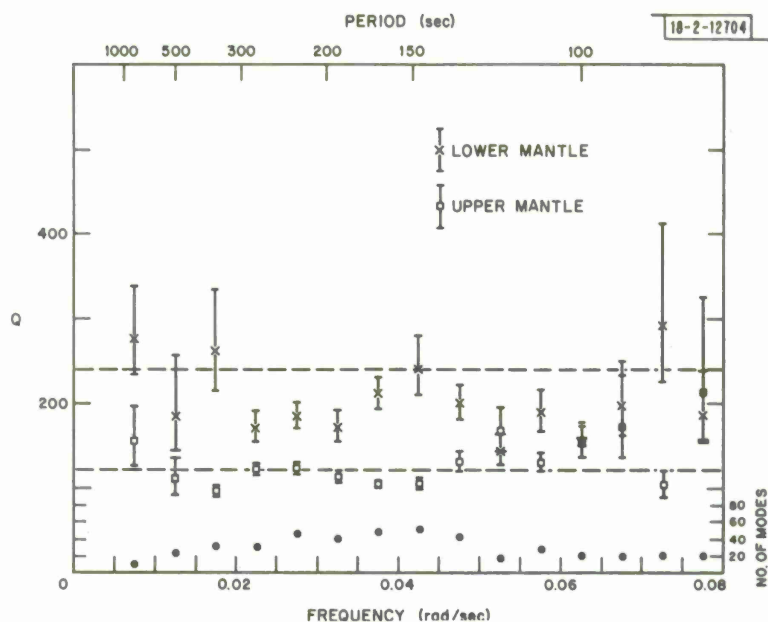
Fig. II-4. Results of inversions using modes with eigenfrequencies falling within 15 separate frequency bands. Error bars are for one standard deviation of 1/Q. Dashed lines are for Q model obtained by inversion of 223 modes. Dots along bottom of figure give number of modes used in each inversion.
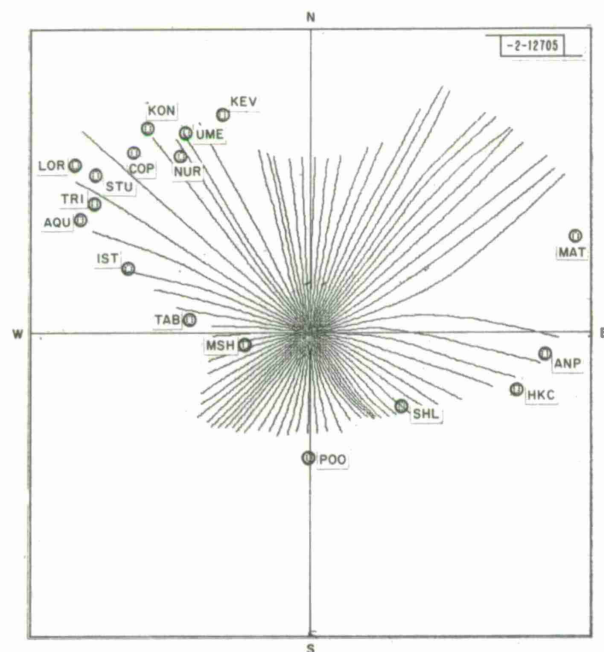
Fig. II-5. Results of ray tracing in grid of 40-sec period Rayleigh-wave phase velocities. Plot is polar projection centered at (39°N, 74°E) in Pamir mountains, and extends to 50° distance in compass directions. Rays leave source at 5° intervals in azimuth from 0° to 355°.
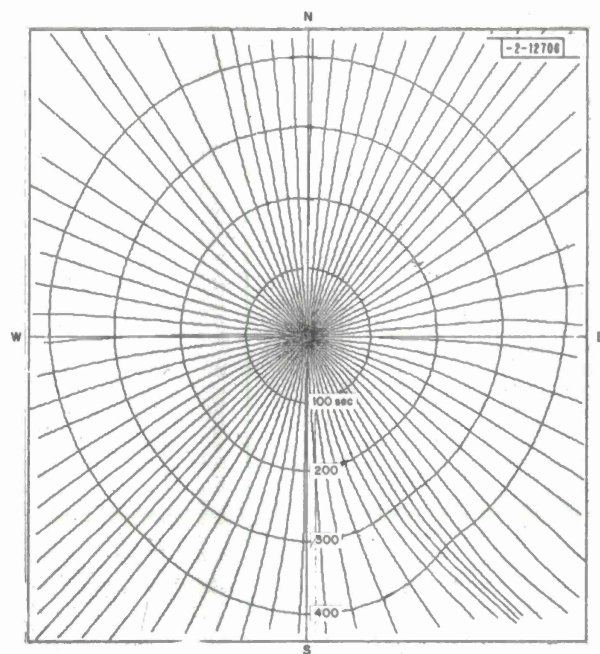
Fig. II-6. As in Fig. II-5, but to distance of only 15°. Centers
are wavefronts (equal phase delay) at delays of 100, 200, 300,
and 400 sec.
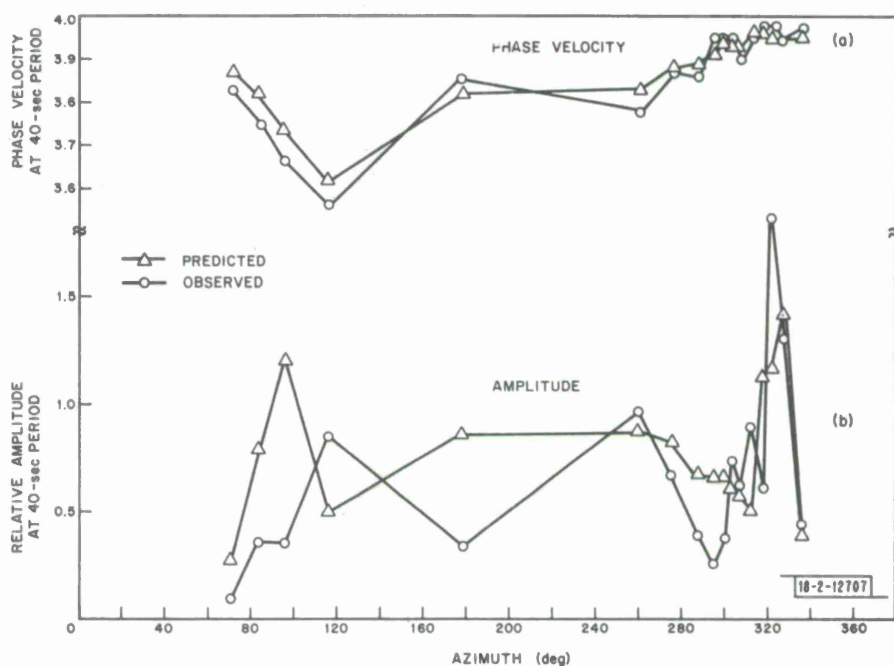
Fig. II-7. Observed and predicted 40-sec Rayleigh-wave phase velocities
and amplitudes at 17 WWSSN stations. Lines joining points do not indicate
actual variation of parameters, but are intended only to show matching
characteristics of observation and theory.
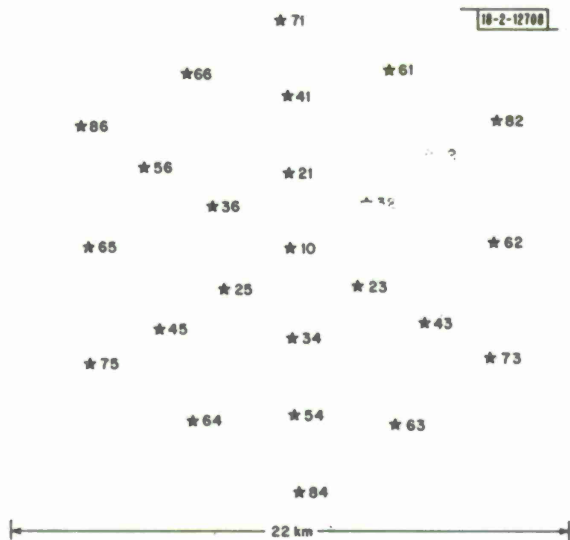
Fig. II-8.   Extended E3 subarray of LASA.
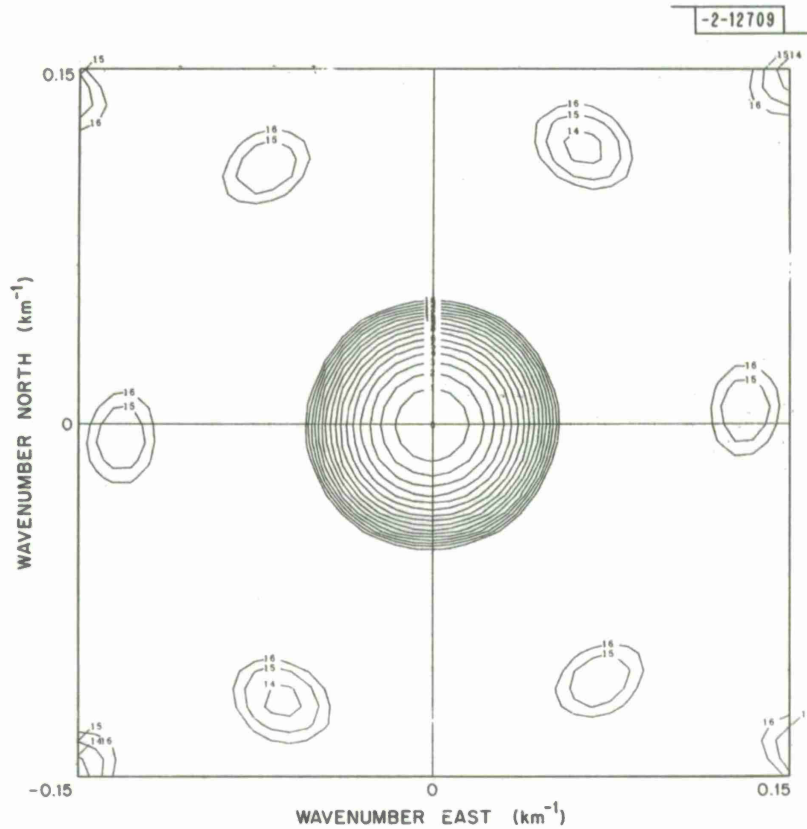
Fig. II-9.   Theoretical beam response of E3 subarray.   Contour interval is 1 dB.
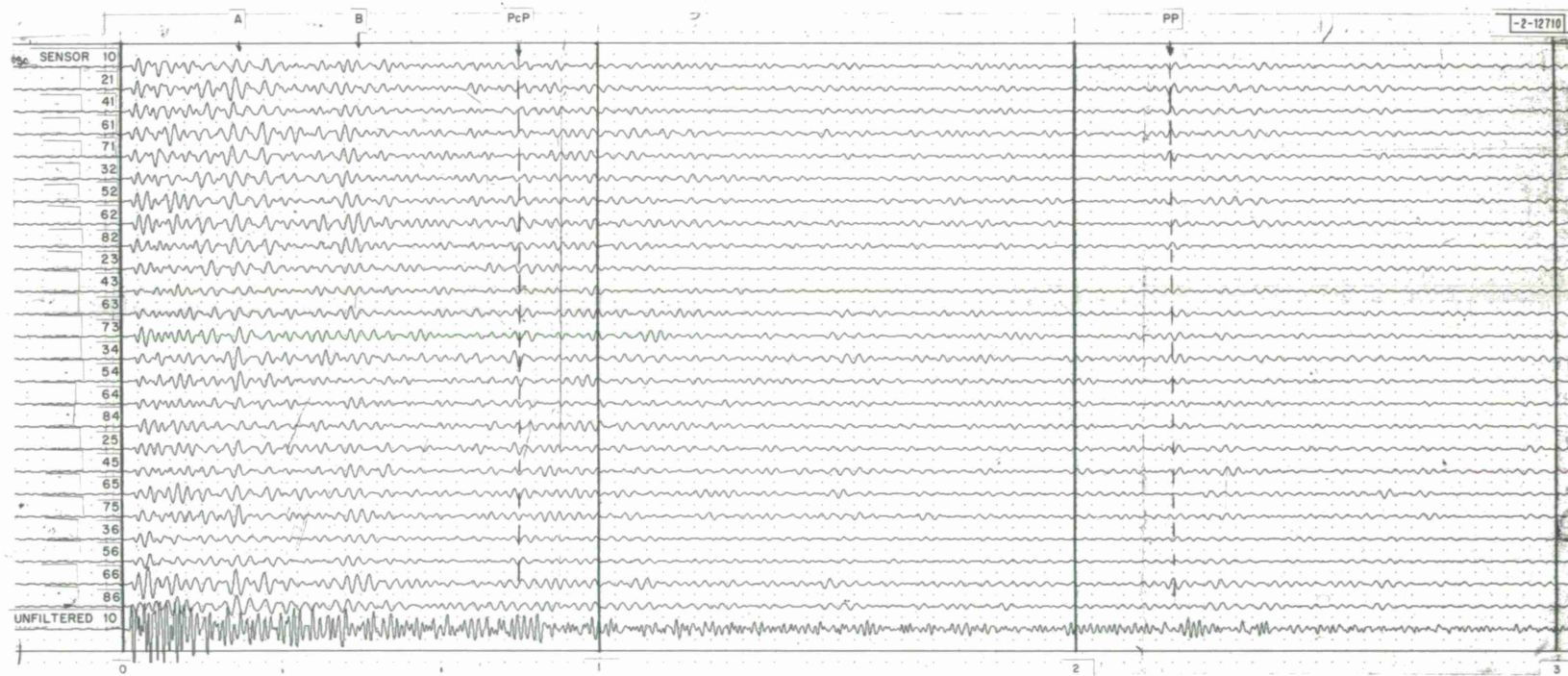
Fig. II-10.   E3 subarray traces of Novaya Zemlya explosion, 14 October 1969, bandpass filtered from 0.5 to 0.9 Hz.
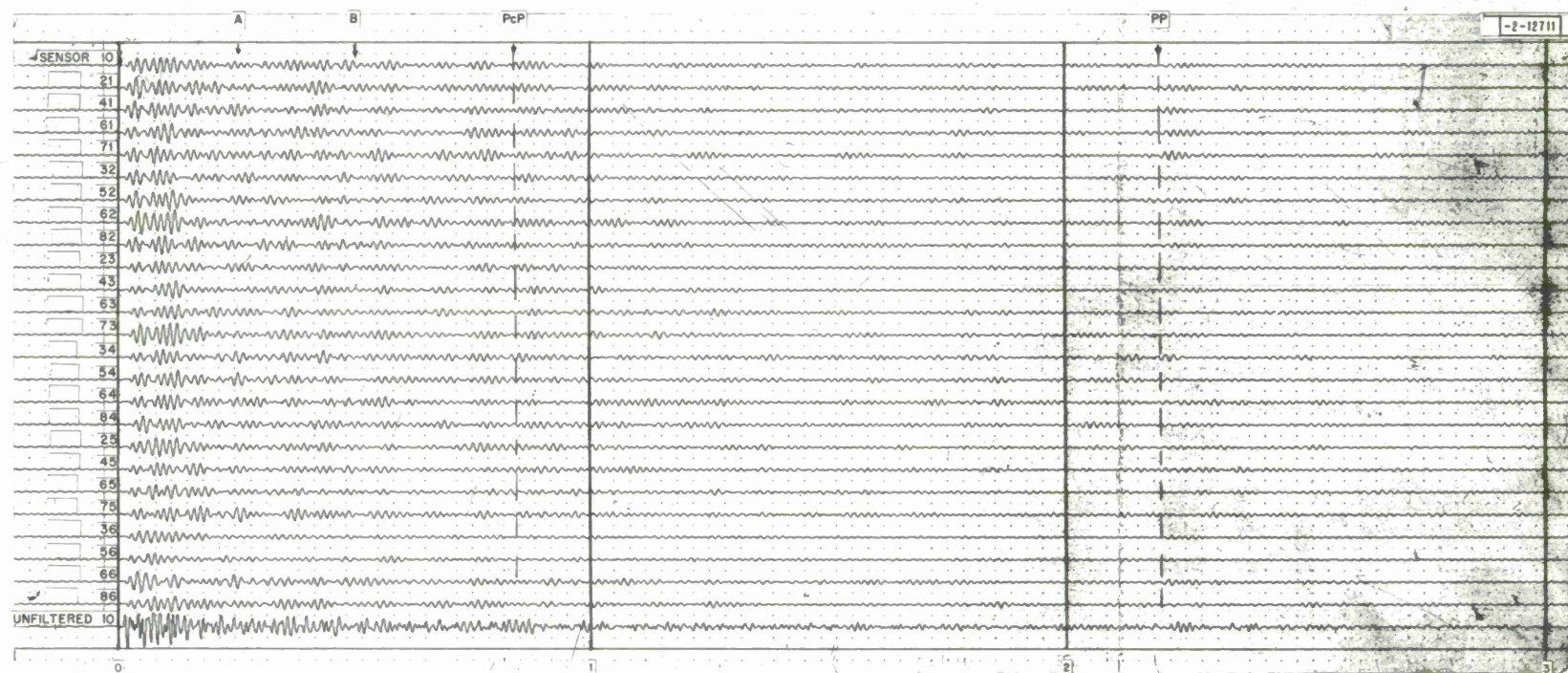
Fig. II-11.   E3 subarray traces of Novaya Zemlya explosion, 14 October 1969, bandpass filtered from 0.8 to 1.2 Hz.
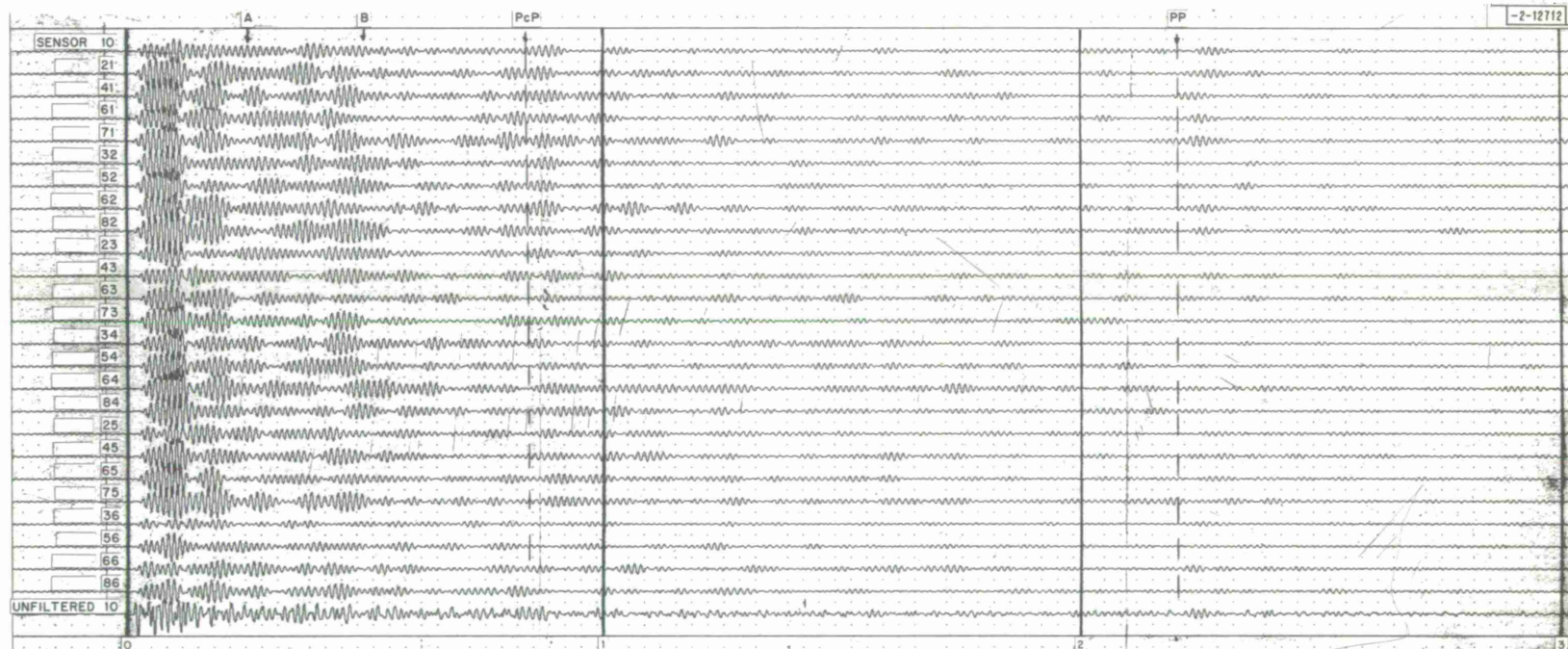
Fig. II-12. E3 subarray traces of Novaya Zemlya explosion, 14 October 1969, bandpass filtered from 1.1 to 1.5 Hz.
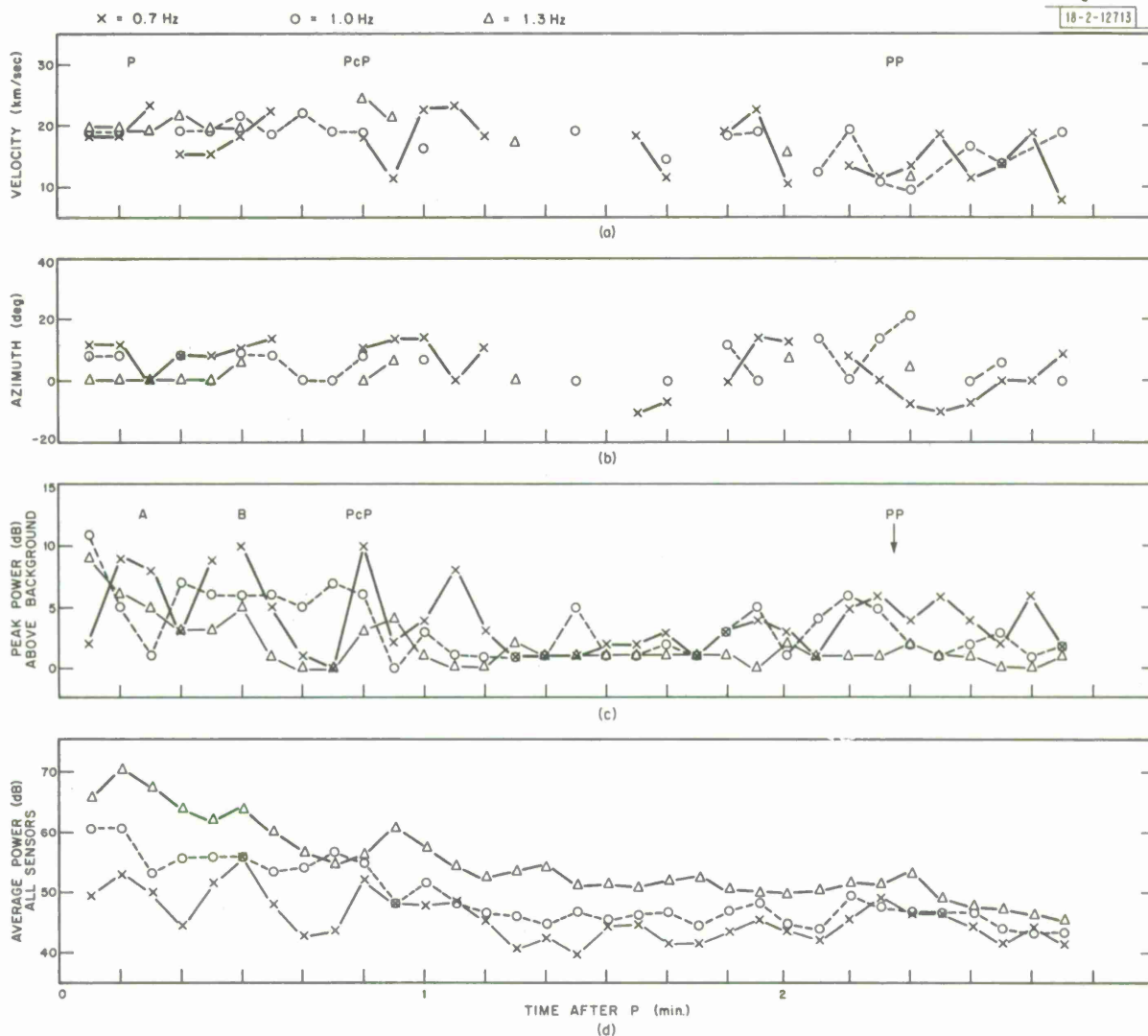
Fig. II-13. High-resolution analysis of E3 subarray data. Each symbol is result of analyzing 10 sec of data. Successive windows overlap by 5 sec. (a) Shows phase velocity of wavenumber peak; (b) shows azimuth of wavenumber peak; (c) displays peak power above background on 25 sensors; and (d) displays average power of all sensors. All calculations done at frequencies of 0.7, 1.0, and 1.3 Hz.

42
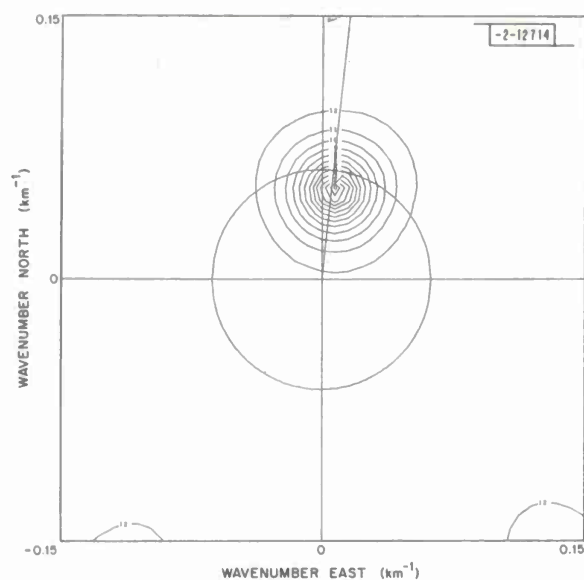
Fig. II-14.   Wavenumber plot of P wave
at 1.0 Hz.   Contour interval is 1 dB.
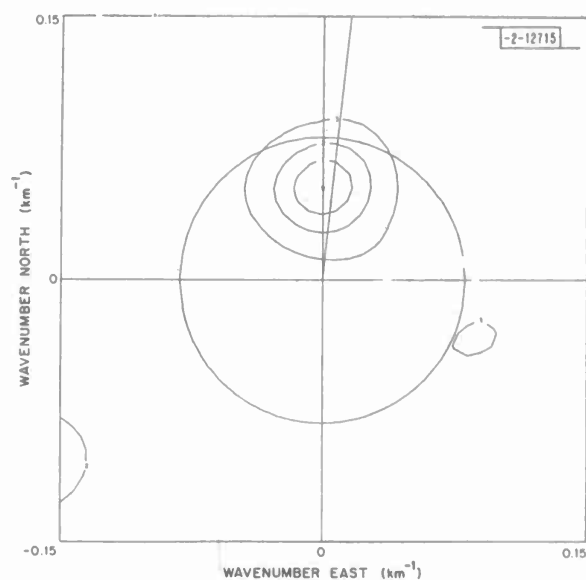
Fig. II-15.   Wavenumber plot of PcP wave
at 1.3 Hz.   Contour interval is 1 dB.

Fig. II-16.   Wavenumber plot of PP wave
at 0.7 Hz.   Contour interval is 1 dB.

43

N 74°

N 73°

E 53°   E 57°

NOVAYA

ZEMLYA

EVENTS		m_b
1	4 OCT 1969	6.1
2	28 AUG 1972	6.3
3	14 OCT 1970	6.7
4	12 SEP 1973	6.8
5	27 SEP 1973	6.0
6	27 OCT 1973	6.9
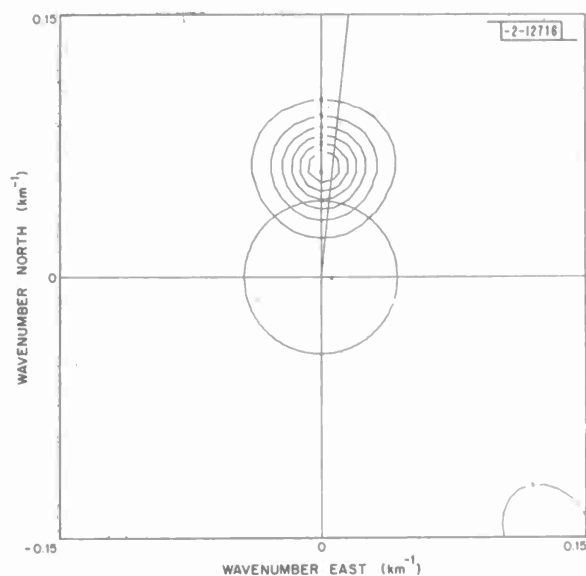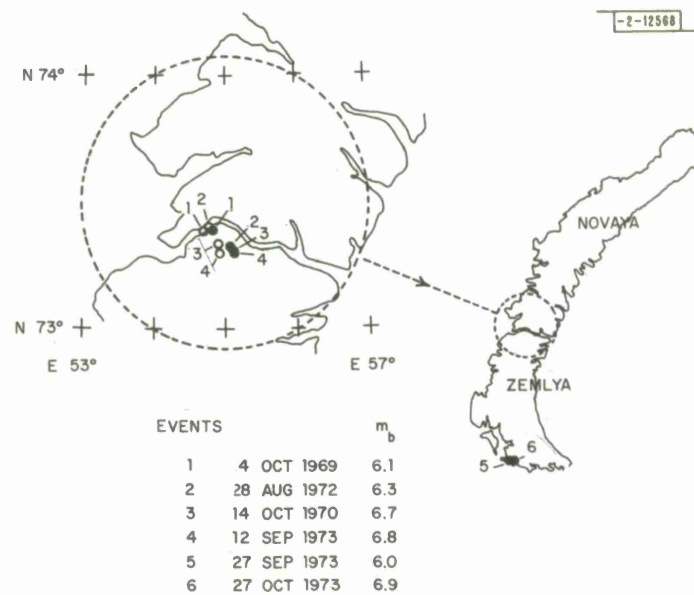
Fig. II-17.   Locations (open circles) and relocations (solid circles) of five Novaya Zemlya events.[10]

EVENT 1, 14 OCT 1969   -2-12717

VERTICAL COMPONENT

VERTICAL COMPONENT FILTERED

1.8 SEC
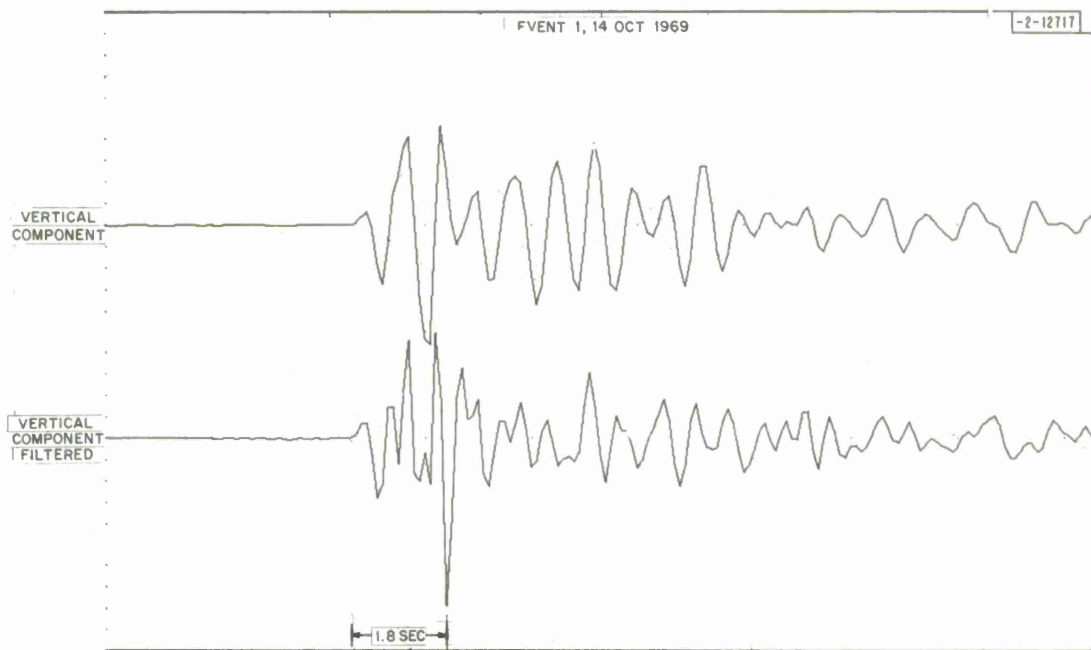
Fig. II-18.   Original vertical component and adaptively deconvolved output from Event 1.

EVENT 2, 14 OCT 1970

-2-12718

VERTICAL COMPONENT S

EAST COMPONENT

NORTH COMPONENT

VERTICAL COMPONENT FILTERED

EAST COMPONENT FILTERED

NORTH COMPONENT FILTERED

|← 10 SEC →|
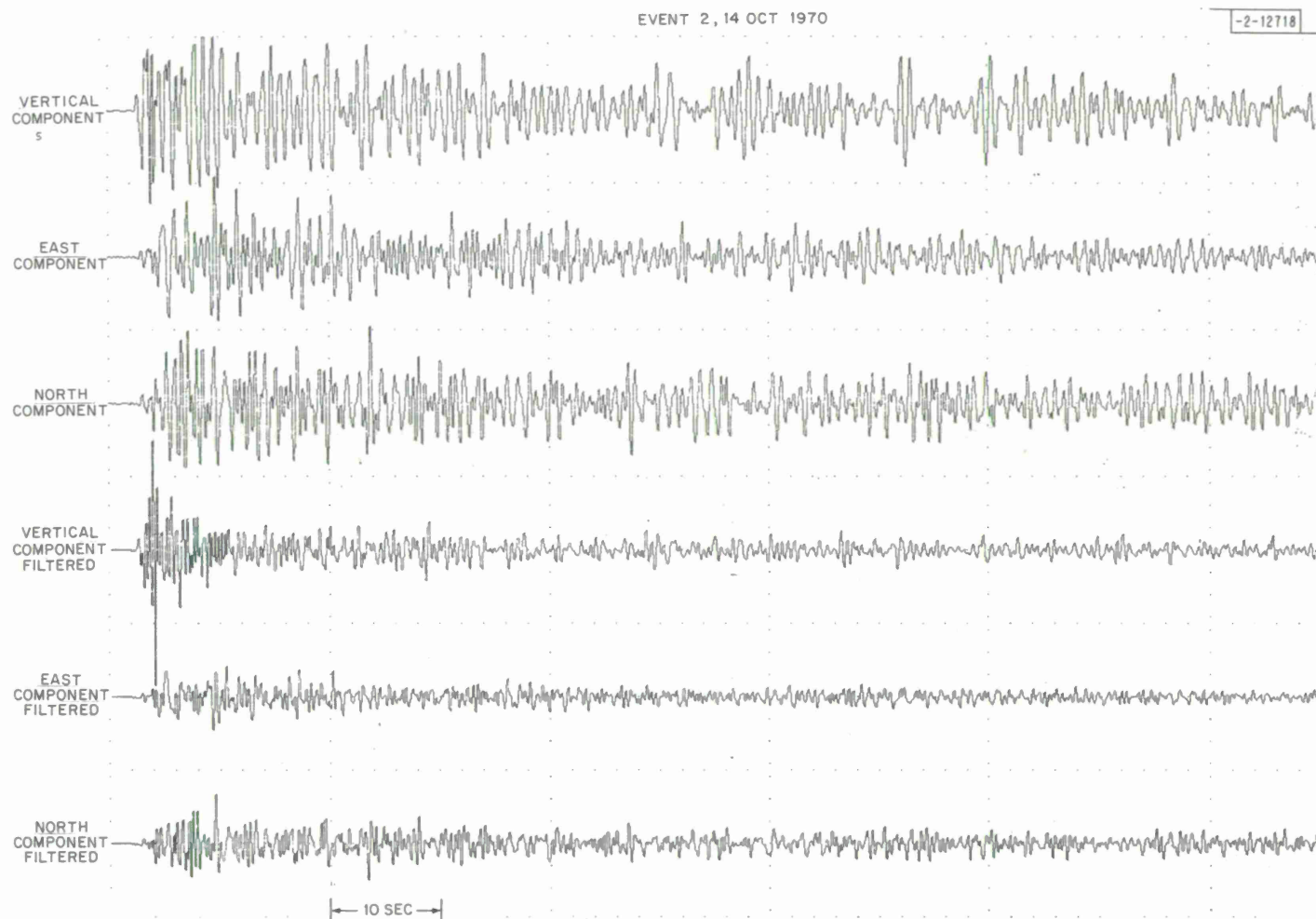
Fig. II-19.   Original data and adaptively deconvolved output from Event 2.
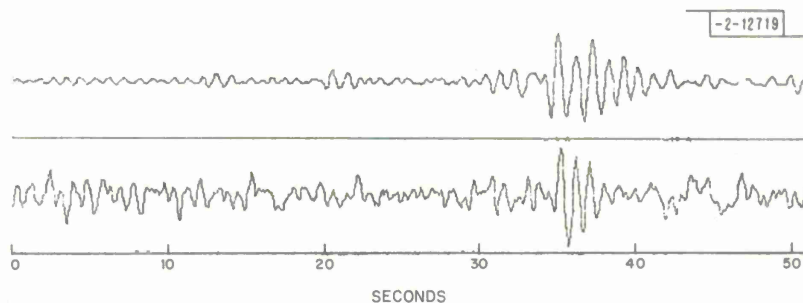
Fig. II-20. Array beam steered for PKPPKP at 2.4 sec/deg (top trace) arriving 2.5 min. after array beam steered for PKP$_{600}$PKP at 2.1 sec/deg (bottom trace). (Gains and signals are adjusted for visual comparison.)
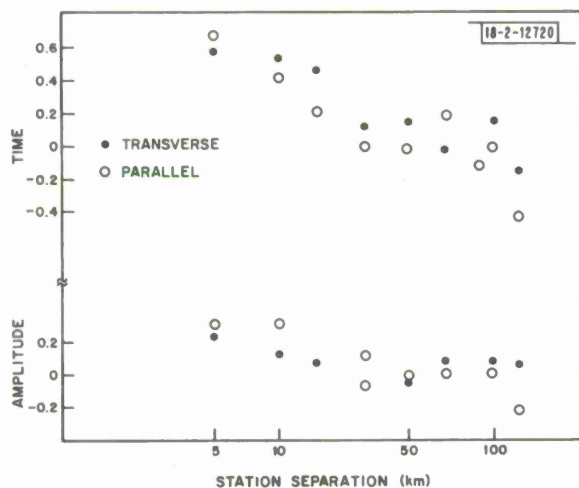
Fig. II-21. Spatial correlation functions derived for LASA from set of Japan earthquakes.
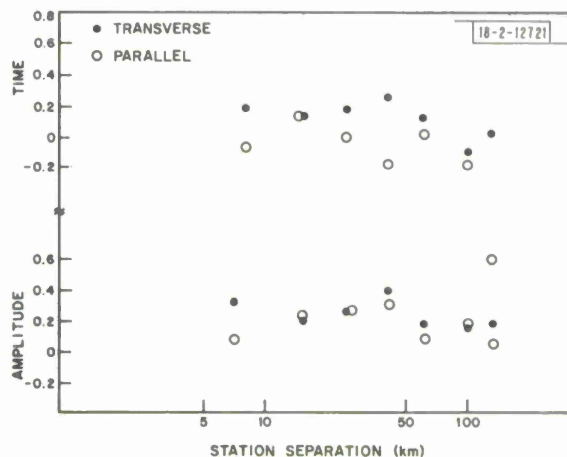
Fig. II-22. Spatial correlation functions derived for LASA from set of Kamchatka earthquakes. In both cases, parallel and transverse refer to station separations projected onto axes, respectively, parallel and perpendicular to ray path.
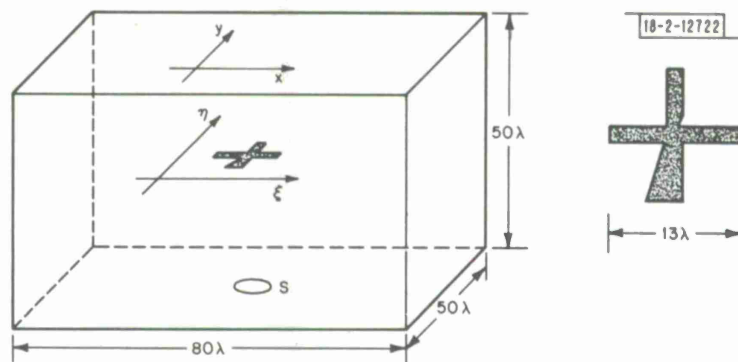
Fig. II-23. Diagram of epoxy model used in ultrasonic holography experiment. ξ-η plane lies 30λ above source, s, and 20λ below x-y plane. Data were recorded at x-y plane every 1/3λ to give matrix of 61 $\times$ 61 data points from which wavefront immediately above ξ-η plane was reconstructed. Source is 12λ diameter.
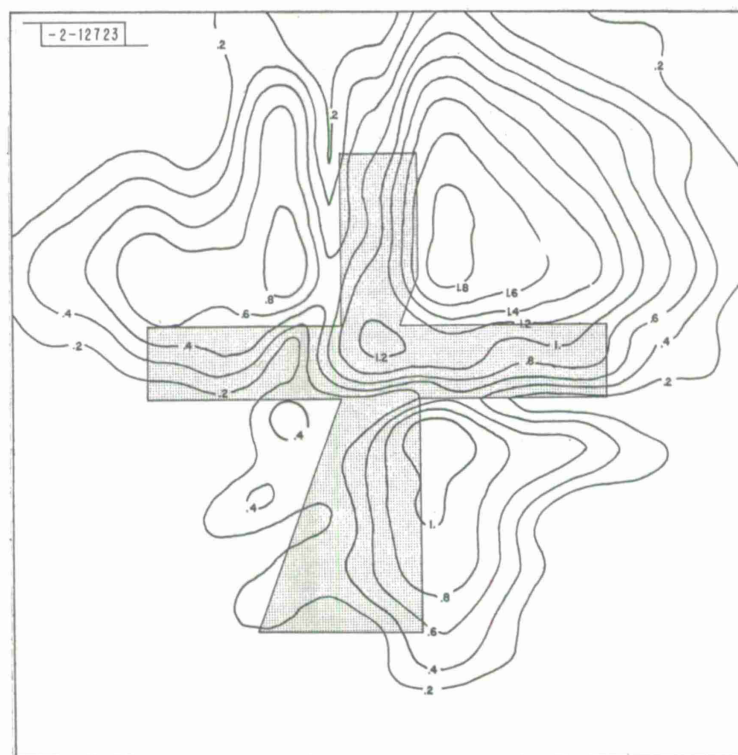
Fig. II-24. Contour map of amplitudes of reconstructed wavefront just above ξ-η plane normalized to arbitrary maximum of 2.0. Shaded area corresponds to position of cross-shaped inhomogeneity. Salient features of cross are clearly depicted by reconstructed wavefront.

47
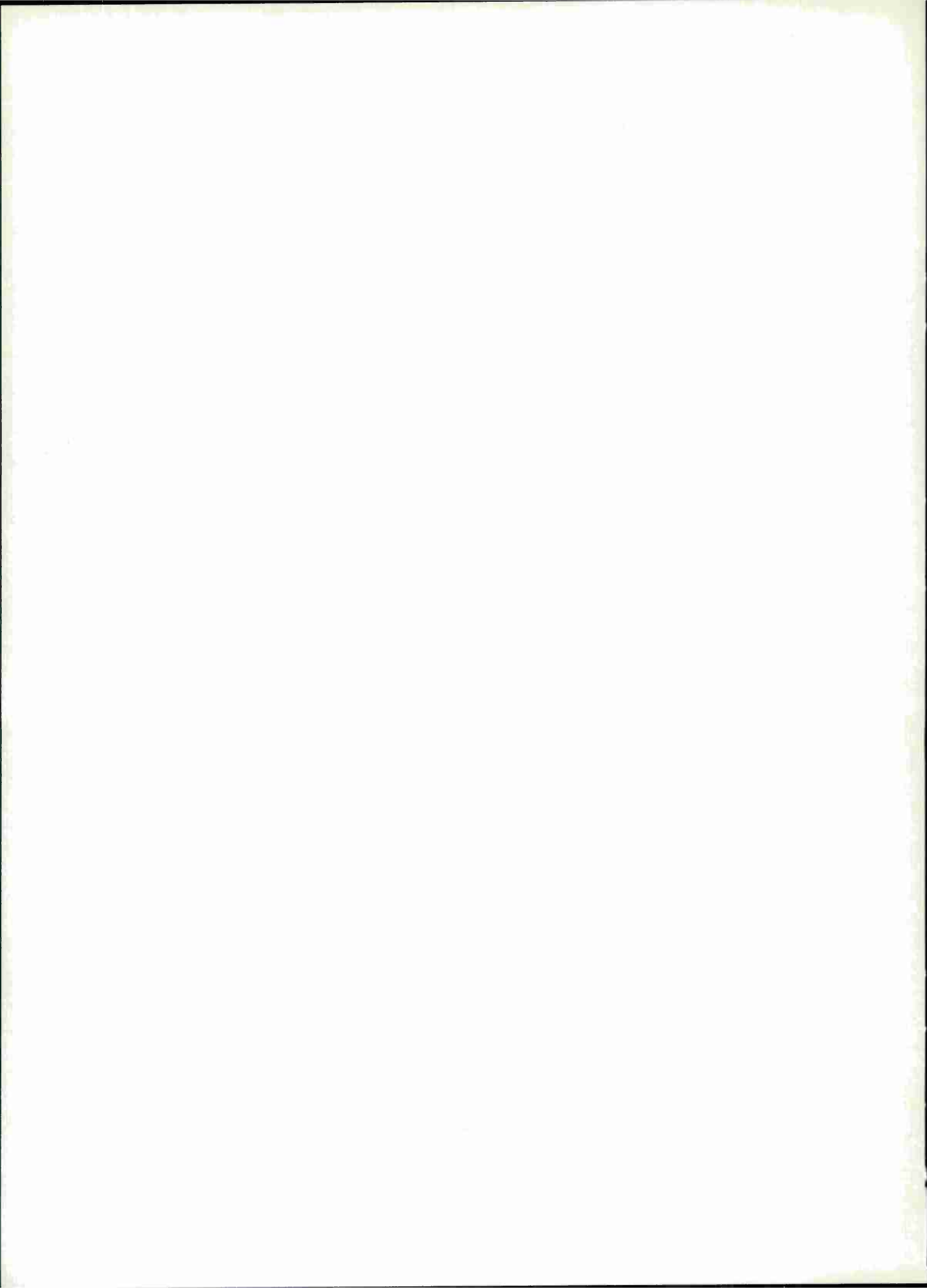
III. MISCELLANEOUS STUDIES

A. STUDIES ON THE MAXIMUM ENTROPY SPECTRAL TECHNIQUE

An important characterization of many physical processes is the power spectrum. Most standard techniques used to estimate this function weight the data in such a way that the data or their autocorrelation are zeroed beyond some lag. When the physics of the process dictates stationarity, such techniques can compromise absolute resolution and produce spectral overlap of adjacent components. Maximum Entropy Spectral Analysis, on the other hand, estimates the spectrum without assuming zero data outside the observed region. This technique, using Burgs' innovation for calculating a consistent prediction error wavelet directly from observed data, has proven very successful in estimating spectra in several seismologically important areas.[1,2]

There are, though, several ill-defined problems in applying the technique to data with significant amounts of noise. Most important is use of the proper filter length. The problem is currently being studied using the correspondence between the Maximum Entropy Method and autoregressive techniques noted by Ulrych and Bishop.[3] Akaike[4] has proposed two methods for determining the order of an autoregressive process. Essentially, the error in predicting the data as a function of filter length is weighted such that less-than-random decreases in the error produce an increase in the weighted error. The estimate of the order then lies at the minimum of the functions. Figure III-1 shows a representative error curve and weighted error curves used in the Maximum Entropy Cepstral Technique shown elsewhere in this report. Here, a triple check of the technique is available since the real, imaginary, and complex log spectra should all have the same order. Figure III-1, showing the results for just the imaginary log spectrum, indicates an order of 23. The real and complex log spectra had the same values. Computed spectra using this filter length gave reasonable results. Unfortunately, data with larger amounts of noise do not give consistent results, and research into this problem is continuing.

<div style="text-align: right;">T. E. Landers</div>

B. THE VARIATION OF MAXIMUM ENTROPY CEPSTRAL pP TIMES OVER A NETWORK OF STATIONS

In anticipation of SRO data, the raw traces from the short-period center instruments of NORSAR for an NTS explosion and a presumed explosion in Eastern Kazakh (EK) have been analyzed by the Maximum Entropy Cepstral[1] method to determine the variation of pP delay times observed over a network of stations. Since waveforms rather than absolute arrival times or amplitudes comprise the data set, use of the individual stations as a network is justified despite all stations being approximately equidistant from the events. Short-period waveform degradation due to near-receiver scattering is severe across NORSAR, and the ability of any individual waveform technique to give consistent results will be adequately tested. Since each path or near-receiver scatterer has approximately the same effect on P and pP, the basic echo delay time should be well determined even though signal shapes vary significantly. Unfortunately, dispersed waveforms have poorer signal-to-noise (S/N) ratios and so less-well-determined cepstra.

The source parameters for the events used in this study were obtained from the PDE and NORSAR Bulletins, and are listed in Table III-1. Data from each center site of the C-ring subarrays and the OA subarray were used. Approximately 15 sec of each of the 15 signals for each

| TABLE III-1 |
| SOURCE PARAMETERS OF THE EVENTS USED IN THE STUDY |

Event	Date (1974)	Time	Latitude	Longitude	Depth	m_b	Δ (deg)	Azimuth (deg)
NTS	20 Aug	15:00:00	37°N	116°W	OG	5.8	73	318
EK	30 Jan	04:57:02	50°N	78°E	OG	5.4	38	75

event was analyzed.   An example of the waveforms is given in Fig. III-2.   Whereas the longer-period NTS event signals remain relatively constant, the shorter-period EK event records at the same two sites show the strong dispersion of signal energy that is often observed.   The result is that while the S/N ratio at OC9 is approximately 10/1, at OC13 it is only 2/1.   Similar, though not so severe, variations also occur for event NTS.

In the manner described in the previous SATS,[1] the Maximum Entropy Cepstrum was computed for each waveform.   For each event, the log-spectrum band and t* were held constant in the analysis of each waveform.   In addition, Akaike's order criterion[4] was computed as an aid in determining the filter length.   Cepstral peaks were read to the nearest digitizing interval, 0.05 sec.   The results are given in Table III-2, and are shown in histogram form in Fig. III-3.

| TABLE III-2 |
| pP TIMES OBSERVED AT THE NORSAR SUBARRAYS |

Event	A1	C1	C2	C3	C4	C5	C6	C7	C8	C9	C10	C11	C12	C13	C14
NTS	0.80	0.70	0.80	0.70	0.80	0.85	0.80	0.75	0.90	0.90	0.85	0.80	0.75	0.75	0.80
EK	0.45	0.70	0.65	0.60	0.55	0.75	0.60	0.55	0.65	0.55	0.50	0.70	0.60	0.55	0.65

The mean and standard deviation of event EK is 0.60 ± 0.08 sec, and for event NTS it is 0.80 ± 0.06 sec.   The consistency of these results, despite the complicating receiver effects and large S/N ratios, are very encouraging.

T. E. Landers

C.   EARTHQUAKE SOURCE MECHANISM DISCRIMINATION

Work continues on the study of discrimination between earthquake source mechanism types. As reported in the last SATS,[1] the mid-Atlantic region is studied because the earthquakes are predominantly of two types (strike-slip and normal), both occurring at similar, shallow depths. Events of this source region are studied to obtain a better understanding of the typical spread observed in explosion-earthquake discriminants, such as M_s vs m_b.

The separation observed in M_s vs m_b for the two mechanism types was attributed to the combination of the effects of source geometry and a local zone of attenuation associated with the spreading ridge.   Dip-slip geometry causes m_b to be higher, while an attenuating zone under

the event reduces m_b. However, the effect of scattering on m_b must also be considered. If a significant amount of the short-period energy radiated from an event undergoes scattering, the lobes of the radiation pattern will effectively be smoothed out. As a result, the m_b for dip-slip events will not be increased as greatly as anticipated. This effect of scattering is being studied to re-examine how much change in M_s vs m_b can actually be attributed simply to the effect of the radiation patterns for particular source geometries.

Although signal complexity is also a useful parameter in the explosion discrimination problem, it has not been found useful in separating these two source mechanism types. This is surprising in view of the observed source complexity of shallow strike-slip events (noted by Filson,[5] for example). Work continues on the modification of the traditional complexity measure to obtain a parameter which does reflect this observable mechanism-dependent signal character.

A. F. Shakal

D. PARAMETRIC TRAVEL-TIME TABLES FOR TELESEISMIC PHASES

An important motivation for construction of a Parametric Earth Model (PEM)[6] has been that its functionals such as travel times are, for a particular branch, smooth functions of the epicentral distance. The density and velocities in model PEM are described by piecewise continuous functions of radius; polynomials up to the third order. Therefore, the travel times for this model might also be represented in a similar form; such representation has been shown to be appropriate in smoothing the observed P and S travel times.[7,8] Model PEM is a good fit to an extensive set of free oscillation data[9] as well as to several subsets of the body wave travel times: P, S, SKS, SKKS, and PKIKP. It may be expected, therefore, that the travel times computed for this model would be more representative of the real earth than the Jeffreys-Bullen tables[10] computed nearly four decades ago. The advantages of an analytical representation of the travel times are the following: (1) the travel times for a particular branch are defined uniquely, there is no need for interpolation which is always subject to a number of assumptions; (2) the functions can be analytically differentiated to obtain the slowness parameter and amplitudes; (3) computer storage requirements are significantly reduced; and (4) certain other parameters such as the incidence angles or bottoming depths can also be computed using analytical formulas.

Coefficients of the polynomial representation of the teleseismic P travel-time branch (rays bottoming below 650-km discontinuity) are shown in Table III-3; all computations are performed for the continental model PEM-C.

The formula for evaluation of the travel time is

$$t(\Delta) = \sum_{n=0}^{N} a_n x^n \tag{III-1}$$

where $x = (\Delta - B)/A$.

The constants A and B are chosen such that x assumes values between -1 and 1, approximately. This means that all the coefficients a_n need to be specified with the same precision.

The values of the polynomial coefficients are obtained by the least-squares fit of $p(\Delta)$ computed for an appropriately selected set of ray parameters; this assures that $p(\Delta)$ obtained by

TABLE III-3										
PARAMETRIC REPRESENTATION OF THE P TRAVEL TIMES FOR RAYS BOTTOMING IN THE LOWER MANTLE[†]										
Depth (km)	Δ_{min}	Δ_{max}	a_0	a_1	a_2	a_3	a_4	a_5	a_6	a_7
0	17.2	94.7	609.00	274.56	−60.24	2.55	3.75	−5.72	1.11	1.64
20	17.1	94.6	605.76	274.36	−60.18	2.56	3.67	−5.69	1.13	1.62
35	17.0	94.6	603.65	274.18	−60.12	2.57	3.62	−5.65	1.13	1.61
70	16.8	94.5	599.88	273.63	−59.92	2.58	3.45	−5.54	1.17	1.57
120	16.3	94.3	594.48	272.84	−59.63	2.61	3.23	−5.35	1.22	1.52
170	15.9	94.2	588.93	272.07	−59.36	2.62	3.01	−5.17	1.27	1.46
220	15.5	94.0	583.39	271.29	−59.08	2.63	2.79	−5.00	1.30	1.40
270	15.0	93.8	578.56	270.39	−58.74	2.60	2.57	−4.77	1.33	1.33
320	14.5	93.7	573.84	269.46	−58.37	2.57	2.36	−4.53	1.35	1.27
370	13.9	93.5	569.25	268.51	−58.00	2.50	2.15	−4.27	1.36	1.19
420	13.3	93.3	564.75	267.51	−57.61	2.42	1.96	−4.02	1.36	1.11
470	12.5	93.0	560.68	266.42	−57.16	2.31	1.81	−3.70	1.33	1.01
520	11.7	92.8	556.66	265.31	−56.70	2.16	1.67	−3.38	1.28	0.92
570	10.8	92.6	552.73	264.17	−56.24	2.00	1.57	−3.07	1.20	0.81
620	9.8	92.3	548.87	262.99	−55.76	1.83	1.51	−2.77	1.11	0.72
670	8.7	92.1	545.09	261.79	−55.27	1.64	1.49	−2.48	1.01	0.63
720	14.4	91.8	541.94	260.38	−54.70	1.12	1.97	−1.74	0.58	0.11
770	16.4	91.5	538.86	258.92	−54.01	0.69	2.09	−1.30	0.47	−0.20

[†] The constants A and B in $x = (\Delta - B)/A$ are 40° and 60°, respectively. For foci shallower than 670 km, the travel times for distances near Δ_{min} will correspond to secondary arrivals.

differentiation of Eq. (III-1) will be accurate:

$$p(\Delta) = A^{-1} \sum_{n=1}^{N} n a_n x^{n-1} \tag{III-2}$$

coefficient a_0 is then obtained to give the best least-squares to the travel times.

For the set of parameters shown in Table III-3, the rms difference between $p(\Delta)$ obtained using Eq. (III-2) and computed exactly is 0.002 sec/deg and the maximum difference is -0.008 sec/deg at 94.7°; the rms error for the travel times is 0.03 sec, and maximum difference 0.07 sec at 93°. Clearly, the fit is satisfactory.

Travel times have also been calculated for a number of other phases. For instance, polynomial coefficients for the surface focus are listed in Table III-4 for 52 phases; the full set is much more extensive, as the SP and PS travel times are different for a finite depth focus; also, multiple surface reflections, trivial for a surface focus, are not included. Note that only the phases with a ray, or both rays in the case of converted phases, bottoming in the lower mantle are listed. The discontinuity in the upper mantle of model PEM gives rise to multiple branches for rays bottoming in this region; the best representation for the upper-mantle travel times is still under consideration.

In addition to the travel times, ellipticity corrections have also been computed using the approach of Dziewonski and Gilbert[1,11] in which the ellipticity correction is represented by:

$$\delta t = \sum_{m=0}^{2} P_{2,m}(\Theta_0) \cdot \cos m\xi \cdot \tau_m(\Delta) \quad . \tag{III-3}$$

The analytical representation of these corrections in terms of Eq. (III-1) is possible, although it is more complex since the functions $\tau_m(\Delta)$, unlike the travel times, are generally not monotonic. For some phases (e.g., SKKKS), $\tau_m(\Delta)$ have four local extrema; accurate representation with a low degree polynomial is not possible in this case.

This difficulty may be circumvented in the following way. The most significant part of the ellipticity correction arises due to a change in the radius of the free surface; this is particularly true for the core phases. Thus, instead of the form

$$\tau_m(\Delta) = \sum_{n=0}^{N} b_{nm} x^n \tag{III-4}$$

we may seek the representation:

$$\tau_m(\Delta) = C_m [\delta_{m0} + P_{2,m}(\Delta)] + \sum_{n=0}^{N} c_{nm} x^n \tag{III-5}$$

[see Eqs. (23) to (25) in Ref. 11]; Eq. (III-5) can easily be generalized for the multiple surface reflections. In Table III-5, we compare results obtained for the core P phases using Eqs. (III-4) and (III-5). For PKIKP and PKP_1, nearly the entire variation of $\tau_m(\Delta)$ is described by the first term in Eq. (III-5). This is in good agreement with the J-B tables,[10] where a constant value of $f(\Delta) = 0.09$ sec is suggested for all the PKP branches. This value of $f(\Delta)$ is equivalent

TABLE III-4

PARAMETRIC REPRESENTATION OF TRAVEL TIMES FOR 52 PHASES — SURFACE FOCUS

Phase[†]	A	B	Δ_{min}	Δ_{max}	a_0	a_1	a_2	a_3	a_4	a_5	a_6	a_7
PKP	30	150	114.2	180.0	1187.75	46.86	−14.88	−8.91	0.45	2.42	−0.13	−0.50
PKP_1	5	150	144.7	155.5	1193.01	12.78	−1.27	0.14	0.00	−0.01	−0.05	0.04
PKP_2	15	155	144.7	173.1	1220.04	64.33	2.32	−1.04	0.41	−1.27	1.47	−0.50
PcP	45	45	0.0	94.3	598.27	155.80	47.40	−21.62	2.33	1.73	−0.76	—
PKiKP	55	55	0.0	113.6	1028.34	63.20	27.24	−4.02	−0.68	0.14	—	—
PKKP	80	280	207.4	360.0	1845.61	128.41	−40.56	−26.69	2.00	8.85	−0.54	−2.30
$PKKP_1$	25	260	235.8	288.0	1806.34	71.95	−10.09	0.91	0.08	−0.06	−0.47	0.29
$PKKP_2$	10	240	235.8	251.9	1744.24	43.64	0.82	−0.49	0.12	—	—	—
PKKKP	120	420	300.6	540.0	2519.26	183.76	−65.22	−33.18	6.98	9.02	−2.05	−2.06
$PKKKP_1$	50	370	320.1	420.5	2419.11	146.47	−23.24	2.09	0.24	−0.83	−0.85	0.86
$PKKKP_2$	5	325	320.1	330.6	2268.78	22.10	0.06	−0.04	0.01	—	—	—
PKIIKP	120	240	114.7	360.0	1342.70	166.81	−65.04	−19.52	5.19	1.32	−0.89	—
PcPPKP	25	160	135.2	180.0	1700.93	44.72	−5.38	−8.00	−11.28	−6.00	4.03	3.65
$PcPPKP_1$	45	220	178.4	267.4	1894.87	189.25	12.49	−6.91	−0.08	−0.78	5.00	−2.83
$PKPPKP^{670}$	70	290	226.3	360.0	2206.16	117.59	−30.01	−26.41	−3.89	9.41	1.57	−2.72
$PKPPKP_1^{670}$	10	295	285.0	308.6	2222.24	26.64	−2.56	0.25	−0.01	0.08	−0.13	0.05
$PKPPKP_2^{670}$	30	310	285.0	341.0	2295.99	130.02	3.71	−2.00	−0.41	−0.27	2.22	−1.26

† The superscripts "670" denote the underside reflections from the 670-km discontinuity. The core phases without a subscript refer to rays traveling through the inner core.

TABLE III-4 (Continued)												
Phase	A	B	Δ_{min}	Δ_{max}	a_0	a_1	a_2	a_3	a_4	a_5	a_6	a_7
PP^{670}	80	100	17.4	184.2	952.34	579.18	−111.03	−3.25	10.37	−6.32	−0.19	1.25
S	40	60	15.4	98.9	1106.72	514.43	−91.68	−0.61	5.33	−6.29	0.50	1.32
ScS	50	50	0.0	98.7	1132.75	342.67	95.26	−50.68	8.37	3.84	−2.36	−
SKS	40	140	104.1	180.0	1604.93	64.67	−19.89	−13.54	0.61	4.47	−0.14	−1.17
SKS_1	35	110	70.6	144.3	1515.73	144.25	−43.60	7.64	−4.83	1.95	2.31	−1.90
SKKS	80	280	197.3	360.0	2278.41	120.02	−44.10	−20.15	5.10	4.86	−1.44	−1.05
$SKKS_1$	95	180	81.1	276.9	1974.38	434.04	−138.22	19.22	−0.43	−6.48	4.04	−0.65
SKKKS	125	415	290.5	540.0	2944.12	188.37	−69.35	−31.84	8.46	7.51	−2.46	−1.52
$SKKKS_1$	160	250	91.6	409.4	2431.32	749.21	−246.04	29.14	5.00	−13.62	6.03	−0.35
$ScSSKS_1$	15	140	128.9	156.1	2526.59	52.36	−12.33	1.93	−0.30	1.93	−3.18	1.35
$ScSSKS_2$	2	130	128.9	131.6	2486.11	13.30	0.65	−0.04	0.42	−0.65	−0.20	0.47
PS	15	125	110.1	137.8	1857.58	132.89	−3.33	−0.77	0.17	−	−	−
PPS	25	150	127.3	176.6	2183.70	223.41	−4.48	−1.39	0.17	−	−	−
PSS	20	220	203.0	236.7	3344.55	177.21	−4.73	−1.04	0.36	−	−	−
PcS	30	30	0.0	60.7	777.26	97.76	35.46	−11.64	−1.11	0.73	−	−
PKS	35	155	109.1	180.0	1410.62	43.22	−26.00	−8.05	4.69	1.80	−1.89	−0.88
PKS_1	10	140	130.0	147.6	1389.16	27.49	−3.79	0.46	−0.10	−0.22	−0.05	0.26
PKS_2	5	135	130.0	139.5	1378.95	22.00	0.16	−0.08	0.07	−0.05	−	−
$PScS_1$	5	115	110.3	121.8	1771.62	27.02	−2.19	0.24	0.01	0.10	−0.18	0.07
$PScS_2$	15	125	110.3	137.6	1861.06	124.53	2.23	−1.85	0.14	0.91	0.72	−1.12

TABLE III-4 (Continued)

Phase	A	B	Δ_{min}	Δ_{max}	a_0	a_1	a_2	a_3	a_4	a_5	a_6	a_7
$PSKS_1$	40	160	122.1	200.5	2091.27	240.41	−34.37	2.22	0.61	−1.44	0.75	—
$ScPPKP$	25	155	130.1	180.0	1909.41	44.84	−5.20	−6.21	−5.63	−1.96	1.49	1.07
$ScPPKP_2$†	30	200	172.2	233.8	2053.34	126.82	6.96	−3.49	0.12	−0.79	2.35	−1.14
$ScSPKP$	30	150	125.1	180.0	2117.88	54.00	−7.00	−9.23	−6.82	−0.08	2.20	0.32
$ScSPKP_1$	2	165	163.8	166.4	2151.00	4.97	−0.47	0.15	−0.02	−0.11	−0.28	0.41
$ScSPKP_2$	20	180	163.8	200.2	2211.88	85.38	4.10	−2.21	−0.02	−0.68	2.29	−1.22
$PKKS$	80	280	202.4	360.0	2062.12	124.22	−42.68	−23.38	3.99	6.72	−1.18	−1.58
$PKKS_1$	30	245	214.0	276.5	1987.18	91.56	−13.02	1.02	0.05	−0.22	−0.34	0.28
$PKKS_2$	3	215	214.0	218.3	1881.51	13.23	0.08	−0.07	0.02	—	—	—
$PKPSKS$	70	290	218.3	360.0	2792.64	111.46	−34.65	−22.47	0.99	7.06	−0.26	−1.75
$PKPSKS_1$	20	280	260.0	295.3	2778.32	54.98	−7.58	0.92	−0.21	−0.47	−0.12	0.51
$PKPSKS_2$	10	270	260.0	279.0	2757.90	43.98	0.34	−0.14	0.15	−0.10	—	—
$PKPPKS$	70	290	223.3	360.0	2575.97	115.40	−31.91	−25.07	−1.80	8.57	0.73	−2.30
$PKPPKS_1$	15	290	276.1	301.3	2582.28	40.02	−4.95	0.73	−0.12	−0.48	−0.16	0.54
$PKPPKS_2$	20	295	276.1	312.6	2620.62	87.58	1.43	−0.93	0.03	0.22	0.41	−0.42

† The extent of the branch $ScPPKP_1$ is less than 0.3°.

TABLE III-5

PARAMETERIZATION OF ELLIPTICITY CORRECTION COEFFICIENTS FOR PKP PHASES†

Phase and Δ Range	m	C_m	b_0/c_0	b_1/c_1	b_2/c_2	b_3/c_3	b_4/c_4	b_5/c_5	b_6/c_6
PKIKP 114.2 to 180.0	0	—	-2.10	-1.05	0.25	0.21	0.00	-0.01	-0.01
		-1.35	0.00	—	—	—	—	—	—
	1	—	1.07	-0.58	-0.58	0.09	-0.14	0.01	0.13
		-1.27	0.07	-0.07	—	—	—	—	—
	2	—	-0.32	0.53	-0.12	-0.02	-0.02	-0.07	0.01
		-1.22	0.00	—	—	—	—	—	—
PKP₁ 144.7 to 155.5	0	—	-2.16	-0.20	0.02	-0.01	0.01	—	—
		-1.33	0.00	-0.04	0.01	—	—	—	—
	1	··	0.99	-0.09	-0.02	0.01	-0.01	—	—
		-1.32	0.00	0.02	-0.01	—	—	—	—
	2	—	-0.29	0.07	—	—	—	—	—
		-1.33	0.00	0.00	-0.01	—	—	—	—
PKP₂ 144.7 to 173.1	0	—	-2.06	-0.19	0.05	0.00	0.02	0.03	-0.03
		-1.14	-0.02	0.10	-0.03	0.01	-0.01	0.01	—
	1	—	0.63	-0.39	-0.03	0.01	-0.01	-0.02	0.02
		-1.10	-0.02	-0.04	0.03	-0.01	0.03	-0.02	—
	2	—	-0.35	0.05	-0.03	0.00	-0.01	-0.01	0.01
		-1.37	-0.20	-0.15	0.02	0.00	0.01	—	—

† Obtained using Eq. (III-1) – constants b_{nm}, and Eq. (III-5) – constants C_m and c_{nm}. For this table: A = ($\Delta_{max} - \Delta_{min}$)/2; B = ($\Delta_{max} + \Delta_{min}$)/2.

to $C_m = -1.28$ in Table III-5, with all other coefficients being zero. The maximum errors resulting from this approximation would be of the order of 0.1 sec for PKIKP and PKP_1, but for PKP_2 errors could amount to as much as 0.5 sec.

A. M. Dziewonski

E. TOWARD A MOMENT TENSOR-ENERGY RELATION

The advantages to expressing seismic radiation fields in terms of the moment tensor of the applied source[12] are well known. The six independent quantities in this tensor provide information about the seismic source in the most general form; for example, it can describe a source representing a linear combination of three point source mechanisms: explosive, compensated linear vector dipole, and double couple.[13] Furthermore, the time history of the moment tensor determines the phenomenology of the event.[14] In this report, we show how to solve the forward problem of directly calculating the radiated seismic energy if the moment tensor (i.e., source mechanism) of an event and the earth structure are known. In our approach, we utilize certain fundamental properties of normal modes.

Following Gilbert,[12] we can express the vector displacement of the earth's surface as a sum over its normal modes of oscillation:

$$\vec{u}(\vec{r},t) = \sum_n \vec{s}_n(\vec{r}) \, [M{:}S_n(\vec{r}_s)] \, \frac{1 - \cos \omega_n t}{F_n \omega_n^2} \quad . \tag{III-6}$$

In this expression, $\vec{s}_n$ is the displacement vector for the nth mode, M is the moment tensor of the source, $S_n(\vec{r}_s)$ is the strain tensor of the nth mode evaluated at the source position, ω_n is the angular frequency of the nth mode, and F_n is the normalization factor:

$$F_n = \int \rho(\vec{r}) | \vec{s}_n(\vec{r})|^2 \, dv \quad . \tag{III-7}$$

The kinetic energy density in each mode will then be given by:

$$\mathcal{E}_n(\vec{r}) = \frac{1}{2} \rho(\vec{r}) \left| \vec{s}_n(\vec{r}) \, W_n \, \frac{\sin \omega_n t}{F_n \omega_n} \right|^2 \tag{III-8}$$

where W_n represents the nth weight: S:M. Integrating this over the volume of the earth and evaluating it at its maximum ($\omega_n t = \pi/2$) gives the kinetic energy in each mode:

$$E_n = \frac{1}{2} \frac{|W_n|^2}{F_n \omega_n^2} \tag{III-9}$$

where we have used the normalization relation (III-7) in the numerator. Since the normal modes are independent, the total energy is the sum of the maximum kinetic energies:

$$E = \frac{1}{2} \sum_n \frac{|M{:}S_n(\vec{r}_s)|^2}{F_n \omega_n^2} \quad . \tag{III-10}$$

This relationship can be generalized for an event with an arbitrary time history if M in Eq. (III-10) were to represent the spectrum of the moment rate tensor $M(\omega)$.[9] For the case of

a ramp increase in applied moment of length T, and the total moment M_o:

$$E = \frac{1}{2} \sum_n \frac{|M_o : S_n(\vec{r}_s)|^2}{F_n \omega_n^2} \left(\frac{\sin \frac{\omega_n T}{2}}{\frac{\omega_n T}{2}} \right)^2 . \qquad \text{(III-11)}$$

As can be seen, the effect of changing the source time function from a step function to a ramp function is to reduce the total radiated energy. Thus, events with slow increases in applied moment radiate decreasing amounts of high-frequency energy. Energy associated with the low-frequency modes is relatively unaffected.

To apply either of these expressions to actual events, it is necessary to have a complete catalog of normal mode frequencies and their associated strains. A suitable model which satisfied a wide spectrum of standard earth data is Gilbert's and Dziewonski's[9] 1066A model for density, and compressional and shear velocities. For this model, we have spheroidal modes $_nS_\ell$, with n reaching 62 at $\ell = 1$ and n = 9 at $\ell = 99$. This provides complete coverage down to 100-sec period. We have toroidal modes $_nT_\ell$, with ℓ up to 150 to provide complete coverage down to 60-sec period. This catalog was computed by Buland and Gilbert[15] and was kindly made available to us.

TABLE III-6			
SOURCE PARAMETERS FOR THE ALASKAN AND CHILEAN EARTHQUAKES			
Parameter	Alaska, 1964	Chile, 1960	Reference
Depth (km)	50	25	16, 17
Strike (deg)	246	10	16, 17
Dip (deg)	20	35.5	16, 17
Slip (deg)	270	270	16, 17
Moment (dyn-cm)	7.5×10^{29}	8.6×10^{29}	16, 17
M_s	8.3	8.3	USGS; USGS
Energy (erg)	1.5×10^{25}	1.8×10^{24}	16; Gutenberg-Richter relation

As a test of the method, we consider the 1964 Alaskan and 1960 Chilean earthquakes. Both were large enough to excite the earth's free oscillations, observations of which were used to determine model 1066A.[9] The source mechanisms of these were found, for example, by Kanamori[16] in the former case, and by Plafker and Savage[17] in the latter. The pertinent data are listed in Table III-6. Double couple moment tensors computed from these results were then used along with the catalog of normal modes to calculate the energies given in Table III-7.

The results for both earthquakes show that the step-function source releases more energy than the estimates shown in Table III-6; actually, it can be shown that if all possible modes are considered, the energy is infinite for the step function. Using ramp times of 170 and 180 sec

TABLE III-7				
CALCULATED ENERGIES IN THE EARTH'S FREE OSCILLATIONS				

	Toroidal (erg)	Spheroidal (erg)	Total (erg)	M_s from Gutenberg-Richter Relation
Alaska				
D = 45.2 km, step function	2.55×10^{25}	1.97×10^{25}	4.52×10^{25}	9.2
D = 79.4 km, step function	3.60×10^{25}	3.02×10^{25}	6.62×10^{25}	9.3
D = 79.4 km, 170-sec ramp function	3.39×10^{23}	4.09×10^{24}	4.4×10^{24}	8.5
Chile				
D = 45.2 km, 180-sec ramp function	3.35×10^{23}	4.63×10^{23}	7.98×10^{23}	8.1
D = 45.2 km, step function	2.64×10^{25}	3.45×10^{25}	6.09×10^{25}	9.3

for the Alaskan and Chilean earthquakes, respectively, brings both energy values down to about a third of the estimated values. These ramp times were suggested by analysis of other large earthquakes[14] and seem reasonable when compared with estimates of the fault length divided by the rupture velocity.[16,18] Furthermore, the results for the Alaskan earthquake with the source at two depths show a slight increase in radiated energy with increasing depth.

Two conclusions based on these results are that: (1) although the seismic moments of both the Alaskan and Chilean earthquakes are comparable, the difference in source depth and mechanism leads to five times more energy being radiated in the Alaskan event; and (2) the bandwidth of this experiment (100-sec period for the spheroidal modes and 60-sec period for the toroidal modes) is able to account for roughly a third of the estimated strain energy release with a 170- to 180-sec ramp-function time history. It also can be generally observed that a very large part of the total energy is contained in the long period part of the spectrum, and that the spectral energy density depends significantly on the source time function.

Further work along this line should consist of: (1) extending the spheroidal part of the free oscillation catalog to shorter periods, (2) analyzing additional events to determine if any definite patterns emerge between observed source characteristics and calculated energies, and (3) studying the energy distribution as a function of frequency.

<div style="text-align: right">

D. W. McCowan
A. M. Dziewonski

</div>

F.   APPLICATION OF NORMAL-MODE THEORY TO CALCULATION OF CHANGES IN THE EARTH'S MOMENT OF INERTIA DUE TO EARTHQUAKES

The problem of evaluating a change in the earth's moment of inertia due to redistribution of density $\delta\rho(\underset{\sim}{r})$ following an earthquake consists of computation of the integral:

$$\Delta\underset{\sim}{C} = \int_V \left[(\underset{\sim}{r} \cdot \underset{\sim}{r}) \, \underset{\sim}{I} - (\underset{\sim}{r} \, \underset{\sim}{r}) \right] \delta\rho(\underset{\sim}{r}) \, dV \quad . \tag{III-12}$$

In all published solutions, $\delta\rho(\underset{\sim}{r})$ has been obtained by solving the static deformation problem; here we use the result of Gilbert,[12] who has shown that the static displacement field can be obtained by superposition of normal modes. In practical terms, we circumvent the difficulty that occurs in solving the static displacement problem with the "normal" boundary conditions — for example, continuity of the radial displacement across the liquid-solid interface at the core mantle boundary. Chinnery[19] makes a convincing case for application of a different set of the boundary conditions. However, in the case of a homogeneous, adiabatically compressed fluid core either set of conditions leads to the same system of equations. Since the seismic evidence indicates that the density distribution in the outer core follows the Adams-Williamson equation very closely, we believe that, in practice, either set of equations should lead to similar results. In particular, in our numerical calculations we use an earth model[6] that satisfies the Adams-Williamson equation nearly exactly.

The advantage of using the normal mode theory is that it has been empirically tested; all the modes that significantly contribute to the change in the moment of inertia have been observed; their excitation and eigenfrequencies can be explained by the realistic models of the earth's structure and seismic source. The numerical results presented by various authors using the static displacement approach have been marred by disagreements of an order of magnitude; comparisons with observations are questionable, as the estimates of changes in the pole positions following (or preceding) earthquakes are uncertain.

For an elastic deformation:

$$\delta\rho(\underset{\sim}{r}) = -\rho_0(r) \underset{\sim}{\nabla} \cdot \underset{\sim}{u}(\underset{\sim}{r}) - \hat{\underset{\sim}{r}} \cdot \underset{\sim}{u}(\underset{\sim}{r}) \, \partial_r \rho_0(r) \quad . \tag{III-13}$$

The static displacement vector $u(r, t = \infty)$ may be represented in terms of superposition of normal modes[12] (the epicentral coordinate system is adopted):

$$\underset{\sim}{u}(\underset{\sim}{r}) = \sum_{i=1}^{6} \left\{ \sum_{\ell=0}^{\infty} \sum_{n=0}^{\infty} \sum_{m=0}^{\min(2,\ell)} {}_n\underset{\sim}{S}_\ell^m(\underset{\sim}{r}) \cdot [{}_n\overline{\underset{\sim}{\mathcal{E}}}_\ell^m(r_s)]_i \right\} M_i \tag{III-14}$$

where M_i are the elements of the moment tensor (the formalism and symbols follow Gilbert and Dziewonski,[9] Sec. 2; note that M_i is a vector representing a second rank symmetric tensor; similarly, the inertia tensor will be represented as a vector C_i).

After substitution of Eq. (III-14) into (III-13) and then into (III-12), transformed into the spherical coordinate system, it is clear that each element of inertia tensor must be a linear combination of the elements of the moment tensor

$$\Delta C_i = \sum_{j=1}^{6} D_{ij} M_j \tag{III-15}$$

where $\underset{\sim}{D}$ is a matrix representing a fourth rank tensor:

$$
\begin{vmatrix}
R_1 - 2S_1 & R_2 - 2S_2 & R_2 - 2S_2 & 0 & 0 & 0 \\
R_1 + S_1 & R_2 + S_2 - S_3 & R_2 + S_2 + S_3 & 0 & 0 & 0 \\
R_1 + S_1 & R_2 + S_2 + S_3 & R_2 + S_2 - S_3 & 0 & 0 & 0 \\
0 & 0 & 0 & S_4 & 0 & 0 \\
0 & 0 & 0 & 0 & S_4 & 0 \\
0 & 0 & 0 & 0 & 0 & -2S_3
\end{vmatrix}
\tag{III-16}
$$

and

$$R_1 = \frac{2}{3} \sum_{n=0}^{\infty} {}_nI_0 \cdot {}_n(\mathcal{E}_1^0)_0 \quad ; \quad R_2 = \frac{2}{3} \sum_{n=0}^{\infty} {}_nI_0 \cdot {}_n(\mathcal{E}_2^0)_0$$

$$S_1 = \frac{1}{3\sqrt{5}} \sum_{n=0}^{\infty} {}_nI_2 \cdot {}_n(\mathcal{E}_1^0)_2 \quad ; \quad S_2 = \frac{1}{3\sqrt{5}} \sum_{n=0}^{\infty} {}_nI_2 \cdot {}_n(\mathcal{E}_2^0)_2$$

$$S_3 = \sqrt{\frac{2}{15}} \sum_{n=0}^{\infty} {}_nI_2 \cdot {}_n(\mathcal{E}_2^2)_2 \quad ; \quad S_4 = \sqrt{\frac{2}{15}} \sum_{n=0}^{\infty} {}_nI_2 \cdot {}_n(\mathcal{E}_4^1)_2 \quad . \tag{III-17}$$

The $\mathcal{E}_i^m$ are defined in Eq. (2.1.22) of Ref. 9 and

$$n^{I}_{\ell} = \sqrt{4\pi} \int_0^1 r^3 [2U(r) + \ell(\ell + 1)\, V(r)]\, \rho_0(r)\, dr \quad . \tag{III-18}$$

Applicability of the normal mode approach depends on the rate of convergence of the infinite sums:

$$\sum_{n=0}^{\infty} {}_n I_{\ell} \cdot {}_n(\mathcal{E}_i^m)_{\ell} \quad . \tag{III-19}$$

Since the strains $\mathcal{E}$ do not increase with n, in general, the convergence depends on the behavior of the integrals $_n I_{\ell}$. Numerical experiment shows that the sums (III-19) converge very rapidly; over 95 percent of the entire contribution comes from only three modes: $_0S_0$, $_0S_2$, and $_1S_2$.

Figure III-4 shows the seven distinct elements of the matrix $\underset{\sim}{D}$ as a function of depth for a realistic earth model PEM[2] and a uniform earth model[20] with $\bar{\rho} = 5.52$ g/cm^3; $\bar{\mu} = 1.463$ Mb and $\bar{\lambda} = 3.514$ Mb. It can be seen that some functions, such as $R_1 - 2S_1$ and $R_2 - 2S_2$, have distinctly different behavior for the two earth models. It follows that application of the uniform earth as an approximation in predicting changes in the moment of inertia may give misleading results; this effect will depend on the actual source mechanism.

In Table III-8 we compare results obtained for several source mechanisms with the values of Dahlen,[21] when applicable. The agreement is excellent; small discrepancies can be explained by difference in the earth models used by us and Dahlen.

Most of the large earthquakes occur at plate boundaries; it has been established before that there is an excellent agreement between the source mechanism inferred from excitation of seismic waves and that predicted by the relative plate motions.

Using the data of Solomon et al.[22] for the positions of the plate boundaries and relative velocities of the plates, as well as the values of the dip of Benioff zones determined from the

TABLE III-8

POLAR SHIFT (S; in units of 0".01) AND ITS DIRECTION (D) FOR SEVERAL SOURCE MECHANISMS AND EARTH MODELS

Earthquake	Dahlen (1973)[21]		PEM-A		PEM-C		Uniform Earth	
	S	D	S	D	S	D	S	D
Chile[17]	1.02	110E	1.39	112E	1.41	112E	0.24	164E
Chile[18]	–	–	1.55	119E	1.56	119E	0.38	178E
Chile[24]	–	–	3.45	119E	3.47	119E	0.84	178E
Alaska[25]	0.48	193E	0.48	194E	0.48	194E	0.21	156E
Alaska[16]	0.73	202E	0.87	204E	0.88	204E	0.38	185E

earthquake distribution, we were able to estimate fault plane parameters for hypothetical earthquakes of three types: dip-slip faulting at mid-oceanic ridges, strike-slip faulting on fracture zones, and thrust faulting associated with the subduction zones. In Fig. III-5 we show the magnitude and the direction of the change in the pole position due to hypothetical earthquakes of a standard moment of 10^{30} dyn-cm. It can be seen that there is a wide range of the potential contribution of different seismic zones to excitation of the Chandler wobble. It may be important that the arrows associated with the earthquakes in some of the most active regions of the circum-Pacific belt have approximately the same direction. Chinnery and Landers[23] present evidence for a simultaneous (on the scale of 1 to 2 months) increase of seismicity in the entire Pacific region. Thus, contributions of earthquakes in different zones could be additive.

A. M. Dziewonski
R. J. O'Connell[†]

REFERENCES

1. Seismic Discrimination SATS, Lincoln Laboratory, M.I.T. (30 June 1975), DDC AD-A014793/4.

2. Ibid. (31 December 1974), DDC AD-A006194/5.

3. T. J. Ulrych and T. N. Bishop, "Maximum Entropy Spectral Analysis and Autoregressive Decomposition," Rev. Geophys. 13, 183-200 (1975).

4. H. Akaike, "A New Look at the Statistical Model Identification," IEEE Trans. Automatic Control AC-19, 716-723 (1974).

5. J. Filson, "Sources of Shallow Asian Earthquakes from Short and Long Period P Waves," Seismological Society of America Annual Meeting, San Francisco, 25-27 March 1975.

6. A. M. Dziewonski, A. L. Hales, and E. R. Lapwood, "Parametrically Simple Earth Models Consistent with Geophysical Data," Phys. Earth Planet. Inter. 10, 12-48 (1975).

7. A. L. Hales, J. R. Cleary, and J. L. Roberts, "Velocity Distribution in the Lower Mantle," Bull. Seismol. Soc. Am. 58, 1975-1989 (1968).

8. A. L. Hales and J. L. Roberts, "The Travel Times of S and SKS," Bull. Seismol. Soc. Am. 60, 461-489 (1970).

9. F. Gilbert and A. M. Dziewonski, "An Application of Normal Mode Theory to the Retrieval of Structural Parameters and Source Mechanisms from Seismic Spectra," Phil. Trans. Roy. Soc. London A278, 187-269 (1975).

10. H. Jeffreys and K. E. Bullen, Seismological Tables (British Association for the Advancement of Science, London, 1967).

11. A. M. Dziewonski and F. Gilbert, "The Effect of Small, Aspherical Perturbation on Travel Times and a Reexamination of the Corrections for Ellipticity," Geophys. J. R. Astron. Soc. 44, 7-17 (1976).

12. F. Gilbert, "Excitation of the Normal Modes of the Earth by Earthquake Sources," Geophys. J. R. Astron. Soc. 22, 223-226 (1971).

† Department of Geological Sciences, Harvard University.

13. L. Knopoff and M. J. Randall, "The Compensated Linear-Vector Dipole: A Possible Mechanism for Deep Earthquakes," J. Geophys. Res. 75, 4957-4963 (1970).

14. A. M. Dziewonski and F. Gilbert, "Temporal Variation of the Seismic Moment and the Evidence of Precursive Compression for Two Deep Earthquakes," Nature 247, 185-188 (1974).

15. R. P. Buland and F. Gilbert, "The Theoretical Basis for the Rapid and Accurate Computation of Normal Mode Eigenfrequencies and Eigen-functions," unpublished note.

16. H. Kanamori, "The Alaska Earthquake of 1964: Radiation of Long Period Surface Waves and Source Mechanism," J. Geophys. Res. 75, 5029-5040 (1970).

17. G. Plafker and J. C. Savage, "Mechanism of the Chilean Earthquakes of May 21 and May 22, 1960," Geol. Soc. Am. Bull. 81, 1001-1030 (1970).

18. H. Kanamori and J. J. Cipar, "Focal Process of the Great Chilean Earthquake May 22, 1960," Phys. Earth Planet. Inter. 9, 128-136 (1974).

19. M. A. Chinnery, "The Static Deformation of an Earth with a Fluid Core: A Physical Approach," Geophys. J. R. Astron. Soc. 42, 461-475 (1975).

20. C. L. Pekeris and H. Jarosch, "The Free Oscillations of the Earth," in Contributions in Geophysics in Honor of Beno Gutenberg (Pergamon Press, New York, 1958), pp. 171-192.

21. F. A. Dahlen, "A Correction to the Excitation of the Chandler Wobble by Earthquakes," Geophys. J. R. Astron. Soc. 32, 203-217 (1973).

22. S. C. Solomon, N. H. Sleep, and R. M. Richardson, "On the Forces Driving Plate Tectonics: Inferences from Absolute Plate Velocities and Intraplate Stress," Geophys. J. R. Astron. Soc. 42, 769-801 (1975).

23. M. A. Chinnery and T. E. Landers, "Evidence for an Earthquake Triggering Stress," Nature 258, 490-493 (1975).

24. H. Kanamori and D. L. Anderson, "Amplitude of the Earth's Free Oscillations and Long Period Characteristics of the Earthquake Source," J. Geophys. Res. 80, 1075-1078 (1975).

25. G. Plafker, "Tectonics of the March 27, 1964 Alaska Earthquake," Geol. Survey Prof. Paper 543-I (1969) — 74 pages.

Fig. III-1. Error curve (solid curve) and Akaike's FPE (short dashed curve) and AIC (long dashed curve) order criterion curves for imaginary part of log spectrum indicating that data have an order of 23.
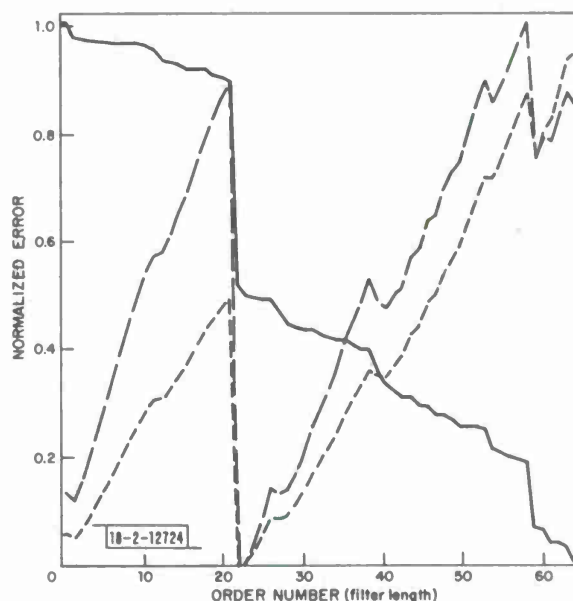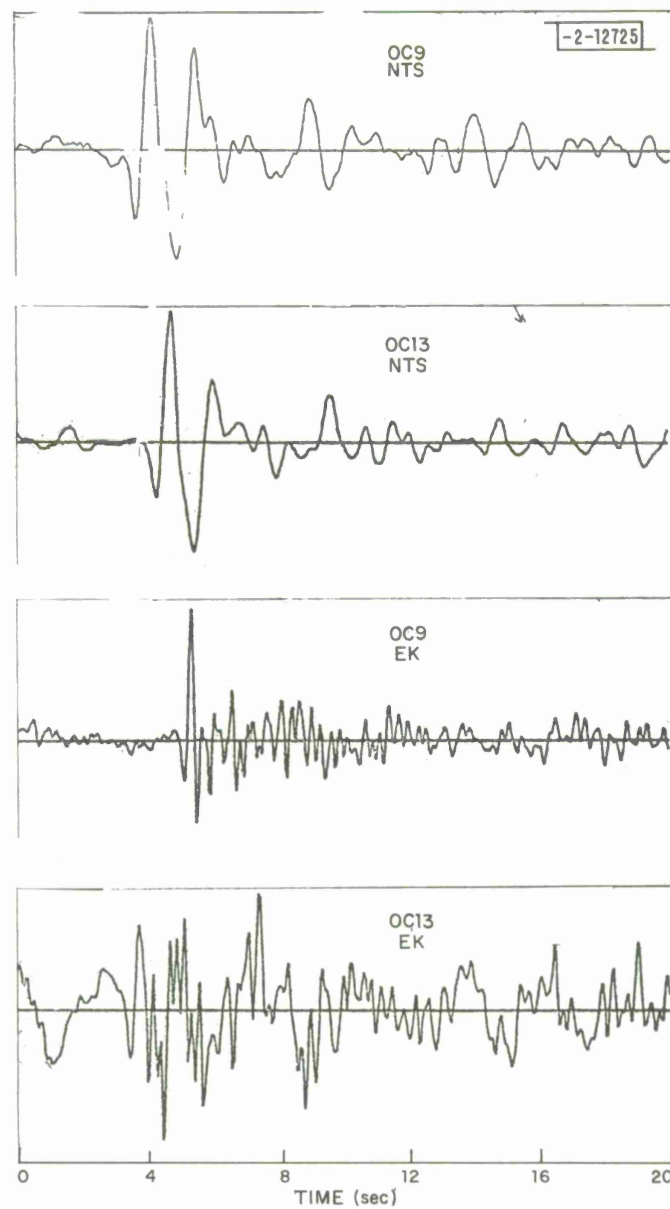
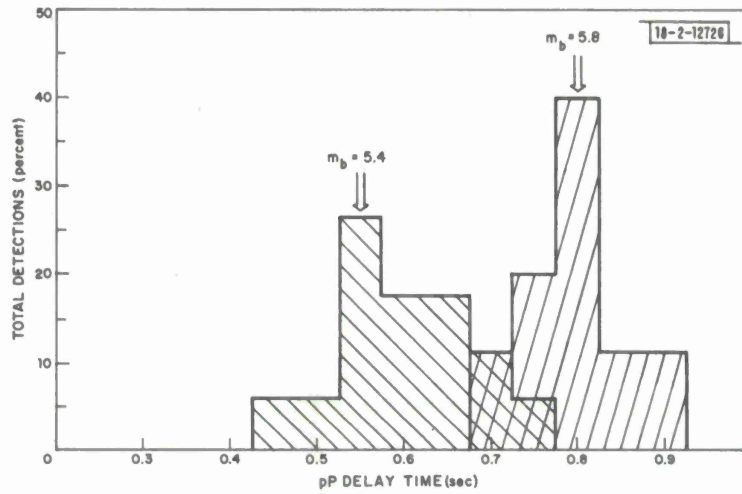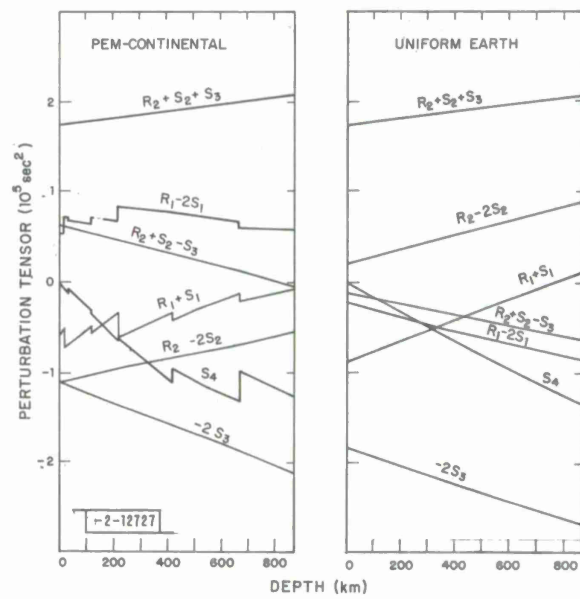Fig. III-2.   Raw signals at subarray centers OC9 and OC13 for events NTS and EK.

Fig. III-3.   Histograms of pP detections for events NTS and EK.

Fig. III-4.   Distinct elements of matrix $\mathcal{D}$ [Eqs. (III-15) and (III-16)] as a function of depth for two earth models.
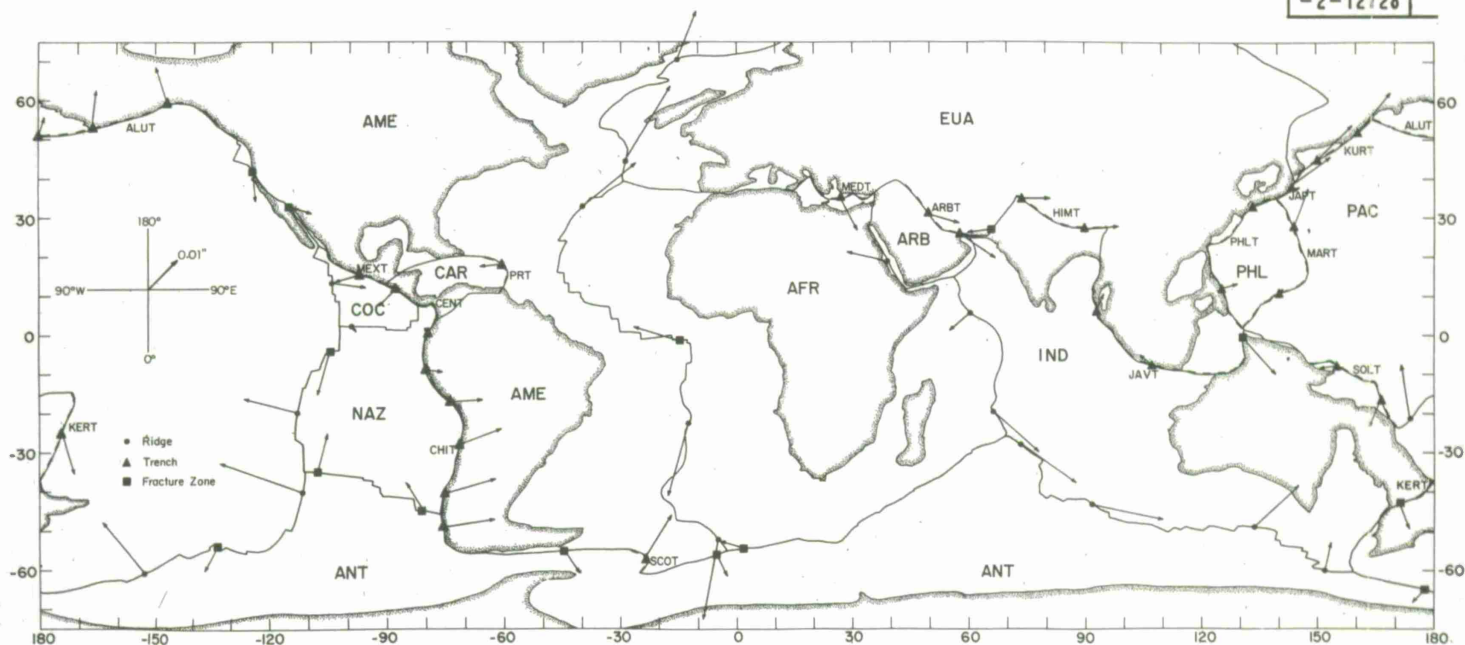

67

Fig. III-5. Magnitude (arrow's length) and direction (see inset for definition) of polar shifts in response to three types of hypothetical earthquakes with standard moment of 10^{30} dyn-cm.

IV. COMPUTER SYSTEMS AND SOFTWARE

A. SRO DATA TAPE PROCESSING FACILITY

PDP-7 Console expansion and other software required to effectively handle SRO data tapes were discussed in the last SATS.[†] Several of the design and implementation tasks mentioned have now been completed.

The major software items which have been implemented since the previous report are:

(1) Console users can now time-shift and modify the gain of an individual seismic trace on the display without changing any of the other traces.

(2) A PDP-11 program (SROSP) which strips short-period data from an SRO 9-track tape and creates a Data Unit[†] on a 7-track tape is operational. Another very similar program to do the same for the long-period SRO data is not yet implemented, but will be once >DUI and >TAB discussed below have been completed.

(3) A PDP-7 program (DUM) to merge Data Unit tapes generated by SROSP (and the not yet implemented long-period equivalent) into composite Data Unit tapes containing data from several stations is now available.

(4) A new Console program (>SAV) to save data from a Console session in the same Data Unit format as that generated by SROSP and DUM has been designed and completed. It will append data to an existing Data Unit as well as create a new one.

(5) As part of the above software implementation, several general Fortran subroutines were created for our PDP-7 computers. A set of these allow character string manipulations. Others create, check, and extract information from the Type, Description, and Title sections of a Data Unit. Still others support reading and writing of the actual data in the body of the Data Unit.

(6) Also in support of this software effort, the PDP-7 Fortran system was modified to allow multiple formatted reads of the same physical record.

Other software components have been designed and are now being coded, the major one of which is >DUI which will provide convenient and efficient initialization of the Console from Data Unit tapes. This program will be driven by a condition table set up by another program, >TAB. The first version of >TAB is also specified. It will set up the condition table to find all SRO P- or Rayleigh-wave data for an event, given only the event location and origin time.

It will be inconvenient for researchers to handle multistation SRO data in the Console environment until >DUI and >TAB are completed. However, a simple test program is now available which does allow us to enter Data Units into the Console. For example, Fig. IV-1 shows twenty SRO short-period waveforms which were entered into the Console and then plotted with existing programs. Table IV-1 lists events reported by USGS which correspond to some of the signals in Fig. IV-1.

[†] Seismic Discrimination SATS, Lincoln Laboratory, M.I.T. (30 June 1975), DDC AD-A014793/4.

TABLE IV-1

ASSOCIATION OF SRO DATA TRACES OF FIGURE IV-1 WITH EVENTS REPORTED BY USGS

Trace Number	Event Parameters					
	Date (1974)	Origin Time	Latitude (°S)	Longitude (°W)	Magnitude	Distance (deg)
1	22 December	02:18:36.9	26.9	176.2	5.1	90.1
8 (1)	22 December	16:44:15.5	19.0	69.8	5.2	64.0
8 (2)	22 December	16:44:05.3	17.6	179.0	5.1	86.3
10	22 December	18:06:36.2	27.0	176.3	5.2	90.3
15	23 December	01:04:02.7	14.6	175.7	5.4	82.0
17	23 December	08:13:58.8	3.0	75.4	4.6	47.7
18	23 December	11:16:48.2	16.2	176.7	4.6	83.8
19	23 December	11:31:00.0	26.3	177.5	4.2	90.7

(1),(2) Arrivals from two events are on the same trace. First arrivals for each are indicated by (1) and (2) on trace 8 of Fig. IV-1.

Each SRO contains a short-period event detector which triggers the saving of the data. The twenty waveforms shown in Fig. IV-1 correspond to the first twenty detections by the ALQ site starting on 22 December 1974. All gains are the same except traces 15 and 20 which are attenuated by 1/4 and 1/8, respectively. Those signals which correspond to events on the USGS Preliminary Determination of Epicenters List are identified in Table IV-1. In one case (trace 8) two events occur, with the second one arriving about 65 sec after the first. Traces 5, 9, and 16 show no clear arrivals but may contain coda or secondary arrivals from the events with the first arrivals on traces 4, 8, and 15, respectively. There were four PDE events in the same time period with distances <90° from ALQ which did not trigger the ALQ SRO event detector. The PDE magnitudes and distances for these events are:

m_b	Distance (deg)
5.0	70
4.6	53
3.5	69
—	39

Several of the traces not associated with the PDE list show very clear arrivals and, as mentioned above, some do not strongly indicate distinct arrivals. Trace 3, however, shows a

relatively clear but small arrival. Figure IV-2 shows trace 3 and a filtered version which clearly shows the arrival. The filtered version was obtained simply by the application of the Console filter program.

The SRO at ALQ was just starting operation in December 1974. It is not our purpose here to evaluate the site or the performance of the event detector at that time. However, some observations can be made about our small data set. The data quality is excellent. The event detector was set in such a way that it generated very few false alarms. It might be that if more false alarms had been allowed, one or two of the missed PDE events would have triggered the detector. Certainly, in a network environment many more false alarms can be and should be tolerated than occur in our small sample of data.

<div style="text-align: right">R.T. Lacoss
M.F. O'Brien
L.J. Turek</div>

B.   USE OF ARPANET FOR INTERACTIVE DISPLAY AND ANALYSIS OF SEISMIC NETWORK DATA

A study of earthquake source mechanisms using P-waves from shallow Asian earthquakes was reported in the last SATS (30 June 1975, DDC AD-A014793/4). That study involved the use of seismograms from a network of stations and of theoretical seismograms for the same stations. Displays showing theoretical and observed seismograms and how the station was located with respect to the hypocenter and fault plane orientations were found to be quite helpful in that study. However, the construction of the displays was a slow manual process which detracted from the study and use of the data. Motivated by this, an interactive seismic display and analysis package has been written to generate displays and perform the kind of analysis required for those source-mechanism studies. The package is a fairly general interactive display system which has been implemented to demonstrate how remote computation and data storage can be combined with a graphics terminal as a tool for seismic research involving a number of seismic stations. The source-mechanism problem is just one possible application.

The display and analysis package runs under the time-sharing system on the Lincoln Laboratory IBM-370/168. The user terminal is a Tektronics terminal with a storage cathode-ray-tube display. The terminal is attached to the 370 through the ARPANET. Two such terminals are available and are used for a variety of interactive and graphics-based activities.

Figure IV-3 is an example of the kind of display generated by the system. It can display up to twenty waveforms for an event, the orientation of the stations with respect to the event location, and the orientation with respect to the fault plane and slip vector if these are known. In the figure shown, the central circle is the lower half focal sphere for the event. A symbol is shown in that circle for each station of interest. The symbol is at the azimuth of the station from the event, and the distance from the origin represents the takeoff angle for P-waves. The fault plane is also shown in the usual way on such a display. The symbol used for each station indicates if the first motion is up, down, or has not been entered into the data. More stations can be displayed than seismograms and, in fact, the display can be used for fault-plane studies without displaying any seismograms at all. In the display shown, there are two seismograms shown for each station. One of these is the actual seismogram of the long-period P-wave, and the other is a theoretical one generated by the model built into the system. In each case, the actual seismogram is identified by the station three-letter code and the theoretical one has a T appended. The * indicates that time scaling has been adjusted and the user should refer to the display system output file, which is discussed below, for details.

The display and analysis package makes use of four distance files of data — three are input and one is output. Two of the input files constitute a waveform library which can be created and modified independent of the display system. These files can contain any number of seismograms. They can be both long and short period, actual, or theoretical. Each is identified by station, date, time, time interval, sampling rate, gain, instrument type, a comment if desired, and a unique seismogram identification number. These two files are the universe of possible signals which can be displayed by the display system. If the display system calls a subsystem to generate theoretical waveforms, the theoretical ones are added to this universe and treated exactly like actual signals for display purposes. The third input file is specific to the display package. It contains the hypocenter and origin time of events of interest and, if desired, specifications of the stations and waveforms of interest. If such specifications are not given, the program will immediately enter the interactive mode and display a menu of options to the user. The output file just contains tables which completely specify the actual display. In fact, the display is generated by internal subroutines which are driven by this so-called output file and which get waveform data from the so-called input files.

The display shown in Fig. IV-3 was, in fact, generated using the interactive capability of the system. The original display generated for the same event is shown in Fig. IV-4. During the interactive session, the user has generated theoretical seismograms and added them to the display, changed various scaling parameters, added the fault plane, and changed the size of the central circle to clean up the general appearance of the plot.

Table IV-2 shows the menu available to the user. At essentially any point in a terminal session, he can request to exercise any or all of the options. He simply enters the list of

TABLE IV-2	
MENU OF OPTIONS FOR THE INTERACTIVE DISPLAY SYSTEM	
Argument	Definition
WAVFM	Display waveform file before making a change
ISEIS	Add, replace, or delete waveforms to display
SCLRAD	Scale the radius of the net projection to another
MAXPTS	Change maximum number of waveform points to display
FAULT	Display the fault plane and theoretical waveforms
CNET	Change the stereographic projection to azimuth-delta type
CTOA	Change the delta limits for the station projections
CONLIN	Do not connect plot projection and waveform with a line
NOAZI	Do not order waveforms azimuthally for plot
CTIM	Scale the time axis for the waveform(s)
CAMP	Scale the amplitude display for the waveform(s)
CSTA	Change the station code(s) to waveform serial number(s)
TMSTRT	Change the start time of the displayed waveform(s)

arguments corresponding to the changes he wishes to make, and the system then requests all further information it requires. The normal use of the system is to set an initial display, make a hard copy using a device attached to the terminal, request the menu and make changes, generate a new display, etc.

L. C. Lande
R. T. Lacoss

C. PROGRESS REPORT ON NLS (ON-LINE SYSTEM) AND THE SEISMIC DATA MANAGEMENT SYSTEM

Most of the major files that will make up the NLS directory for the Seismic Data Management System have been updated and structured within the NLS system. Some of these files contain the site descriptions of the High Gain Long Period sites (HGLP) and of the Seismic Research Observatories (SROs). They reflect the current state of development in those areas where development is still in progress, the Seismic Research Observatories for example, as well as containing complete descriptions of both the hardware aspect of the SROs and the software necessary to run the sites.

The main effort that is now under way is basically divided into two parts. The first part is the continuing acquisition of additional information and documentation that will be placed in the directory ⟨IWWSS⟩. Information related to the Network Event Processor (NEP), Seismic Information Processor (SIP), Control and Communication Processor (CCP), as well as the actual structure of the seismic files that will be stored on the mass store device, would fall into the category of information that should be contained in the NLS directory. Also connected with this aspect of the effort is the continued acquisition of updated information describing the installation of the SRO sites, and the additional information about the SRO installations as they become operational and begin to produce actual data.

The second main area of effort concerns procedures by which researchers and other users of the seismic information directory will access this information. All the information that is contained and collected in the seismic directory ⟨IWWSS⟩ will be made available in hard-copy form, and therefore not require that the user have any prior knowledge of the ARPANET or NLS. This is the simplest method of getting the information to interested users. However, this is a slow, cumbersome, and inappropriate means of information transfer. The other means available are to provide access to the directory ⟨IWWSS⟩ and allow the user to obtain those files that pertain to the topics of interest. The files maintained in this directory will be in both text form and in NLS form. The advantage to the user is that he should be able to copy these files on his terminal as a sequential text file, or he can enter the NLS world and freely browse through these NLS files addressing any topics of interest.

There are two approaches to providing on-line ARPANET access to the data files. The simplest and most convenient approach would be to make these files available in a semipublic, protected directory with read-only privilege similar to the NIC directory at OFFICE-1. This is the approach that is now being taken. The directory ⟨IWWSS⟩ will have the proper protection and restrictions to allow the user access to only this directory and not the rest of the OFFICE-1 (or ISIC) system. The data information files would be maintained both as NLS files and as text files, thus allowing the user the choice of methods of data retrieval. The text versions could be listed at the terminal of the user or at some other line printer, while the NLS versions would be available to experienced NLS users.

The developers of NLS, the Stanford Research Institute, have now begun to train and distribute information which will allow users to write and set up complete user subsystems within the NLS environment. This will provide a very useful and powerful means for setting up a complete seismic user subsystem (SUS) within NLS. The complete design of SUS is not yet complete; however, the goal of this subsystem will be to interact with the user and try to provide him with description and information that is desired without making a novice user stumble through the data files.

R. M. Sheppard

D.   THE APPLIED SEISMOLOGY GROUP (ASG) ARPANET CONNECTION

The ASG uses the ARPANET to provide time-sharing terminal access to several large computer sites, as described in the previous SATS (30 June 1975, DDC AD-A014793/4). An ELF operating system, running on a PDP-11/40 computer, connects seven terminals and a lineprinter to the ARPANET.

We are continuing to improve the software and the hardware supporting the network connection. Recent improvements include:

|	
Improved reliability	The ELF system crashes two times per week, on the average. This represents an order-of-magnitude improvement in reliability from that previously reported.
Availability of 11/50 system for development	The ELF system was transferred to the PDP-11/40, releasing the 11/50 (which has many peripheral devices) for software and hardware development.
Interprocessor device	We have designed and tested a simple but robust high-speed interprocessor device for PDP-11 computers. Three pairs of these will be built, enabling us to communicate efficiently among our three PDP-11's (an 11/50, an 11/40 and a GT-40 graphics terminal).
Lineprinter facility	Software provided on the Lincoln 370 computer by Group 28 to allow sending files over the ARPANET can now be used to send files to our ELF system for lineprinter listing. Previously, we had been able to get listings only from TENEX sites.

P. A. Neilson
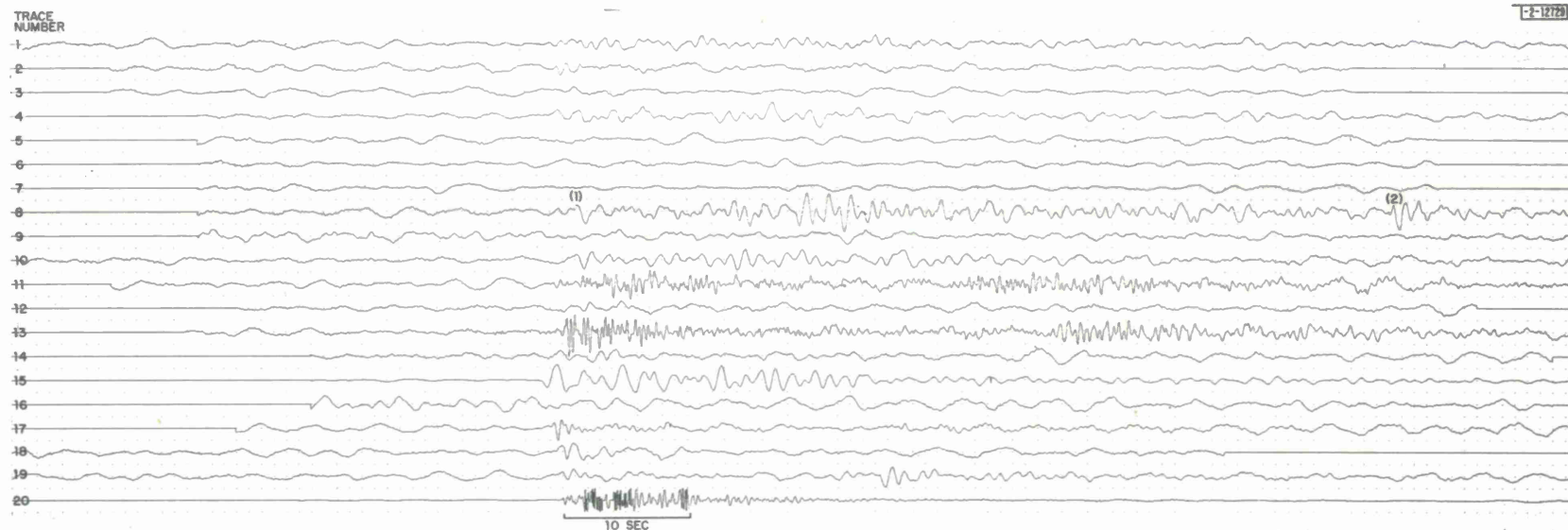
Fig. IV-1. Display of short-period vertical waveforms corresponding to a sequence of twenty detections by ALQ SRO site.
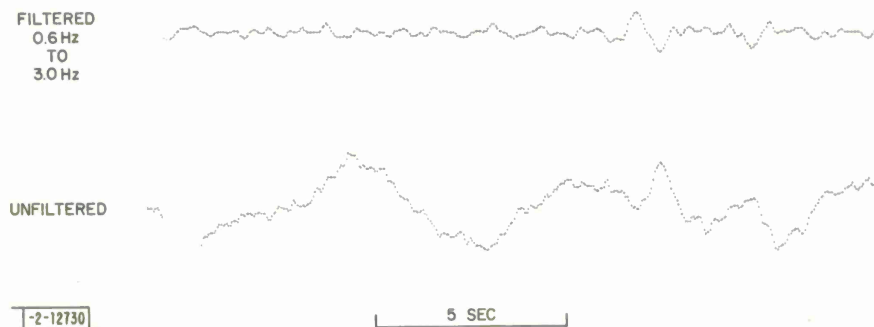
Fig. IV-2. Unfiltered short-period vertical SRO waveform, and same trace bandpass-filtered to pass 0.6 to 3.0 Hz.
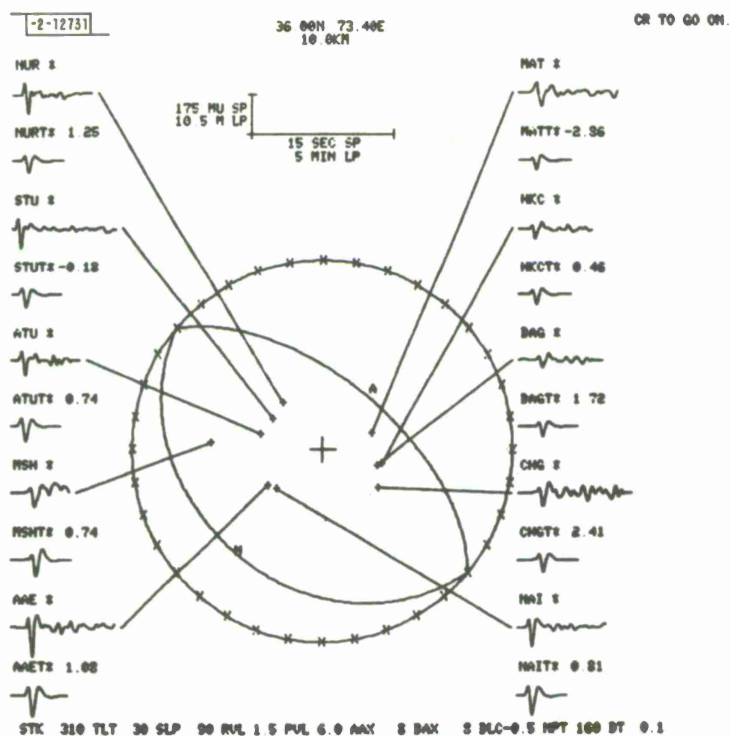

Fig. IV-3. Actual and theoretical seismograms displayed by interactive display system.
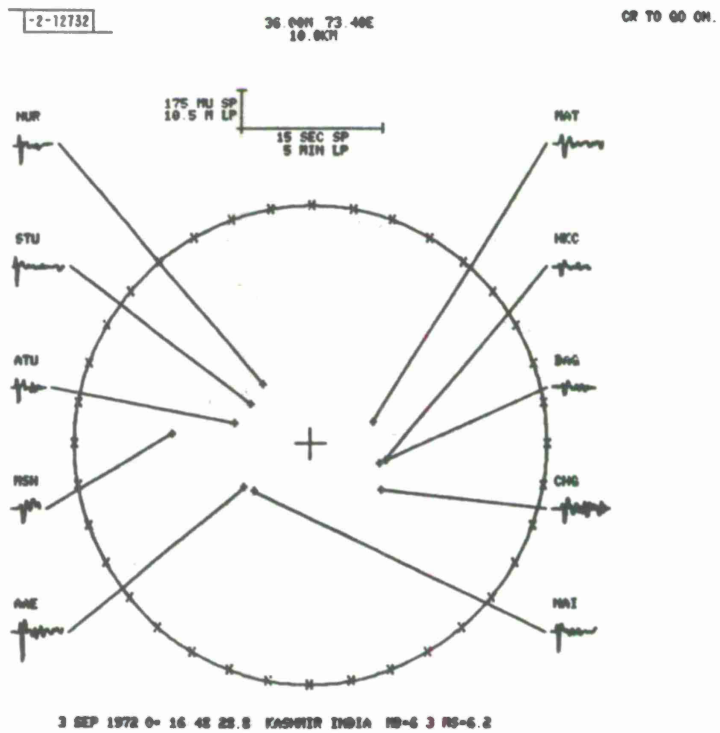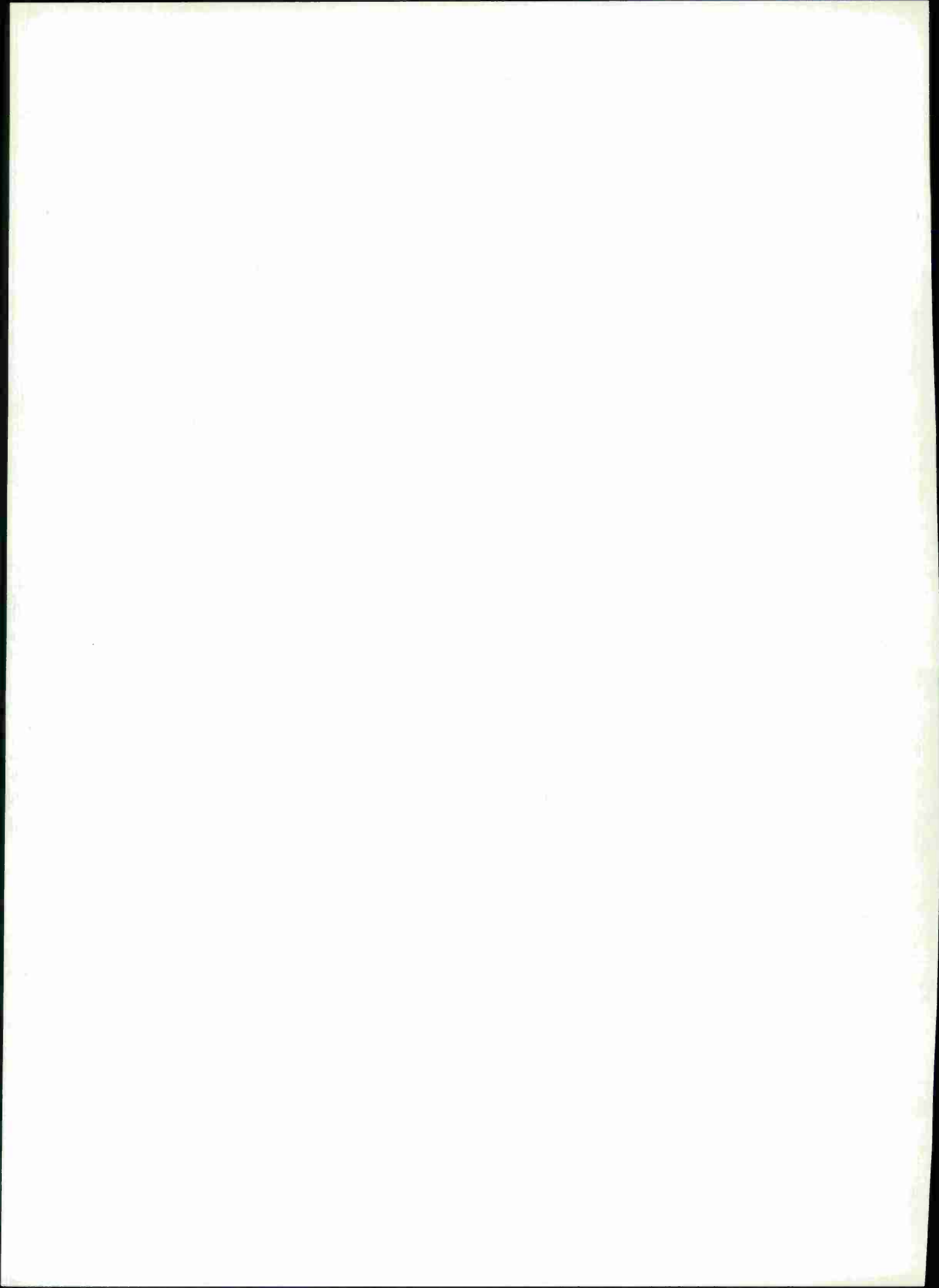
Fig. IV-4.   Initial seismogram display from interactive display system.

V. PUBLICATIONS LIST

The following list contains an update to the Seismic Discrimination publications list printed in the 30 June 1974 SATS (DDC AD-785377/3).

Requests for these reports or reprints should be addressed to:

> The secretary
> Lincoln Laboratory Group 22
> 42 Carleton Street
> Cambridge, MA 02142

132. J. Capon, "Signal Processing and Frequency-Wavenumber Spectrum Analysis for a Large Aperture Seismic Array," in Methods in Computational Physics, Vol. 13, B. A. Bolt, Ed. (Academic Press, New York, 1973), pp. 1-59.

133. D. W. McCowan and E. A. Flinn, "Curvature Spectra: Applications to Signal Detection and Estimation of the Resolving Power of Arrays," Geophys. J. R. Astr. Soc. 37, 179-190 (1974).

134. D. B. Jovanovich, M. I. Husseini, and M. A. Chinnery, "Elastic Dislocations in a Layered Half-space I. Basic Theory and Numerical Methods," Geophys. J. R. Astr. Soc. 39, 205-218 (1974).

135. D. B. Jovanovich, M. I. Husseini, and M. A. Chinnery, "Elastic Dislocations in a Layered Half-space II. The Point Source," Geophys. J. R. Astr. Soc. 39, 219-240 (1974).

136. C. W. Frasier and D. K. Chowdhury, "Effect of Scattering on PcP/P Amplitude Ratios at Lasa from 40° to 84° Distance," J. Geophys. Res. 79, 5469-5477 (1974), DDC AD-A006707/4.

137. E. S. Husebye, A. Christoffersson, and C. W. Frasier, "Orthogonal Representation of Array-Recorded Short Period P-waves," NATO Advanced Study Institute, Proceedings (1974).

138. S. C. Solomon and B. R. Julian, "Seismic Constraints on Ocean-Ridge Mantle Structure: Anomalous Fault-Plane Solutions from First Motions," Geophys. J. R. Astr. Soc. 38, 265-285 (1974).

139. R. G. North, "Seismic Slip Rates in the Mediterranean and Middle East," Nature 252, 560-563 (1974).

140. Seismic Discrimination Semiannual Technical Summary, Lincoln Laboratory, M.I.T. (31 December 1974), DDC AD-A006194/5.

141. R. T. Lacoss, "Review of Some Techniques for Array Processing," in Exploitation of Seismograph Networks, K. G. Beauchamp, Ed. (Noordhoff, Leiden, 1975), pp. 11-24.

142. R. T. Lacoss, "Interactive Computational Tools for Research," in Exploitation of Seismograph Networks, K. G. Beauchamp, Ed. (Noordhoff, Leiden, 1975), pp. 313-322.

143. J. Filson and T. Simkin, "An Application of a Stochastic Model to a Volcanic Earthquake Swarm," Bull. Seismol. Soc. Am. 65, 351-358 (1975).

144. J. Filson, "Array Seismology," Annu. Rev. Earth Planet. Sci. 3, 157-181 (1975).

145. M. A. Chinnery, "The Static Deformation of an Earth with a Fluid Core: A Physical Approach," Geophys. J. R. Astr. Soc. 42, 461-475 (1975).

146. Seismic Discrimination Semiannual Technical Summary, Lincoln Laboratory, M.I.T. (30 June 1975), DDC AD-A014793/4.

147. R. E. Needham, "Worldwide Detection Capability of a Prototype Network of Seismograph Stations," Technical Note 1975-42, Lincoln Laboratory, M.I.T. (19 August 1975), DDC AD-A016058.

148. M. A. Chinnery and T. E. Landers, "Evidence for Earthquake Triggering Stress," Nature $\underline{258}$, 490-493 (1975).

149. M. A. Chinnery and R. G. North, "The Frequency of Very Large Earthquakes," Science $\underline{190}$, 1197 (1975).

150. S. Das and J. Filson, "On the Tectonics of Asia," Earth Planet. Sci. Lett. $\underline{28}$, 241-253 (1975).
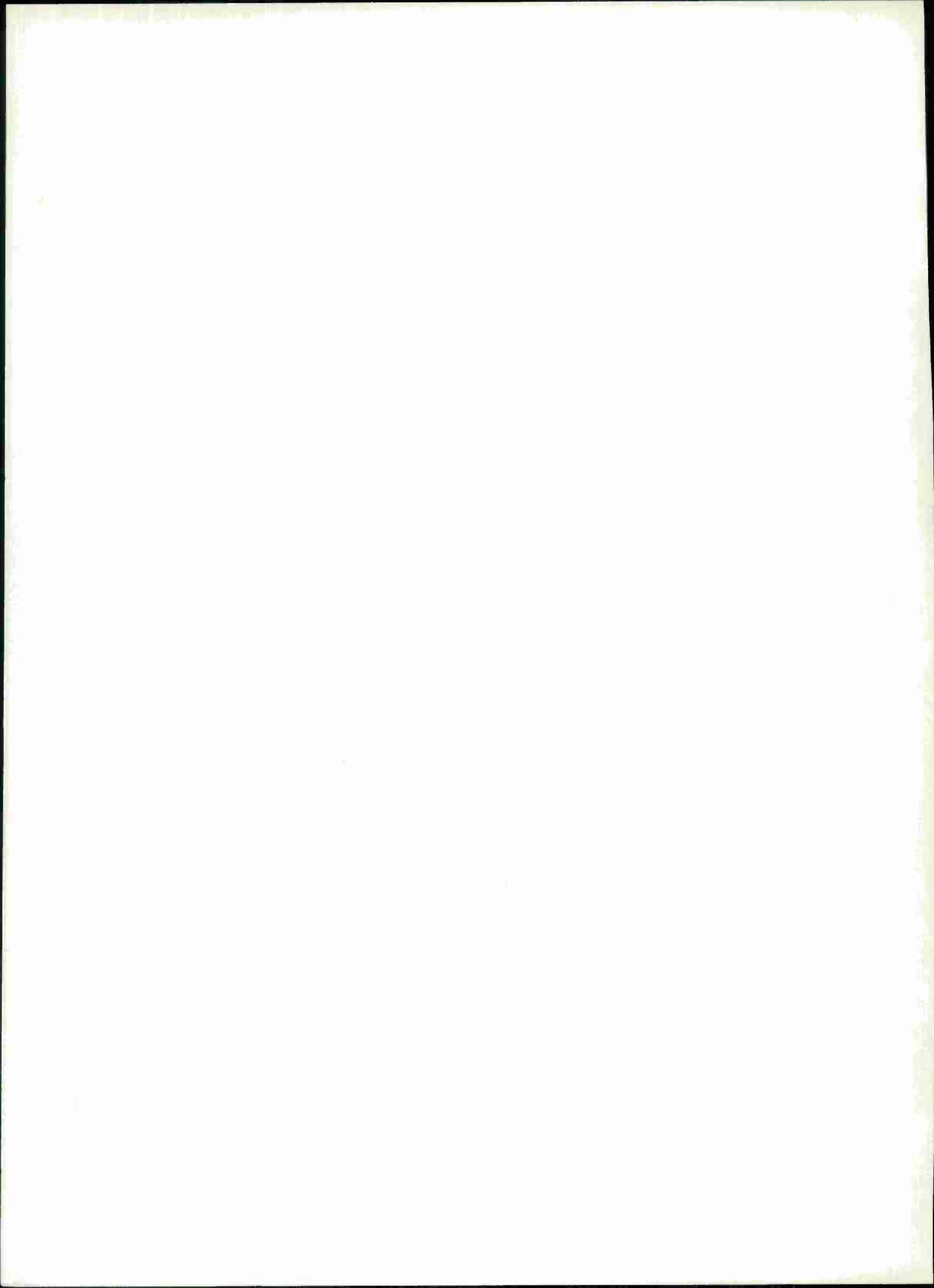
REPORT DOCUMENTATION PAGE		READ INSTRUCTIONS BEFORE COMPLETING FORM
1. REPORT NUMBER ESD-TR-75-335	2. GOVT ACCESSION NO.	3. RECIPIENT'S CATALOG NUMBER
4. TITLE *(and Subtitle)* Seismic Discrimination		5. TYPE OF REPORT & PERIOD COVERED Semiannual Technical Summary 1 July – 31 December 1975
		6. PERFORMING ORG. REPORT NUMBER
7. AUTHOR*(s)* Michael A. Chinnery		8. CONTRACT OR GRANT NUMBER*(s)* F19628-76-C-0002
9. PERFORMING ORGANIZATION NAME AND ADDRESS Lincoln Laboratory, M.I.T. P. O. Box 73 Lexington, MA 02173		10. PROGRAM ELEMENT, PROJECT, TASK AREA & WORK UNIT NUMBERS ARPA Order 512 Program Element No. 62701E Project No. 6F10
11. CONTROLLING OFFICE NAME AND ADDRESS Defense Advanced Research Projects Agency 1400 Wilson Boulevard Arlington, VA 22209		12. REPORT DATE 31 December 1975
		13. NUMBER OF PAGES 92
14. MONITORING AGENCY NAME & ADDRESS *(if different from Controlling Office)* Electronic Systems Division Hanscom AFB Bedford, MA 01731		15. SECURITY CLASS. *(of this report)* Unclassified
		15a. DECLASSIFICATION DOWNGRADING SCHEDULE

16. DISTRIBUTION STATEMENT *(of this Report)*

Approved for public release; distribution unlimited.

17. DISTRIBUTION STATEMENT *(of the abstract entered in Block 20, if different from Report)*

18. SUPPLEMENTARY NOTES

None

19. KEY WORDS *(Continue on reverse side if necessary and identify by block number)*

seismic discrimination	surface waves	NORSAR
seismic array	body waves	ARPANET
seismology	LASA	

20. ABSTRACT *(Continue on reverse side if necessary and identify by block number)*

This report describes 23 investigations in the field of seismic discrimination. These are grouped as follows: estimation of magnitude by networks and single stations (6 contributions); studies relating to earth structure and scattering processes (7 contributions); studies in focal depth determination, source mechanism discrimination, and general seismology (6 contributions); and recent developments in computer systems and software for seismic data processing (4 contributions).